# Deciphering the force-dependent lifetime dynamics of tip-links in inner-ear

**Nisha Arora**

*A thesis submitted for the partial fulfillment of*
*the degree of Doctor of Philosophy*


Department of Chemical Sciences
Indian Institute of Science Education and Research Mohali
Knowledge city, Sector 81, SAS Nagar, Manauli PO, Mohali 140306, Punjab, India.

December, 2022

# Declaration

The work presented in this thesis has been carried out by me under the guidance of Dr. Sabyasachi Rakshit at the Indian Institute of Science Education and Research Mohali. This work has not been submitted in part or in full for a degree, a diploma, or a fellowship to any other university or institute. Whenever contributions of others are involved, every effort is made to indicate this clearly, with due acknowledgment of collaborative research and discussions. This thesis is a bonafide record of original work done by me and all sources listed within have been detailed in the bibliography.

Nisha Arora

In my capacity as the supervisor of the candidate's thesis work, I certify that the above statements by the candidate are true to the best of my knowledge.

Dr. Sabyasachi Rakshit

# Acknowledgments

During the PhD tenure, I came across many good people who have influenced me and have provided immense support from time to time. I take this opportunity to express my sincere gratitude and thanks to everyone who has been a part of this journey.

Firstly, I am extremely thankful and grateful to my PhD supervisor, Dr. Sabyasachi Rakshit for his immense support, suggestions, and guidance. I am thankful to him for his genuine interest in my project and for taking part in the experiments and analysis whenever required. He has exceptional skill of deep and logical thinking toward a scientific problem. I appreciate his true and unbiased judgement in every aspect. His insightful suggestions were the source of motivation that allowed me to extend my boundaries and perform beyond my comfort zone.

I am thankful to my thesis committee members Dr. Purnananda Guptasarma and Dr. Arijit Kumar De for the timely evaluation and valuable insights regarding the work.

I sincerely thank Dr. Ashish (IMTECH, Mohali) for timely evaluation of the work as my external committee member and for providing help in modeling the protein structures.

I extend my thanks to Dr. Amin Sagar for all the simulation studies that helped us to delineate the catch-bond mechanism. I am also thankful to Dr. Abhishek Chaudhuri and his student, Sandip Roy for the Langevin simulations. Their interest in this work helped it to acquire its present shape.

I am thankful to Dr. Raj Ladher (NCBS, Banglore) for providing us the constructs of Cadherin-23 and Protocadherin-15.

I sincerely thank Dr. Sarika Gupta (NII, Delhi), Dr. Shivprasad Patil (IISER Pune), Dr. Deepak Sharma (IMTECH, Mohali), and their lab members for allowing us to use their AFM instrument when ours was down.

I am thankful to Dr. Sharmistha Sinha for her kindness and support during these years.

I am really thankful and grateful to my seniors who were the foremost Ph.D. students in the lab, Dr. Gayathri and Dr. Jagadish. They introduced me and taught me about designing and performing experiments. I am thankful to Gayathri for her constant support and being a good friend, and for addressing all my concerns patiently. I am thankful to Jagadish for his support, all the work that we did together, and all the scientific discussions we had.

I am thankful to all past postdoctoral members of the lab, Dr. Jesse, Dr. Deb, Dr. Malay, and Dr. Amin for sharing their knowledge and experience.

Many thanks to all the lab members, Surbhi, Sai, Tanuja, Veerpal, Gaurav Bhati, Pritam, Devansh, Vishawdeep, Dr. Varinder, Nilesh, Rohini, Keshav, Satavisa, Sayan, Deepali, Dr. Sonu for always maintaining a friendly and vibrant atmosphere in the lab. I thank Surbhi and Sai for being good friends, as joined in the same batch we have seen all the phases of this journey together.

I thank all the Sinha lab members for their support.

I am grateful to IISER Mohali for providing the infrastructure and CSIR for the fellowships during my tenure.

I would like to express my thanks and gratitude to all my friends Parul, Rekha, Deeksha, Shaina, Radha, Surbhi, and Simer for their help and genuine support over these years. I extend my thanks to hostel friends, Arpita Sharma, Pratima, Bindia, Shivali, Neeladrita, and Arpita Mrigwani for their friendly behavior throughout.

My sincere thanks to Dr. Gyanendra Kumar Bisaria (Sant ji) for inspiring me to pursue Ph.D.

I am extremely grateful to my family. My parents, for believing in me and supporting me throughout the endeavor. My elder brother Rajan, who always motivated me to achieve higher and showered on me his love, support and care. My sister, Dimple for her affection and support. I extend my thanks to uncle, aunt, Richa, and Tilak for their love, care, and support.

## *ABBREVIATIONS*

| | |
|---|---|
| *AFM* | *Atomic Force Microscopy* |
| *DNA* | *Deoxyribose Nucleic acid* |
| *EC* | *Extracellular domains* |
| *EGTA* | *Ethylene glycol-bis (β-aminoethyl ether)- N, N,N',N'-tetra acetic acid* |
| *HEPES* | *4-(2-hydroxyethyl)-1-piperazineethanesulfonic acid* |
| *mg* | *milligram* |
| *mL* | *millilitre* |
| *MD* | *Molecular Dynamics* |
| *nm* | *nanometre* |
| *NTA* | *Nitrilo Tri-Acetic acid* |
| *PCR* | *Polymerase Chain Reaction* |
| *RPM* | *Rotations per minute* |
| *RT* | *Room Temperature* |
| *SDS-PAGE* | *Sodium Dodecyl Sulphate poly- Acrylamide Gel Electrophoresis* |
| *SEC* | *Size Exclusion Chromatography* |
| *SMFS* | *Single-Molecule Force Spectroscopy* |
| *µg* | *microgram* |
| *µL* | *microliter* |

# PREFACE

## Chapter 1

## Introduction

Hearing is one of the five phenomenal senses for seeing the world. Hearing sensation and balance in vertebrates involve the transformation of sound as a mechanical stimulus into electrical signals. This transformation is known as mechanotransduction. Hair cells, highly sensitive mechanoreceptors present in the inner ear, mediate this mechanotransduction process. The apical end of each hair cell features bundles of hair-like projections known as stereocilia that are arranged in order of increasing heights. The mechanical force from the sound stimuli causes the deflection of the hair bundle towards the tallest stereocilia. These deflections create tension in a long protein filament, the tip-links which connect the tip of the shorter stereocilium to the side of the taller neighboring stereocilium. The tension in the tip-links guide the opening of the mechanically gated ion channels residing at the lower end of each tip-links and allows the influx of $K^+$ and $Ca^{2+}$ ions through it that subsequently depolarizes the associated hair cell. This change in cell polarity signals the brain through the afferent auditory nerve and is decoded as speech, noise, or music.

Tip-link is a 150-180 nm long protein couple formed by two calcium-dependent non-classical cadherin proteins, Cadherin-23 (Cdh23) and Protocadherin-15 (Pcdh15). Both proteins comprised of one cytoplasmic domain, a single-pass transmembrane domain, and exceptionally long extracellular cadherin (EC) domains, with 27 and 11 EC domains in Cdh23 and Pcdh15, respectively. Interestingly, despite being long proteins, only two outermost N-terminal domains of Cdh23 and Pcdh15 interact in a handshake-like trans mode to form an antiparallel heterodimer. Electron microscopy images illustrated that tip-links exist as heterotetramer formed by the parallel cis-homodimers of Cdh23 and Pcdh15. *Homo sapiens* perceive sound in the frequency range of 20 Hz-20 kHz and the amplitude range of 5-120 dB. Tip-links are always in continuous exposure to mechanical forces from sound stimuli. The varying intensity of sound exposes the tip-links to the force of 10 pN to

100 pN in the perceived frequency range. Intriguingly, it is important to study the mechanical strength of the tip-links complex in this wide range of input forces. Single-molecule studies estimated the lifetime of the tip-links as ~8 s at the resting tension of 10 pN and less than 1 s at 50-60 pN. This indicates that the tip-links won't even survive at higher forces from the loud sound of up to 100 pN.

The first objective of this thesis is to decipher how the tip-links maintain their complex integrity at high forces.

Furthermore, studies showed that the force required to open the gated ion channels is ~ 4-8 pN, suggesting that tip-links dissipate the extra input force that is not utilized for the opening of the ion channel. How the tip-links dissipate the extra force while simultaneously conveying the required force to open the ion channel is still elusive. The second objective of this thesis is to delineate the mechanism of tip-links as gating springs that simultaneously serve as force conveyor and force dissipator.

**Chapter 2**

**Tip-links follow slip-catch-slip by transitioning into a stronger binding conformation**

Tip-links sense the force from sound stimuli and transmit it to the transduction channels at its lower end. Different intensity of sound exerts a force of up to 100 pN on the tip-links. How tip-links withstand and maintain their complex integrity in such a varying range of forces from sound stimuli is not yet clear. In this chapter, we aim to decipher the mechanical response of the tip-links with varying mechanical perturbations.

In tip-links, Cdh23 and Pcdh15 interact via their N-termini through the outermost two domains EC1-2, therefore, we first intended to examine the force-dependent bond lifetime dynamics of the interacting domains to exclusively measure the response of the binding interface. We performed the single-molecule force clamp spectroscopy employing Atomic Force Microscopy (AFM) to achieve high loading rates corresponding to high-frequency sound. We observed that the tip-links follow an atypical triphasic slip-catch-slip transition with force. To understand the molecular details, we performed steered molecular dynamic simulation using infinite switch simulated tempering in force (FISST). *In-silico* studies highlight the mechanism for the slip-to-catch transition in the tip-link complex as an

enhancement in the buried surface area which is corresponding to a more stable conformation. The transition from a low-affinity state to a high-affinity state is driven by a robust salt bridge between Cdh23(E78) and Pcdh15(R113) which acts as a molecular pivot. We further explored its pivotal role by measuring the pairwise inter-residue forces which showed that this interaction remains in a pre-tensed state and the tension remains constant at all the forces due to a load balancing activity which drives the force away from this critical interaction. An inherited deafness mutation R113G disrupts the pivot and turns a slip-only dissociation of the complex. Finally, we fit the experimental data with a mathematical model to extract the kinetic parameters.

**Chapter 3**

**Non-interacting domains of Cdh23 modulate the elasticity of tip-links and aid in the force-dissemination**

Cdh23 and Pcdh15 are very long proteins with 27 and 11 EC domains, respectively; however, only two N-terminal domains interact to mediate the heterophilic interaction. The rest of the non-interacting domains may interact laterally to facilitate the formation of cis-homodimer. In addition, the presence of these spare domains also modulates the elasticity of the tip-links. As proposed earlier, tip-links to function as a gating spring should have an elastic nature. However, the effect of protein elasticity on tip-links dynamics has not yet been studied in detail. In this chapter, we aimed to understand how the slip-catch-slip bond nature of the tip-links varies when we introduce the non-interacting domains which will manifest the overall elasticity of the tip-links. To achieve this objective, we designed and expressed different fragments of Cdh23 with varying numbers of EC domains to systematically incorporate the elasticity factor into the tip-links complex. We expressed Cdh23 EC1-5, Cdh23 EC1-10, Cdh23 EC1-21, and full-length Cdh23 EC1-27, and subsequently performed force-clamp measurements for all these tip-links variants with Pcdh15 EC1-2 to mediate the interaction. Interestingly, force-lifetime data for all these tip-links complexes of different lengths showed a similar slip-catch-slip feature. However, the overall lifetime increases systematically with the increasing length of the tip-links. We also noticed unfolding-associated unbinding in the force-clamp spectra for all complex variants.

Further, we observed a hike in the unfolding percentage with the increase in EC domain number which is contributing to prolong the lifetime of the tip-link. We further incorporated the force-induced unfolding dynamics into the kinetic model to fit the experimental slip-catch-slip data for all variants of the tip-links complex and estimated the kinetic parameters.

**Chapter 4**

**Heterotetramer tip-links feature a slip-ideal-slip bond under force**

Tip-links exist as a heterotetramer where the cis-homodimer of Pcdh15 participates in trans-binding with the cis-dimer of two opposing Cdh23 proteins. Recent studies confirmed the formation of the cis-homodimer of Pcdh15 in the tip-links. Crystal structure and negative staining transmission electron microscopy of Pcdh15 showed two points of dimerization; one is the EC2-3 domain and the other is a membrane adjacent domain (MAD or Pcdh15 interacting channel associated (PICA) domain) after EC11. However, no similar experimental and structural studies have been reported so far for the specific cis-dimerization sites of Cdh23. Further, a recent study has shown the effect of rebinding in the heterotetramer tip-links which is facilitated by the cis-dimerization and results in a substantial increase in the bond lifetime. In this chapter, we too set out to study the force-lifetime behavior for the heterotetramer of tip-links and the effect of rebinding. We performed similar force-clamp measurements among dimers. We found that the lifetime for the heterotetrameric tip-links follow a slip-ideal-slip with force. Rebinding feature was reflected as the bi-exponential fitting of the survival probability plots, especially at higher forces where lower-lifetime component didn't undergo rebinding. We propose that the slip-ideal-slip bond nature of the heterotetrameric tip-links reflects their gating spring function by acting as a low-force pass-filter. At lower force-range, it allows the force to convey to the ion-channel while at higher force-range, it dissipates the extra force and makes the complex ideal. We verify the ideal bond nature of the heterotetrameric tip-links using Langevin dynamics on polymer chains. Finally, we propose a gating spring model of tip-links in terms of springs and dashpots.

# CONTENTS

# Chapter 1

## Introduction

## 1.1 Mechanosensing and Mechanotransduction

*"Everything in biology is mechanical".* - Julio Fernandez

Nature is governed by the four fundamental forces, gravity, strong nuclear forces, weak nuclear forces, and electromagnetism(1). All the events and phenomena are controlled by these forces. Although, 'force' as such is perceived as a physics terminology but in the last five decades, the origin and flourishing of mechanobiology have been observed in various biological processes(2). Everything in biology is mechanical from embryo to adult(3).

Biological systems generate, sense, and respond to the mechanical force(4). The sensation of the mechanical force is known as mechanosensing and transducing the mechanical signal into a biological response is called mechanotransduction. Mechanotransduction involves the conversion of a mechanical signal into an electrical signal for a range of sensory phenomena like touch, hearing, and balance(5, 6). The electrical signal is the language of the nervous system that can be read out by the brain. Nobel Prize 2021 in physiology and medicine is awarded to David Julius and Ardem Patapoutian for their discovery of receptors responsible for the sensation of heat & cold (temperature) and touch (mechanical stimuli). Their discoveries helped in understanding the mechanism of how the nervous system senses heat, cold, and mechanical stimuli and interprets our environment.

Mechanosensing and mechanotransduction are ubiquitous and vital for the cells and tissues to function in the body. Biological processes such as replication, transcription, translation, protein translocation across the membranes and cell locomotion generate the mechanical force(4, 7, 8). Further, the stiffness of the extracellular matrix (ECM) determines the normal cell functions(9) and a change in the ECM mechanical stiffness is reported to cause the progression of cancer and other diseases(10). The importance of mechanical tension is also demonstrated in regulation of the tissue morphogenesis in developing embryos(11, 12).

Cells in our body receive the mechanical tension from blood flow, breathing, muscle contraction, heart-pumping, etc. and use this mechanical information to make decisions

about various processes like growth, motility, differentiation, cell division, and cell death(13). Moreover, our brain and its constituent cells experience physical forces during development, maturation, and ageing. Neurons and glial cells convert these physical forces into signals(14, 15).

A large number of mechanosensors and transducers have been identified so far. For example, mechanosensitive ion-channels(16–18), vinculin(19, 20), talin(21), integrin(22), paxillin(23), actin cytoskeleton(24, 25) etc. The molecular basis of mechanotransduction is described as the force-induced conformational change in the associated proteins that play an essential role in force-sensing and transducing(26). In the last two decades, mechanical properties of proteins under force have been studied extensively using in-vitro single-molecule techniques to understand their role in regulating the in-vivo cellular functions(27).

This thesis focuses on the mechanotransduction in hearing where inner ear hair cells act as the force-sensors. During hearing, force is received from the incoming sound stimuli and converted into electrical signals through mechanosensitive ion-channels of the hair cells.

## 1.2 Mechanotransduction in hearing

Hearing is a highly coordinated mechanotransduction process where specialized cells of our ear serve as mechanosensors. During the process of hearing, sound waves enter through the outer ear, and after a chain of structured processes in the middle and inner ear, it is interpreted by the brain(28, 29). Mechanotransduction for hearing and balance happens in the inner ear(30). The inner ear is mostly a fluidic chamber. Vibrations from the sound waves create oscillations in the inner ear fluid(31, 32). The inner ear has a spiral-shaped cochlea bathing in the fluid which further has organ of Corti(33). The organ of Corti resides on the basilar membrane in the inner ear which vibrates in response to fluid oscillations from the sound(34). The organ of Corti differentiates the different frequencies of sound along the length of the basilar membrane; the high-frequency sound is processed at the proximal end while the low-frequency sound is at the distal end of the organ(35). Basilar membrane harbors hair cells at their apical end. Hair cells are the sensory organ of the inner

ear cochlea(36) and are classified into two types, outer hair cells (OHCs) and inner hair cells (IHCs). OHCs amplify the input sound signal while IHCs play a key role in mechanotransduction(37, 38). On the apical surface of hair cells, an array of 50-100 hair-like projections of increasing heights protruded as an organized bundle, called hair bundle **(Figure 1)**. Hair bundle functions as a mechanical antenna of the hair cell. Individual projections in the bundle are called stereocilium(39–42). The tip of each shorter stereocilium is linked to the side of an adjacent taller stereocilium with a fine filamentous element called tip-links(43–45). Incoming sound stimuli induce the deflection of stereocilia towards the tallest stereocilium and consequently, tip-links get stretched.

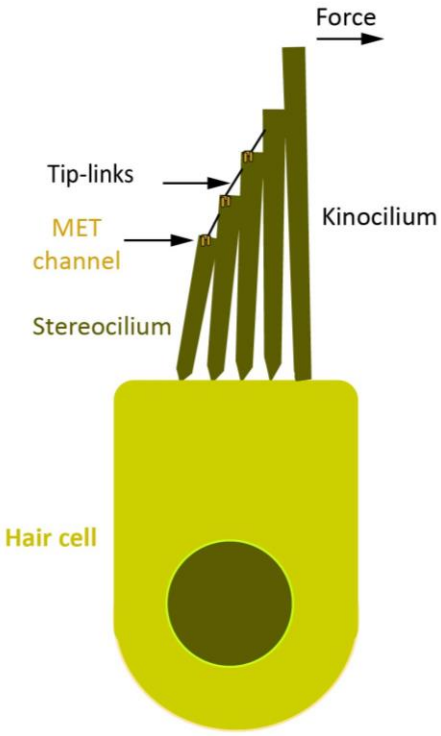


**Figure 1: Schematic of hair cell with hair bundle at the apical end.** Each stereocilium in the hair bundle is connected to the next taller stereocilium through a filamentous element at the tips, known as tip-links. Mechanotransduction channels reside at the bottom of each tip-link.

Tip-links are thought to work as mechanotransducer that transduces the received tension to mechanosensitive ion-channels or mechanoelectrical transduction (MET) channels that

are localized near the tip of shorter stereocilia(46, 47). The tension in the tip-links results in the opening of an ion-channel, specifically a non-selective cation channel that allows the passage of $K^+$ and $Ca^{2+}$ ions through it and leads to the depolarization of the associated hair cell(30, 48, 49). This signal of change in cell polarity conveys auditory information to the brain which the brain interprets. Although mechanotransduction in hearing has been studied in detail, the search for the associated molecular components is still ongoing. Two sets of molecular components are identified that are directly involved in the mechanotransduction, one is the MET channel and the other is the tip-link that together constitutes the MET machinery.

## 1.3 Proteins associated with the MET machinery

### 1.3.1 Components of mechanosensitive ion-channels

Over the years, many molecular components have been proposed as plausible MET-channel candidates such as transmembrane channel-like proteins 1 and 2 (TMC 1 and 2)(50–52), tetraspan membrane protein in hair cell stereocilia (TMHS; also known as Lipoma HMGIC Fusion Partner-Like 5; LHFPL5)(53, 54) and transmembrane inner ear expressed gene (TMIE)(55). All these proteins are identified based on their characterization as deafness-associated genes and possession of multiple transmembrane domains to form the ion-channel. However, there was still uncertainty about the molecule that forms the channel(56). A Series of studies in the past years suggested that TMC1 and 2 are the strong candidates to form the channel. For instance, a mutation in the TMC1 gene causes hearing loss in humans and mice. Moreover, both TMCs are absent in the tallest stereocilia where the MET channel is not present. In 2020, it was shown that these TMC proteins directly respond to the mechanical force, and their mutation results in the abolition of the transduction current, thus directly implicating the pore-forming subunits of the ion-channels(57). In Another study, it was demonstrated that TMIE is also a subunit of the MET channel and directly interacts with the TMC1 and 2. Mutation in the TMIE that disrupts their interaction, abolished the transduction current(58). Thus, all four proteins i.e.

TMC1, TMC2, TMIE, and LHFPL5 are closely linked to the transduction channel, however, TMC1/2 along with TMIE are the plausible component to form the channel.

### 1.3.2 Components of tip-links

In 2000, the first high-resolution electron microscopy image of tip-links from guinea pig cochlea describes the tip-links as a 150-200 nm long helical structure of two strands(59). In the last two decades, several experiments have been performed to identify the molecular components of the tip-links. Earlier studies showed that tip-links are sensitive to calcium and dissociate after treatment with the calcium chelator BAPTA (1,2-bis(o-aminophenoxy)ethane-N,N,N′,N′-tetraacetic acid), this inferred that tip-links have similar properties to cadherins(60, 61). On similar lines, Cadherin-23 (Cdh23), a giant non-classical cadherin protein, was hypothesized to be a part of the tip-links based on its characterization as one of the deafness mutant genes(62). Mutation in Cdh23 was identified to cause non-syndromic hearing loss DFNB12 (Autosomal Recessive Deafness) and usher syndrome USH1D (63, 64). USH1D is associated with blindness in humans. Later, it was found that Protocadherin-15 (Pcdh15) is also associated with deafness/blindness-related usher syndrome USH1F and non-syndromic hearing loss DFNB23(65). Finally, in 2004, Siemens et.al showed the antibody labeling of tip-links against Cdh23(66) that experimentally demonstrated the presence of Cdh23 in the tip-links and justifies its role in mechanotransduction. Based on the existing evidence, in 2007, Kazmierczak et. al., specifically generated the antibodies against the extracellular (EC) domains of Cdh23 and Pcdh15 and successfully showed that both Cdh23 and Pcdh15 localized at the tip-links and interact via their N-terminus(67). Further, disruption of the tip-links with BAPTA treatment disclosed the localization of Cdh23 to constitute the upper part of the tip-links and Pcdh15 to form the lower part **(Figure 2a)**. Subsequently, TEM images demonstrated the individual tip-links proteins as cis-dimers. Overall, it is now believed that the tip-links is a heterotetrameric complex comprising parallel homodimers of Cdh23 and Pcdh15.

Pcdh15 at the lower end interacts with the MET channel **(Figure 2a)** while Cdh23 at the upper end interacts with harmonin and myosins.

### 1.4 Structure of tip-links

After the molecular identity of the tip-links proteins was revealed, efforts were made to understand the structural details of both the constituent proteins mediating the interaction. Both Cdh23 and Pcdh15 are non-classical cadherin family proteins with a cytoplasmic domain, single-pass transmembrane domain, and very long extracellular (EC) domains. Cdh23 and Pcdh15 possess 27 and 11 EC domains, respectively.

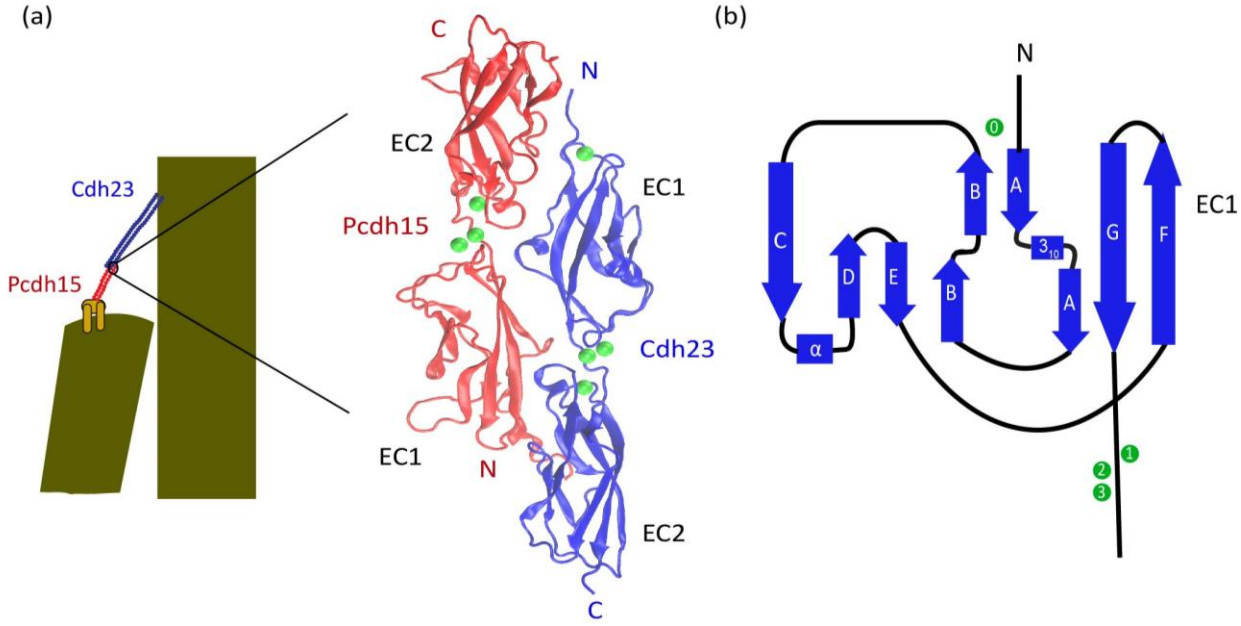


**Figure 2: Tip-link is constituted by the heterophilic interaction between the outermost two domains (EC1-2) of Cdh23 and Pcdh15.** (a) Tip-link is a heterotetramer made up of dimer of Cdh23 (blue) from the top interacting with dimer of Pcdh15 (red) from the bottom. Zoomed view showing the crystal structure (PDB: 4AQ8) for interaction between two N-terminal domains (EC1-2) of Cdh23 (blue) and Pcdh15 (red) in handshake-like trans-conformation. Two consecutive domains generally bind to 3 $Ca^{2+}$ ions (green) at the linker region. (b) Topology diagram of the EC1 domain of Cdh23 depicting seven β-strands inter-connected with loops.

In 2012, Sotomayor et al. employed the X-ray crystallography to elucidate the structure of tip-links and the nature of the heterophilic interaction. They found that the two distal N-

terminal domains of both the constituent proteins, interact in trans-fashion like an overlapped extended-handshake to form the tip-links(68) **(Figure 2a)**. Each EC domain has a Greek key motif fold with seven β-strands interconnected with loops similar to classical cadherins(68, 69) **(Figure 2b)**. Two EC domains are connected by an inter-domain linker that binds to three calcium ions in a canonical arrangement. Calcium-binding to the linkers provides rigidity and mechanical stability to the individual protein and the tip-link complex as shown by the subsequent simulation studies on the solved crystal structure(68, 69).

Furthermore, to reveal the complete structural details of Cdh23 and Pcdh15, Sotomayor and coworkers have expressed various truncated fragments (with 2 or 3 domains) of both the proteins and subsequently crystallized them for refined structures(70–72). To date, the entire Pcdh15 structure has been solved, however, in fragments(73). Linkers between domains EC2-3, EC3-4, EC5-6, and EC9-10 are identified as non-canonical linkers that bind to 2, 2, 1, and 0 calcium ions, respectively and are likely to impart flexibility to the protein(70, 71). EC9-10 with no calcium at the linker results in an L-shaped bent conformation leaving EC9 and EC10 domains perpendicular to each other. Model of Pcdh15 with the entire 11 EC domain is assembled (using PyMOL)(74) here, and shown in **Figure 3a**.

For Cdh23, the structure of 18 EC domains, EC1-3, EC6-8, EC12-14, EC17-18, EC19-21, EC22-24, and EC24-25 has been solved so far. Based on the solved domains, nine consecutive EC domain structure from EC17 to EC25 (EC7-25) was modeled and proposed to have inherent helicity that could contribute to the elasticity of the tip-links (72). In Cdh23, inter-domain linkers between EC2-3, EC12-13, EC20-21, EC21-22, and EC24-25 have been identified as non-canonical linkers, having calcium-binding residues different than the canonical ones. These linkers are expected to possess decreased affinities for calcium ions. The solved crystal structure of EC24-25 also showed that only two $Ca^{2+}$ ions bind to this linker(72). Interestingly, all the crystal structures have been solved at a high

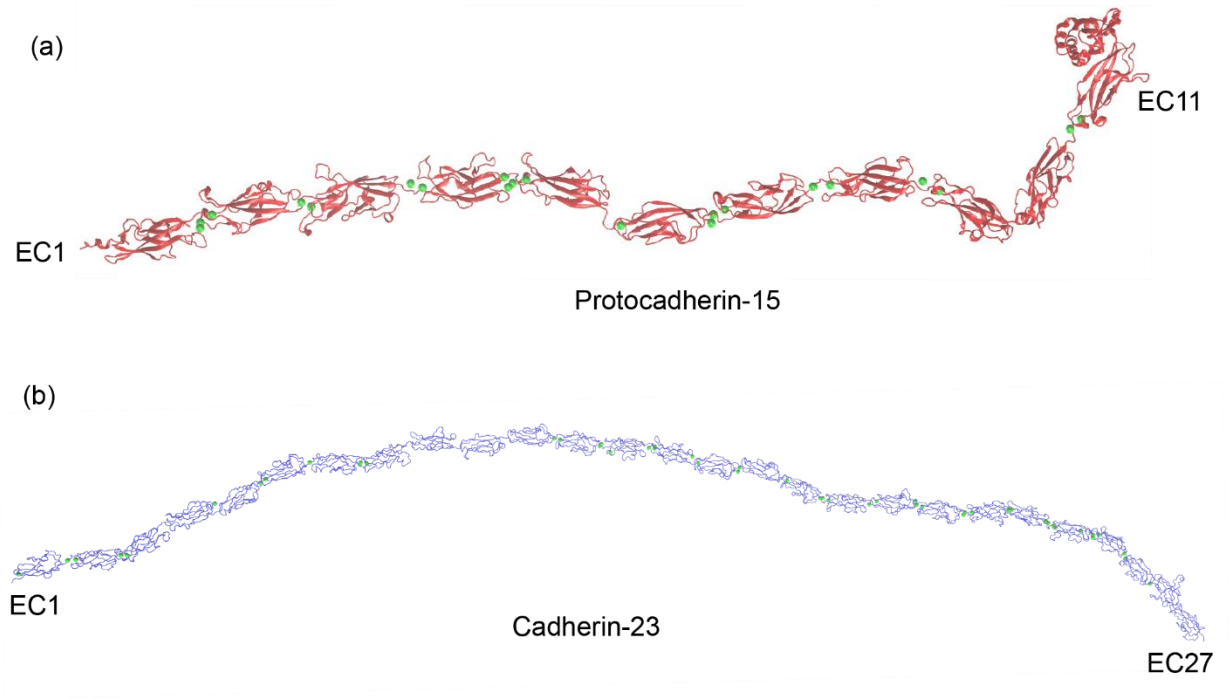


**Figure 3: Modeled structures of Pcdh15 EC1-11 and Cdh23 EC1-27 proteins.** (a) Pcdh15 EC1-11 PICA structure assembled using solved crystal structures of smaller fragments. (b) Cdh23 EC1-27 structure was constructed by including solved crystal structures of 18 EC domains and the remaining 9 EC domains were modeled by template-based modeling using the SWISS model(75). Green spheres represent the calcium ions that bind to inter-domain linkers.

calcium concentration but the endolymph fluid has 20-50 µM of $Ca^{2+}$ in which the tip-links are bathed(76, 77). So, depending on the calcium ion dissociation constant of each site, the effective $Ca^{2+}$ binding extent of all the linkers would be lower. This decrease in the binding affinity implies that less than three calcium ions would bind to the linker at physiological calcium concentration. Moreover, missense mutations at the calcium-binding sites also alter the binding affinity and are shown to cause hearing loss(64).

Besides 27 and 11 EC domains, Cdh23 and Pcdh15 also have one membrane adjacent domain (MAD) with a different structural architecture, which is designated as $28^{th}$ and $12^{th}$ domains, respectively. For Pcdh15, this MAD domain (also called Pcdh15 Interacting-Channel Associated (PICA) domain) has been identified to mediate the cis-dimerization

along with the EC3 domain as shown by using Small Angle X-ray Scattering (SAXS), X-ray crystallography and Cryo-EM studies(78, 79). This domain has a ferredoxin-like fold with 130 conserved amino acids. However, no experimental evidence and structural studies have been reported so far for the specific cis-dimerization sites of Cdh23.

### 1.5 Function of tip-links as gating springs

The conversion of hair bundle deflection into the electrical signal happens within the time limit of 10-500 μs, where larger displacements lead to a faster response(80, 81). Such a fast response is required to process the high-frequency sound and thus, exclude the involvement of any second messengers during the transduction process(80). Therefore, it was postulated that mechanical force is transduced to the transduction channel through an elastic element called 'gating spring' present in series with the channel. This gating spring is stretched as a result of hair-bundle deflection towards the taller edge and conveys the force to the ion-channel.

Tip-links, that connect the two neighboring stereocilia are proposed to serve as a potential gating spring that gates the hair-cell transduction channels and opens them up(43). In past experiments, the tip of a flexible glass fiber was used to apply force on the hair bundle and subsequent displacement of the hair bundle was measured. From this, the stiffness of the gating spring was estimated to be 1 pN/nm(82, 83), referring to a soft spring. However, electron microscopy studies showed that tip-links exists as a helical braid in dimeric form and is predicted to be relatively stiffer with a rigid conformation(59). The molecular dynamics simulations by Sotomayor et. al. using the outermost two cadherin domains measured a very high stiffness of 710 pN/nm per domain at the slowest simulation speed of 0.1 nm/ns(69). They further extrapolated the calculation and estimated the total stiffness of the tip-links as 40-60 pN/nm (38 repeats in the parallel dimer). This imposed the question of how the tip-links alone with such a high stiffness can serve as a gating spring? The next obvious proposal was therefore to connect a relatively elastic component in series with tip-links to achieve stiffness of the gating spring. Overall, the concept of a tip-links complex

was proposed which comprised of tip-links proteins, ankyrin, and other associated components(84).

Hearing is periodic i.e., the sensory organ receives a signal at a period of ~10 µs interval or even less for a high-frequency sound(81). Moreover, adaptability or fast recovery from the last signal is another important parameter in this sensory transduction(85). Thus, the involvement of too many components as gating spring in the tip-links complex was not a very convincing model and not well accepted, rather simple gating spring model was preferred. Henceforth, the search for the gating spring components within tip-links proteins was still ongoing. In 2016, Hudspeths' group proposed tip-links alone can acts as gating spring. They applied mechanical force on the tip-links of the bullfrog's sacculus using a DNA tethered superparamagnetic bead. As a result, the transduction current was measured which was independent of the hair bundle deflection(86).

In mammals, tip-links experience a force of 10-100 pN from a varying range of sound intensity (5 dB-120 dB) and frequency (20 Hz-20 kHz)(87, 88). Tip-links as proposed gating spring, thus, survive and convey forces for ion-channel opening. For the different magnitudes of forces, it is important for the tip-links to convey threshold force and dissipate the rest. How tip-links manage such filtering and withstand these varying forces is not yet known. In the last decade, the mechanical response of tip-links has been investigated by employing *in silico* molecular dynamic simulations and single-molecule techniques. Structural studies revealed the elastic properties within the protein due to the presence of non-canonical linkers(70, 71). Further, the single-molecule pulling experiments on the Pcdh15 EC1-11 monomer reported various length gains and estimated the enthalpic stiffness of Pcdh15 EC1-11 as ~10 pN/nm(89). For the parallel dimer of Pcdh15, stiffness would be 20 pN/nm. Similarly, keeping in mind the length of Cdh23 and its 2/3 contribution in constituting the tip-links, tip-links' overall stiffness was estimated as 6 pN/nm, which quite falls in the range to work as a gating spring(89). Similar to Pcdh15, Cdh23 is also shown to undergo different extensions in response to force, hence depicting the elastic nature(90).

Single-molecule experiments identified monomeric Pcdh15 as an elastic component in the tip-links. Subsequently, structural investigations identified the molecular cues that can provide the elasticity to the tip-links from both the monomer and cis-dimer of Pcdh15. Simulations were performed on the entire modeled structure of Pcdh15, (EC1-11 with the MAD domain) in complexation with two outermost domains of Cdh23 to mediate the interaction(73). During Steered molecular dynamics (SMD) when force was applied, it was found that first the bending between EC9-10 gets straightened followed by stretching of non-canonical linker regions, and with the increase in force, the MAD/PICA domain started unrolling and then unfolding. Overall, this results in a total extension of ~19 nm. Furthermore, a hetero-tetrameric tip-links structure was constructed comprising a parallel cis-dimer of Pcdh15 EC1-MAD interacting in trans with a parallel dimer of Cdh23 EC1-2/1-3 and subsequently, simulation was performed. Extensions of Pcdh15 were observed in the same order as previously for the monomeric tip-links, however, the total extension was reduced to ~11 nm for this hetero-tetrameric complex. This indicates that the tetramer of the tip-links is relatively stiffer(73). These simulation studies identified the cues within the individual protein that imparts elasticity to the tip-links even in the dimeric form. Subsequently, the next approach was to see the force response of the tip-links complex. In 2012, Steered molecular dynamics (SMD) simulation on tip-links with two interacting domains of both the proteins showed the unbinding of the complex at forces >400 pN and revealed the important stabilizing salt-bridges and hydrogen-bond interactions that are crucial to mediate the tip-links complex(68). In 2018, an AFM-based single-molecule experiment on tip-links with two interacting domains also measured the high binding strength of the complex. In the same study, *in silico* results showed that the force-propagation pathway from one protomer to the other is orthogonal to the direction of the pulling force(91). This orthogonal component reduces the effective force sensed by the complex and makes the complex more resilient to force.

In 2021, single-molecule force spectroscopy was performed using optical tweezers to study the dynamics of tip-links bond in monomeric and dimeric forms(92). In this experiment,

loading rates varied between 22.5 pN/s to 271.5 pN/s that applied the maximum force of up to 60 pN on the bond. It estimated the intrinsic lifetime of ~2s for monomeric tip-links and lifetime drops with the increase in force depicting a slip-bond feature. Furthermore, a dimer of the tip-links showed an intrinsic bond lifetime of 22-63 s. This substantial hike in the lifetime was attributed to the load-sharing and rebinding of the complex after the single-bond dissociation. Rebinding was shown to be more prominent at forces less than 20 pN. Rebinding is facilitated by the cis-dimerization of both the proteins, which would keep the interacting domains closer to bind again. From these single-molecule studies, the lifetime of the dimer of tip-links was estimated to be ~8 s at a resting force of 10 pN and less than a second at higher forces of 50-60 pN. From these measurements, the question arises does the tip-links break at higher forces of up to 100-150 pN that originate from very loud sound in a nightclub or a jet engine? Or the tip-links can survive these forces by naturally existing but unexplored mechanism.

Based on the above literature speculations, we asked the two questions.

(a) Why does tip-links exist as a complex and does the complex have any role in force-dissipation by the gating spring?

(b) If tip-links serve as a gating spring what would be the gating spring model of tip-links, comprising of force-conveying and dissipating elements.

### 1.6 (a) Evolutionary thirst of tip-links as a protein-complex

Initially, when only Cdh23 was known to be a part of the gating spring or tip-links, it was proposed that Cdh23, as being a long protein, might be forming the entire tip-links. Later on, Pcdh15 was identified as the second component of the tip-links. We asked the question of why tip-links evolutionary exists as a complex of Cdh23 and Pcdh15 and why not only a single protein extends from one stereocilium to the other and conveys the sensed force to the ion-channel. Towards this, we aimed to understand the mechanoresponsive properties of the tip-links, a handshake complex of Cdh23 and Pcdh15 using Atomic Force Microscopy (AFM) based single-molecule force spectroscopy (SMFS). For comparison, we also studied the force-responsive behavior of individual Cdh23 protein without its

partner protein, Pcdh15. This work has already been included in one of my colleagues' thesis and appended here in the appendix section. I was involved in this project and will briefly discuss the overall results.

To understand the evolutionary drive of the tip-links as a complex, an AFM-based force-ramp experiment was performed in two protein configurations. One where we pulled biotinylated Cdh23 EC1-27 with a cantilever using biotin-streptavidin interaction. We named this geometry handle-assisted pulling (HAP). Similarly, for the second configuration, we pulled the Cdh23 EC1-27 with Pcdh15 EC1-2 using tip-links complexation. We named this mode of pulling as partner-assisted pulling (PAP). From the AFM experiment using both these geometries, we observed multiple unfolding peaks for Cdh23 EC1-27, and then corresponding unfolding forces were estimated. We observed that unfolding forces for Cdh23 in the PAP configuration are higher than in the HAP one. This indicates that protein in the complex form is more resilient to force compared to when pulled directly using a handle. From these observations, we conclude that tip-links in handshake-like geometry is mechanically more stable than in the individual protein geometry to serve as a force-sensor.

Next, to reveal the molecular mechanism of the high force resilience in protein-protein complex than in single-protein configuration, we performed an *in-silico* steered molecular dynamics (SMD) simulation by mimicking the HAP and PAP geometries. After performing SMD, we constructed the force-propagation pathway using the Dynamic Network Analysis plugin of VMD. For PAP geometry, we observed that force from Pcdh15 to Cdh23 propagated through an orthogonal pathway as previously reported and the network is widely spread among most of the β-strands for all the domains. This indicates that the force is distributed throughout the protein and therefore, resulting in more force dissipation. However, in the HAP mode of direct pulling, the force-propagation network is narrowly distributed among the β-strands. This implies that part of the protein through which the network passes will experience the entire force and hence more susceptible to unfold which corroborates with the AFM experimental studies. Furthermore, we also

observed that direct pulling resembles the single-point pulling whereas partner-based pulling is reminiscent of multi-point pulling which results in the more spreading of the entire force network and consequently more force-dissipation.

### 1.6 (b)Thesis motivation and perspective

Tip-links in the inner ear receive mechanical perturbation from sound stimuli and sense the force of 10-100 pN from a wide range of sound intensity and frequency. Tip-links must withstand these forces and maintain the complex integrity while simultaneously conveying the force to the ion-channel. Tip-links are proposed to serve as gating springs that gate the transduction channels. However, the gating spring nature of tip-links is not fully established. Several structural and *in-silico* studies reported the elastic nature within the individual proteins to support the gating spring nature of tip-links. Further, any gating spring should have an elastic component and a non-elastic component. The elastic components are referred to as spring and non-elastic components are referred to as dashpots. However, these components of the gating spring are not yet completely identified in the tip-links. To probe, we clamped the tip-links complex at various constant forces and monitored the molecular changes in tip-links that contribute to the viscoelasticity. With this viscoelastic nature, tip-links convey a threshold force to the ion-channel while dissipating the extra force.

First, we deciphered the force sensitivity of the complex itself. We explored the lifetime-force relationship of the tip-links binding interface comprising of two outermost domains of each protein and report a triphasic slip-catch-slip trend under force. In addition, molecular dynamics simulations and mutational studies reveal the molecular details of this unconventional bond behavior. Next, we estimated the contribution from the non-interacting domains onto the tip-links bond lifetime. Finally, we deciphered the effect of force on the heterotetrameric tip-links and proposed a gating spring model by identifying the spring and dashpots within the tip-links proteins.

## Bibliography


1. K. Huang, *Fundamental forces of nature: The story of gauge fields* (2007) https:/doi.org/10.1142/6447.
2. E. K. Paluch, *et al.*, Mechanotransduction: Use the force(s). *BMC Biol.* **13**, 1–14 (2015).
3. A. Dance, The secret forces that squeeze and pull life into shape. *Nature* (2021) https:/doi.org/10.1038/d41586-021-00018-x.
4. C. Bustamante, Y. R. Chemla, N. R. Forde, D. Izhaky, Mechanical processes in biochemistry. *Annu. Rev. Biochem.* **73**, 705–748 (2004).
5. P. G. Gillespie, R. G. Walker, Molecular basis of mechanosensory transduction. *Nature* **413**, 194–202 (2001).
6. S. Katta, M. Krieg, M. B. Goodman, Feeling Force: Physical and Physiological Principles Enabling Sensory Mechanotransduction. *Annu. Rev. Cell Dev. Biol.* **31**, 347–371 (2015).
7. M. D. Wang, *et al.*, Force and velocity measured for single molecules of RNA polymerase. *Science.* **282**, 902–907 (1998).
8. G. J. L. Wulte, S. B. Smith, M. Young, D. Keller, C. Bustamante, Single-molecule studies of the effect of template tension on T7 DNA polymerase activity. *Nature* **404**, 103–106 (2000).
9. A. Buxboim, *et al.*, Matrix elasticity regulates lamin-A,C phosphorylation and turnover with feedback to actomyosin. *Curr. Biol.* **24**, 1909–1917 (2014).
10. P. Lu, V. M. Weaver, Z. Werb, The extracellular matrix: A dynamic niche in cancer progression. *J. Cell Biol.* **196**, 395–406 (2012).
11. C. P. Heisenberg, Y. Bellaïche, Forces in tissue morphogenesis and patterning. *Cell* **153**, 948–962 (2013).
12. O. Campàs, *et al.*, Quantifying cell-generated mechanical forces within living embryonic tissues. *Nat. Methods* **11**, 183–189 (2014).
13. K. A. Jansen, *et al.*, A guide to mechanobiology: Where biology and physics meet. *Biochim. Biophys. Acta - Mol. Cell Res.* **1853**, 3043–3052 (2015).
14. S. Budday, P. Steinmann, E. Kuhl, Physical biology of human brain development. *Front. Cell. Neurosci.*, 1–17 (2015).
15. C. M. Hall, E. Moeendarbary, G. K. Sheridan, Mechanobiology of the brain in ageing and Alzheimer's disease. *Eur. J. Neurosci.* **53**, 3851–3878 (2021).
16. T. Kobayashi, M. Sokabe, Sensing substrate rigidity by mechanosensitive ion

channels with stress fibers and focal adhesions. *Curr. Opin. Cell Biol.* **22**, 669–676 (2010).

17. M. Sokabe, Y. Sawada, T. Kobayashi, Ion channels activated by mechanical forces in bacterial and eukaryotic cells. *Subcell. Biochem.* **72**, 613–626 (2015).

18. X. Qiu, U. Müller, Mechanically gated ion channels in mammalian hair cells. *Front. Cell. Neurosci.* **12**, 1–10 (2018).

19. G. Diez, V. Auernheimer, B. Fabry, W. H. Goldmann, Head/tail interaction of vinculin influences cell mechanical behavior. *Biochem. Biophys. Res. Commun.* **406**, 85–88 (2011).

20. A. Carisey, *et al.*, Vinculin regulates the recruitment and release of core focal adhesion proteins in a force-dependent manner. *Curr. Biol.* **23**, 271–281 (2013).

21. A. Del Rio, *et al.*, Stretching single talin rod molecules activates vinculin binding. *Science.* **323**, 638–641 (2009).

22. A. Elosegui-Artola, *et al.*, Rigidity sensing and adaptation through regulation of integrin types. *Nat. Mater.* **13**, 631–637 (2014).

23. A. M. Pasapera, I. C. Schneider, E. Rericha, D. D. Schlaepfer, C. M. Waterman, Myosin II activity regulates vinculin recruitment to focal adhesions through FAK-mediated paxillin phosphorylation. *J. Cell Biol.* **188**, 877–890 (2010).

24. K. Hayakawa, H. Tatsumi, M. Sokabe, Mechano-sensing by actin filaments and focal adhesion proteins. *Commun. Integr. Biol.* **5**, 572–577 (2012).

25. D. H. Kim, A. B. Chambliss, D. Wirtz, The multi-faceted role of the actin cap in cellular mechanosensation and mechanotransduction. *Soft Matter* **9**, 5516–5523 (2013).

26. Y. Chen, S. E. Radford, D. J. Brockwell, Force-induced remodelling of proteins and their complexes. *Curr. Opin. Struct. Biol.* **30**, 89–99 (2015).

27. J. Alegre-Cebollada, Protein nanomechanics in biological context. *Biophys. Rev.* **13**, 435–454 (2021).

28. H. Schwartze, The Pathological Anatomy of the Ear. *Am. J. Med. Sci.* (1879) https:/doi.org/10.1097/00000441-187904000-00029.

29. D. B. Webster, Ear structure and function in modern mammals. *Integr. Comp. Biol.* **6**, 451–466 (1966).

30. W. Zheng, J. R. Holt, The Mechanosensory Transduction Machinery in Inner Ear Hair Cells. *Annu. Rev. Biophys.* **50**, 31–51 (2021).

31. J. K. Weston, Notes on the comparative anatomy of the sensory areas of the vertebrate inner ear. *J. Comp. Neurol.* **70**, 355–394 (1939).

32. H. Engström, Microscopic anatomy of the inner ear. *Acta Otolaryngol.* **40**, 5–22 (1951).

33. S. Iurato, Submicroscopic structure of the membranous labyrinth - III. The supporting structure of Corti's organ (basilar membrane, limbus spiralis and spiral ligament). *Zeitschrift für Zellforsch. und Mikroskopische Anat.* (1962) https:/doi.org/10.1007/BF00326848.

34. A. Fridberger, *et al.*, Organ of corti potentials and the motion of the basilar membrane. *J. Neurosci.* **24**, 10057–10063 (2004).

35. C. D. West, The relationship of the spiral turns of the cochlea and the length of the basilar membrane to the range of audible frequencies in ground dwelling mammals. *J. Acoust. Soc. Am.* **77**, 1091–1101 (1985).

36. R. Nobili, F. Mammano, J. Ashmore, How well do we understand the cochlea? *Trends Neurosci.* **21**, 159–167 (1998).

37. P. Dallos, Cochlear amplification, outer hair cells and prestin. *Curr. Opin. Neurobiol.* **18**, 370–376 (2008).

38. P. Kazmierczak, U. Müller, Sensing sound: Molecules that orchestrate mechanotransduction by hair cells. *Trends Neurosci.* **35**, 220–229 (2012).

39. O. Nilsson, Observations on a type of cilia in the rat oviduct. *J. Ultrasructure Res.* **1**, 170–177 (1957).

40. Å. Flock, H. C. Cheung, Actin filaments in sensory hairs of inner ear receptor cells. *J. Cell Biol.* **75**, 339–343 (1977).

41. A. J. Hudspeth, How the ear's works work. *Nature* **341**, 397–404 (1989).

42. L. G. Tilney, M. S. Tilney, D. J. DeRosier, Actin filaments, stereocilia, and hair cells: How cells count and measure. *Annu. Rev. Cell Biol.* **8**, 257–274 (1992).

43. J. O. Pickles, S. D. Comis, M. P. Osborne, Cross-links between stereocilia in the guinea pig organ of Corti, and their possible relation to sensory transduction. *Hear. Res.* **15**, 103–112 (1984).

44. J. O. Pickles, *et al.*, The organization of tip links and stereocilia on hair cells of bird and lizard basilar papillae. *Hear. Res.* **41**, 31–41 (1989).

45. R. J. Goodyear, W. Marcotti, C. J. Kros, G. P. Richardson, Development and properties of stereociliary link types in hair cells of the mouse cochlea. *J. Comp. Neurol.* **485**, 75–85 (2005).

46. A. J. Hudspeth, Extracellular current flow and the site of transduction by vertebrate hair cells. *J. Neurosci.* **2**, 1–10 (1982).

47. M. Beurg, R. Fettiplace, J. H. Nam, A. J. Ricci, Localization of inner hair cell

mechanotransducer channels using high-speed calcium imaging. *Nat. Neurosci.* **12**, 553–558 (2009).

48. A. J. Hudspeth, Mechanoelectrical transduction by hair cells of the bullfrog' sacculus. *Prog. Brain Res.* **80**, 129–135 (1989).

49. J. O. Pickles, D. P. Corey, Mechanoelectrical transduction by hair cells. *Trends Neurosci.* **15**, 254–259 (1992).

50. B. Pan, *et al.*, TMC1 and TMC2 are components of the mechanotransduction channel in hair cells of the mammalian inner ear. *Neuron* **79**, 504–515 (2013).

51. R. Maeda, *et al.*, Tip-link protein protocadherin 15 interacts with transmembrane channel-like proteins TMC1 and TMC2. *Proc. Natl. Acad. Sci. U. S. A.* **111**, 12907–12912 (2014).

52. K. Kurima, *et al.*, TMC1 and TMC2 Localize at the Site of Mechanotransduction in Mammalian Inner Ear Hair Cell Stereocilia. *Cell Rep.* **12**, 1606–1617 (2015).

53. W. Xiong, *et al.*, TMHS is an integral component of the mechanotransduction machinery of cochlear hair cells. *Cell* **151**, 1283–1295 (2012).

54. S. Mahendrasingam, R. Fettiplace, K. N. Alagramam, E. Cross, D. N. Furness, Spatiotemporal changes in the distribution of LHFPL5 in mice cochlear hair bundles during development and in the absence of PCDH15. *PLoS One*, 12:e0185285 (2017).

55. B. Zhao, *et al.*, TMIE is an essential component of the mechanotransduction machinery of cochlear hair cells. *Neuron* **84**, 954–967 (2014).

56. X. Qiu, U. Müller, Mechanically gated ion channels in mammalian hair cells. *Front. Cell. Neurosci.* **12**, 1–10 (2018).

57. Y. Jia, *et al.*, TMC1 and TMC2 Proteins Are Pore-Forming Subunits of Mechanosensitive Ion Channels. *Neuron* **105**, 310–321 (2020).

58. C. L. Cunningham, *et al.*, TMIE Defines Pore and Gating Properties of the Mechanotransduction Channel of Mammalian Cochlear Hair Cells. *Neuron* **107**, 126–143 (2020).

59. B. Kachar, M. Parakkal, M. Kurc, Y. Zhao, P. G. Gillespie, High-resolution structure of hair-cell tip links. *Proc. Natl. Acad. Sci.* **97**, 13336–13341 (2000).

60. J. A. Assad, G. M. G. Shepherd, D. P. Corey, Tip-link Integrity and Mechanical Transduction in Vertebrate Hair Cells. *Neuron* **7**, 985–994 (1991).

61. J. M. Halbleib, W. J. Nelson, Cadherins in development: Cell adhesion, sorting, and tissue morphogenesis. *Genes Dev.* **20**, 3199–3214 (2006).

62. F. Di Palma, *et al.*, Mutations in Cdh23, encoding a new type of cadherin, cause

stereocilia disorganization in waltzer, the mouse model for Usher syndrome type 1D. *Nat. Genet.* **27**, 103–107 (2001).

63. J. M. Bork, *et al.*, Usher syndrome 1D and nonsyndromic autosomal recessive deafness DFNB12 are caused by allelic mutations of the novel cadherin-like gene CDH23. *Am. J. Hum. Genet.* **68**, 26–37 (2001).

64. L. M. Astuto, *et al.*, CDH23 mutation and phenotype heterogeneity: A profile of 107 diverse families with Usher syndrome and nonsyndromic deafness. *Am. J. Hum. Genet.* **71**, 262–275 (2002).

65. Z. M. Ahmed, *et al.*, PCDH15 is expressed in the neurosensory epithelium of the eye and ear and mutant alleles are responsible for both USH1F and DFNB23. *Hum. Mol. Genet.* **12**, 3215–3223 (2003).

66. J. Siemens, *et al.*, Cadherin 23 is a component of the tip link in hair-cell stereocilla. *Nature* **428**, 950–955 (2004).

67. P. Kazmierczak, *et al.*, Cadherin 23 and protocadherin 15 interact to form tip-link filaments in sensory hair cells. *Nature* **449**, 87–91 (2007).

68. M. Sotomayor, W. Weihofen, R. Gaudet, D. P. Corey, Structure of a Force-Conveying Cadherin Bond Essential for Inner-Ear Mechanotransduction. *Nature* **492**, 128–132 (2012).

69. M. Sotomayor, W. A. Weihofen, R. Gaudet, D. P. Corey, Structural Determinants of Cadherin-23 Function in Hearing and Deafness. *Neuron* **66**, 85–100 (2010).

70. R. Araya-Secchi, B. L. Neel, M. Sotomayor, An elastic element in the protocadherin-15 tip link of the inner ear. *Nat. Commun.* **7**, 1–14 (2016).

71. R. E. Powers, R. Gaudet, M. Sotomayor, A Partial Calcium-Free Linker Confers Flexibility to Inner-Ear Protocadherin-15. *Structure* **25**, 482–495 (2017).

72. A. Jaiganesh, *et al.*, Zooming in on Cadherin-23 : Structural Diversity and Potential Mechanisms of Inherited Deafness. *Structure* **26**, 1–16 (2018).

73. D. Choudhary, *et al.*, Structural determinants of protocadherin-15 mechanics and function in hearing and balance perception. *Proc. Natl. Acad. Sci. U. S. A.* **117**, 24837–24848 (2020).

74. W. L. DeLano, Pymol: An open-source molecular graphics tool. *{CCP4} Newsl. Protein Crystallogr.* (2002).

75. K. Arnold, L. Bordoli, J. Kopp, T. Schwede, The SWISS-MODEL workspace: A web-based environment for protein structure homology modelling. *Bioinformatics* **22**, 195–201 (2006).

76. S. K. Bosher, R. L. Warren, Very low calcium content of cochlear endolymph, an

extracellular fluid. *Nature* **273**, 377–378 (1978).

77. A. N. Salt, N. Inamura, R. Thalmann, A. Vora, Calcium gradients in inner ear endolymph. *Am. J. Otolaryngol. Neck Med. Surg.* **10**, 371–375 (1989).

78. P. De-la-Torre, D. Choudhary, R. Araya-Secchi, Y. Narui, M. Sotomayor, A Mechanically Weak Extracellular Membrane-Adjacent Domain Induces Dimerization of Protocadherin-15. *Biophys. J.* **115**, 2368–2385 (2018).

79. B. Honig, *et al.*, Mechanotransduction by PCDH15 Relies on a Novel cis-Dimeric Architecture. *Neuron* **99**, 480–492 (2018).

80. D. P. Corey, A. J. Hudspeth, Kinetics of the receptor current in bullfrog saccular hair cells. *J. Neurosci.* **3**, 962–976 (1983).

81. U. Muller, P. G. Gillespie, Mechanotransduction by Hair Cells: Models, Molecules, and Mechanisms. *Cell* **139**, 33–44 (2010).

82. J. Howard, A. J. Hudspeth, Compliance of the hair bundle associated with gating of mechanoelectrical transduction channels in the Bullfrog's saccular hair cell. *Neuron* **1**, 189–199 (1988).

83. M. Tobin, A. Chaiyasitdhi, V. Michel, N. Michalski, P. Martin, Stiffness and tension gradients of the hair cell's tip-link complex in the mammalian cochlea. *Elife*, 497222 (2019).

84. M. Sotomayor, D. P. Corey, K. Schulten, In search of the hair-cell gating spring: Elastic properties of ankyrin and cadherin repeats. *Structure* **13**, 669–682 (2005).

85. M. LeMasurier, P. G. Gillespie, Hair-cell mechanotransduction and cochlear amplification. *Neuron* **48**, 403–415 (2005).

86. A. Basu, S. Lagier, M. Vologodskaia, B. A. Fabella, A. J. Hudspeth, Direct mechanical stimulation of tip links in hair cells through DNA tethers. *Elife* **5:e16041**, 1–10 (2016).

87. A. J. Hudspeth, Hair-bundle mechanics and a model for mechanoelectrical transduction by hair cells. *Soc. Gen. Physiol. Ser.* **47**, 357–370 (1992).

88. M. Schwander, B. Kachar, U. Müller, The cell biology of hearing. *J. Cell Biol.* **190**, 9–20 (2010).

89. T. F. Bartsch, F. E. Hengel, A. Oswald, G. Dionne, I. V Chipendo, The elasticity of individual protocadherin 15 molecules implicates cadherins as the gating springs for hearing. *Proc. Natl. Acad. Sci.* **116**, 11048–11056 (2018).

90. N. Arora, J. P. Hazra, S. Rakshit, Anisotropy in mechanical unfolding of protein upon partner-assisted pulling and handle-assisted pulling. *Commun. Biol.* **4**, 1–10 (2021).

91. J. P. Hazra, *et al.*, Broken force dispersal network in tip-links by the mutations induces hearing-loss. *Biochem. J.* **476**, 2411–2425 (2019).

92. E. M. Mulhall, *et al.*, Single-molecule force spectroscopy reveals the dynamic strength of the hair-cell tip-link connection. *Nat. Commun.* **12**, 1–15 (2021).

# Chapter 2

Tip-links follow slip-catch-slip by transitioning into a stronger binding conformation

## 2.1 Introduction

*Homo sapiens* perceive sound in the frequency range of 20 Hz-20 kHz and amplitude range of 5 dB-120 dB(1). Listening to a sound of above 80 dB is harmful to the ear whereas beyond 120 dB (from jet planes or music concerts) can cause irreversible damage. Further, excessive exposure to intense sound can also accelerate age-related hearing loss (ARHL). The varying intensity of sound exerts a force of 10-100 pN on tip-links in the perceived frequency range(2). Accordingly, the tip-links must withstand this range of force to remain functional. In the past few years, many *in-silico* and experimental studies have been performed to delineate the force-induced survival of tip-links(3, 4). In 2021, a single-molecule study estimated the average lifetime of tip-links under resting force (~10 pN) as ~8 s(5). Moreover, the lifetime of tip-links drops exponentially with force when pulled at low velocity, indicating the nearly disappearing existence of tip-links in a nightclub or from a jet plane. Studies that disrupt the tip-links with BAPTA, showed that regeneration of tip-links without any stimulation takes 12 h-36 h(6). Thus, reformation of tip-links after disruption is a time-expensive affair, considerably due to the spatial localization of the complex at the tip of stereocilia. It is thus intriguing to decipher the bond-lifetime dynamics of tip-links that survive the periodic shearing forces at high-frequency and amplitude.

With an overarching objective to decipher the bond lifetime dynamics of tip-links complex at varying mechanical perturbations, here we perform the single-molecule force-clamp spectroscopy on tip-links using atomic force microscopy (AFM)(7). The use of AFM is significant in achieving the higher force-loading rates that result in higher forces equivalent to the loud sound. Force-clamp spectroscopy has extensively been used to understand the force-mediated lifetime evolution of protein-protein and protein-ligand complexes(8, 9). It has also been successful in explaining critical physiological phenomena like flow-induced blood clotting(10), shear-enhanced bacterial adhesion(11), cell-cell adhesion(12), etc. Force-mediated lifetime evolution is of three types, slip, catch, and ideal(13). Nature has designed these three types of force-responsive modules to effectively regulate various physiological activities. Slip bonds, a monotonous decrease in a bond lifetime with the

increasing force, are common and found in most biological interactions. Counter-intuitive to slip is catch bonds, that show increasing bond-lifetime with increasing tensile force. On contrary, ideal bonds are insensitive to the tensile force.

As the tip-links bond is mediated by the interaction between two outermost domains of both the proteins Cdh23 and Pcdh15(3), therefore, we first intended to examine the force-dependent bond lifetime dynamics of the interacting domains. This approach exclusively delineates the response of the binding interface under tension. Further, we investigated the molecular reason for the observed bond nature by employing *in-silico* studies. In addition, we verified the effect of mutation associated with hearing loss in humans on the bond-lifetime dynamics.

## 2.2 Experimental Section

### 2.2.1 Cloning, expression, and purification of Cdh23 EC1-2 and Pcdh15 EC1-2

Two N-terminal domains of both the tip-links proteins, mouse Cdh23 EC1-2 (Q24 to D228 in NP_075859.2) and Pcdh15 EC1-2 (Q27 to D259 in NP_001136218.1) were cloned into Nde1 and Xho1 restriction sites of pET21a vector (Novagen, Merck). We recombinantly modified the N-terminus with 6xHis-tag for affinity-based protein purification and the C-terminus with sortase-tag (LPETGG) for covalent attachment on the surface. Both the constructs were successfully cloned and verified by DNA sequencing. Recombinantly cloned genes were expressed in the Lemo21(DE3) (Stratagene) strain of *E.coli* to optimize the expression of proteins in the soluble form(4). Cells were cultured in Luria Bertani broth (LB) media and grown at 37ºC at 180 RPM. 1 mM L-Rhamnose (MP Biomedicals) was added to the cells when grown with an optical density (OD) of 0.4. When OD reached 0.6, cells were induced with 200 µM of Isopropyl-β-D-1-thiogalactopyranoside (IPTG) and kept at 16ºC for 16 h in the incubator. Cells were centrifuged at 7000 RPM and lysed using sonication in the resuspension buffer containing 25 mM HEPES, 100 mM NaCl, 50 mM KCl and 2 mM $CaCl_2$; pH 7.5 (all from Hi-Media). After sonication, cell lysate was separated from the inclusion body by centrifuging at 10,000 RPM at 4 ºC for 30 min.

Inclusion bodies were resuspended into 8M urea. Protein expression was checked in both cytosol and inclusion bodies by running SDS-PAGE gel electrophoresis. We observed the presence of desired proteins in both the samples, however, significantly less amount in the cytosol. We purified the proteins from cell-lysate using Ni-NTA agarose beads by three times sequential loading, and then washing, and finally collected the elutions in the same HEPES buffer with 50, 100, 200, and 500 mM concentrations of imidazole. Proteins were further purified by using size-exclusion chromatography on Superdex-200 column (GE Healthcare) in SEC buffer with 25 mM HEPES, 50 mM KCl, 100 mM NaCl, 2 mM $CaCl_2$, pH 7.5. Protein was detected by monitoring the UV absorbance at 280 nm and subsequently, peak fractions were collected separately. The purity of the collected protein fractions was checked on 12% SDS-PAGE.

Mutation R113G in Pcdh15 EC1-2 was engineered using overlapping extension PCR. Protein expression and purification were carried out by using the same mentioned protocol as for wild-type (WT) proteins.

### 2.2.2 Surface modification for single-molecule force spectroscopy (SMFS)

To perform a single-molecule AFM experiment, glass coverslips were first activated using air plasma for 30 s. Next, coverslips were cleaned by incubating in piranha solution (3 parts $H_2SO_4$: 1part 30% $H_2O_2$) for 2 h. After that, surfaces were then washed thoroughly with Milli-Q water (MQ) in a bath sonicator, 3 times for 10 min each. Surfaces were then etched with 1M KOH for 15 min and subsequently washed with MQ water by sonicating for 10 min, 4 times. Cleaned surfaces were silanized using 2% APTES (3-Aminopropyltriethoxy silane) in 95% acetone for 30 min and cured at 110ºC for 1 h in a vacuum oven. Amine exposed surfaces were functionalized with polyethylene glycol (PEG), as a mixture of 10% bi-functional, Maleimide-PEG-Succinimide (Mal-PEG-NHS) in mono-functional methyl-PEG Succinimide (mPEG-NHS) in 100 mM $NaHCO_3$ and 600 mM $K_2SO_4$, pH 8.0 for 4h at room temperature. PEGylated surfaces were washed with MQ water to remove unreacted PEG and subsequently treated with polyglycine solution (GGGGC) for 7 h at room temperature. Here, thiol group of cysteine reacts with the exposed maleimide group on the

surface and mediates the attachment of peptide GGGG onto the surface. This peptide act as a nucleophile for sortase A based transpeptidation reaction to covalently attach the proteins (bearing –LPETG at C-terminus) on the surface and cantilever(14).

The $Si_3N_4$ cantilever was silanized and functionalized similarly but excluded the steps of piranha cleaning and KOH treatment. Modified surfaces and cantilever were stored in a vacuum desiccator before further use.

We covalently attached the C-terminus of Cdh23 EC1-2 on the surface and Pcdh15 EC1-2 on the cantilever using sortase-A mediated enzymatic reaction. For this, we made a mixture of protein and sortase A (in a molar ratio of 4:5) in SEC buffer and incubated the surface and cantilever with that protein mixture for 1 h. Afterward, we gently washed the surface with buffer to remove any unreacted protein mixture. In a sortagging reaction, Sortase A active-site attacked the peptide bond between threonine and glycine in LPETG and make a thioester intermediate which then undergoes a nucleophilic reaction by –NH2-GGGG present on the surface. After attaching the proteins onto the surface and cantilever we performed single-molecule force spectroscopy in force-clamp mode.

### 2.2.3 Single-molecule force clamp spectroscopy and data-analysis

The two most common method to perform force spectroscopy using AFM is a force-ramp and force-clamp mode(15, 16). In force-ramp, the biomolecules are stretched with a constant pulling velocity, and effect of the resulting mechanical force is studied. In this mode, the separation between the sample and cantilever linearly varies with time. Another way to study the effect of force was introduced by group of Prof. Julio Fernandez where individual molecules or pair of the protein complex is clamped at a constant mechanical force and subsequently, unbinding time of the ligand-receptor complex or unfolding time of each module of polyprotein chain is monitored at that constant force. It involves a PID (Proportional-integral-derivative) feedback system that maintains the desired constant force throughout the experiment(17).

For our experiment, force-clamp spectroscopy was performed using Atomic Force Microscope (AFM) (Nano wizard 3, JPK Instruments, Germany). The spring constant of

the cantilever was determined using the equipartition-based thermal fluctuation method prior to the experiment(18). After modifying the surface and cantilever with the proteins of interest, the cantilever was approached towards the surface to interact with its partner. We let the proteins interact for 1 s, thereafter, retracted the cantilever by 20 nm to break any non-specific interactions and clamped at a certain constant force for 10 s until the bond dissociation occurred, and then finally retracted the cantilever to break all the remaining bonds formed. AFM experiments have been performed in the buffer with 25 mM HEPES, 100 mM NaCl, 50 mM KCl and 50 µM $CaCl_2$. We repeated the experiment at different points on the surface and recorded around 2,000 force curves at each clamping force to get statistically significant data. For the control experiment, force-clamp data was recorded in the buffer without any calcium i.e. 25 mM HEPES, 100 mM NaCl, 50 mM KCl along with 1 mM EGTA. We found that in absence of calcium, the event rate decreased to ~0.5-1% from 6-8% in the presence of calcium. This indicates that our measurements are specific to the interaction of tip-links cadherins.

We estimated the survival of the bond as the difference between the time when clamping force is reached and when spontaneously the bond dissociates. This persistence time of the bond gives the bond lifetime. We pooled all the data and divided it into force bins. Thereafter, we plotted the survival plot at each force bin as the number of intact bonds vs. time. And determined the bond survival probability using the equation; $P(t) = \sum_i P_i(0) \times e^{\frac{-t}{\tau_i}}$, where $\tau$ is the bond lifetime. The exponential fit of the survival probability gives the bond lifetime at a particular clamping force.

### 2.2.4 Molecular dynamics simulations

We used the crystal structure of the complex of EC1-2 domains of Cdh23 and Pcdh15 (PDB ID 4AQ8)(3) as the starting structure for MD simulations. The simulation setup was made with Charmm-GUI(19, 20) using Charmm36 force field(21) along with the TIP3P water model(22). The protein complex was immersed in a water box with dimensions 7.2 x 7.2 x 15 nm with all angles equal to 90°. The long axis of the complex was aligned to the

X-axis of the box. The system was neutralized, and the final salt concentration was set to 0.15 M using sodium and chloride ions. The simulations were run using GROMACS 2020.4(23) patched with PLUMED 2.7.4 which is an open-source sampling library(24, 25). We used periodic boundary conditions and restrained the bonds involving hydrogen atoms using the LINCS algorithm(26). The Particle Mesh Ewald method was used for calculating electrostatic interactions with a cutoff of 1.2 nm for long-range interactions(27). The system was minimized for 10,000 steps using the steepest descent algorithm followed by NVT equilibration for 5 ns with restraints on the protein backbone. This was followed by Infinite Switch Simulated Tempering in Force (FISST) simulations(28) under the NPT ensemble using the X-component of the distance between the C-terminal residues of Cdh23 and Pcdh15 as the collective variable. We used a force range of 10 to 150 pN with 61 interpolated points. The temperature was maintained at 303.15 K using a Nose-Hoover thermostat and for NPT simulations, the pressure was maintained at 1 bar using a Parrinello-Rahman barostat.

The end-to-end distance was calculated using PLUMED and the buried surface area was calculated using the sasa module of VMD. The weighted histograms for distance and buried surface area were generated using the scripts available with the PLUMED-NEST entry (plumID:20.017). The frames corresponding to different force ranges were separated using python scripts employing MDAnalysis(29). The inter-protein interactions including salt-bridges, hydrogen bonds, and hydrophobic interactions were calculated using PyInteraph(30). The pairwise residue forces were calculated using gromacs-fda (release 2020)(31) and written as signed scalars calculated by taking the norm of the force vector with the sign of the force determined based on the cosine of the angle between the force vector and vector joining the centers of masses of the two residues.

### 2.2.5 Kinetic model fitting using Force-induced stronger-binding model

We modified the already existing sliding-rebinding model(32) to fit our triphasic force-lifetime data and defined two pathways for dissociation of the complex. One pathway involves the force-induced conformational transition to a stronger binding interface. The

other pathway is the direct dissociation of the heteromeric complex. We introduced two critical forces $F_{C1}$ and $F_{C2}$ (Eq 1). $F_{C1}$ corresponds to the minimum threshold force for slip-to-catch transition while $F_{C2}$ is the force after which a second slip started to appear. When the applied force is less than $F_{C1}$, no slip-to-catch transition would occur and the complex will directly unbind while above $F_{C1}$, unbinding occurs through an alternate pathway where sliding or conformational rearrangement is followed by enhanced binding that results in the observed catch behavior.

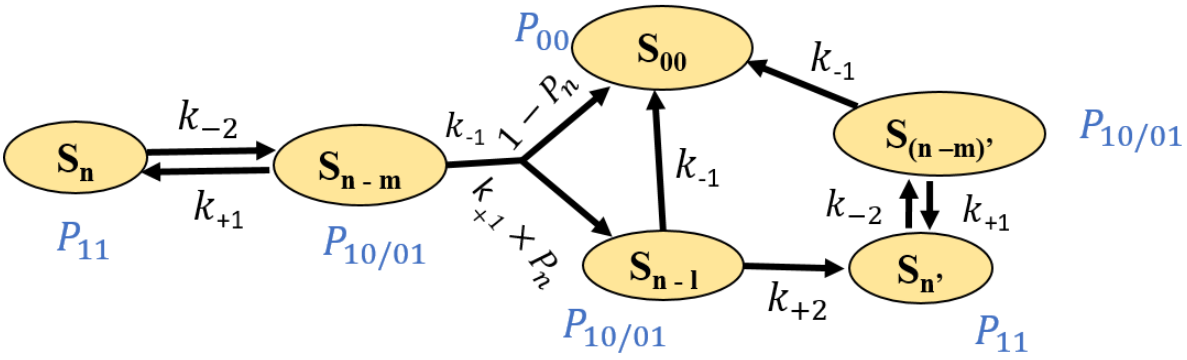


**Scheme 1: Schematic representation of the modified sliding-rebinding model to fit the slip-catch-slip bond transition.** We considered the n pairs of pseudoatoms to describe the non-covalent interactions between the two protomers of tip-links. This corresponds to the initial $S_n$ state in the model. Under the force application, m bonds break with an off-rate of $k_{-2}$, and the complex transitions to a $S_{n-m}$ state. Further, from this $S_{n-m}$ state, there are two pathways, either the complex undergoes a completely dissociated state ($S_{00}$) or to a stronger-binding state ($S_{n'}$) through a force-induced conformational re-arrangement ($S_{n-l}$) of the complex. Transition to the re-arranged state depends on the rate $k_{+1}$ and the probability of new bond formation ($P_n$) within the complex. Finally, from the stronger binding-state $S_{n'}$, the complex will eventually unbind at higher forces. For each state, the corresponding probability (blue) and rates are mentioned.

For simplicity, we have solved the analytical equations for two pairs of pseudoatoms where the kinetic rate equations for the probability of different states are:

$$\frac{dP_{11}}{dt} = 2k_{+1}P_{10} + k_{+2}P_{01} - k_{-2}P_{11}$$
$$\frac{dP_{10}}{dt} = k_{-2}P_{11} - 2(k_{+1} + k_{-1})P_{10}$$
$$\frac{dP_{01}}{dt} = 2p_n k_{-1}P_{10} - (k_{+2} + k_{-1})P_{01}$$
$$\frac{dP_{00}}{dt} = 2(1 - p_n)k_{-1}P_{10} + k_{-1}P_{01}$$

$k_{+1}$ and $k_{+2}$ is constant association rate and $k_{-1}$ is the force-dependent dissociation rate that followed the Bell equation(33):

$$k_{-1}(f) = k_{-1}^{0} \times exp\left(f \times \frac{x_\beta}{k_B T}\right)$$

$$k_{-2}(f) = 2.k_{-1}^{0} \times exp\left(f \times \frac{x_\beta}{2k_B T}\right)$$

$k_{-1}^{0}$ is the zero-force off-rate and $x_\beta$ is the distance from the bound state to the transition state. The probability ($P_n$) of making new bonds and undergoing to a stronger-binding state is defined as follows:

$$P_n = 0 \qquad 0<F<F_{C1}$$
$$P_n = \left\{0.5\left[1 + sin\left(\frac{\pi F}{F_{c2}} - \frac{\pi}{2}\right)\right]\right\}^n \qquad F_{C1}<=F<=F_{C2} \qquad (1)$$
$$P_n = 1 \qquad F>F_{C2}$$

Here, n is the fitting parameter, and $F_{C1}$, $F_{C2}$ are the critical forces that define the first slip-to-catch transition and catch-to-second slip transition respectively. Probability rate equations were solved analytically by a nonlinear least-squares curve-fitting algorithm using MATLAB and survival probability was estimated as:

$$1 - P_{00} = P_{11} + P_{10} + P'_{10}$$

## 2.3 Results

### 2.3.1 Tip-links binding interface follow triphasic slip-catch-slip transition with force

To elucidate the lifetime dynamics of tip-links with two outermost domains that mediate tip-links interaction, we performed AFM-based single-molecule force clamp spectroscopy.

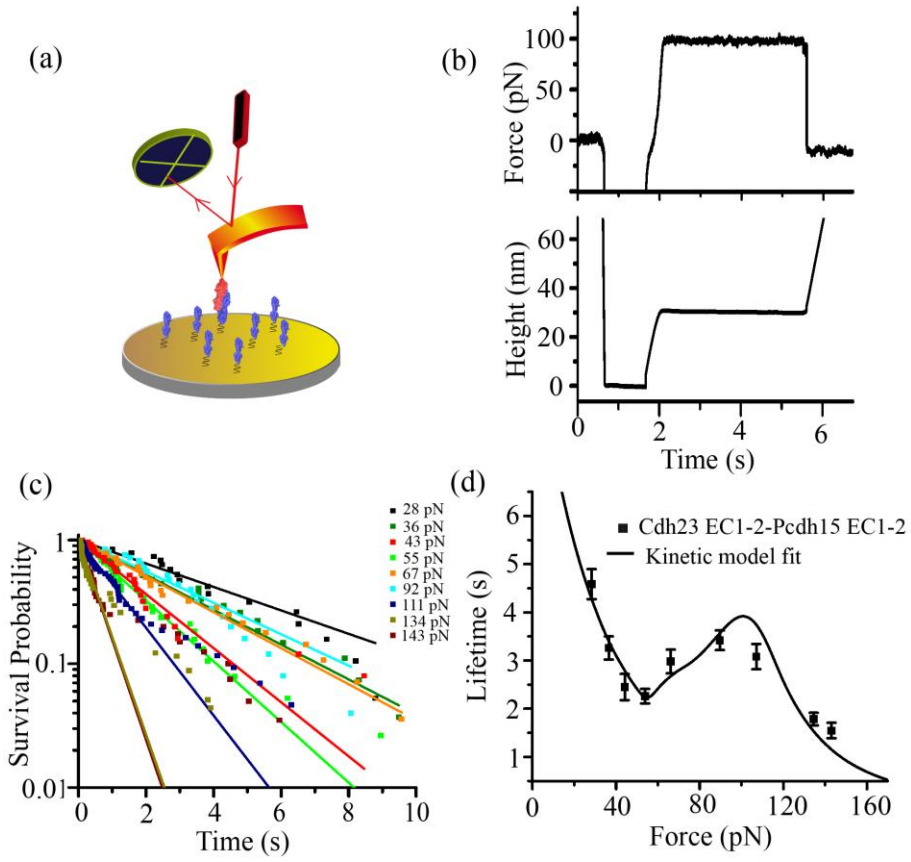


**Figure 1: Tip-links follow triphasic slip-catch-slip under tension.** (a) Schematic representation of the AFM-based force-clamp experiment. Pcdh15 EC1-2 (red) is covalently attached to the cantilever and Cdh23 EC1-2 (blue) is attached to the surface. (b) Typical force vs. time (top) and height vs. time (bottom) graphs respectively obtained from the clamp measurements. (c) Lifetime measurements have been carried out at each clamping force multiple times to obtain statistically significant data and then determined the bond survival probability. (d) The force-dependent lifetime evolution of the tip-link complex (black squares) shows a triphasic slip-catch-slip behavior indicating that lifetime first decreases at lower forces and then increases after a threshold force and eventually decreases again at higher forces. The black solid line represents the corresponding kinetic model fit (discussed in section 2.3.5).

We immobilized the C-terminus of Pcdh15 EC1-2 on the cantilever and Cdh23 EC1-2 on the surface using sortase A-mediated sortagging protocol **(Figure 1a, methods**). We bring the two proteins together, let them interact, and then clamped the interacting complex at a constant force. We monitored the force-tolerance time of the tip-link complex for each successful clamping event. We repeated the force clamp measurements multiple times at the same constant force scanning through different regions on the surface. Similarly, we performed the experiment at different clamping forces to delineate the force-mediated lifetime evolution. We plotted the survival probability at each clamping force and subsequently fit it using the exponential decay model **(Figure 1c**). From the statistical F-test, we determined that the survival probability followed single-exponential decay. We subsequently measured the mean-lifetime of tip-links from the survival probability at all the varying clamping forces and obtained the numeric relation for force-lifetime of the complex.

We observed that the lifetime of the complex follows a triphasic behavior with clamping force (**Figure 1d**). Initially, the complex lifetime drops monotonously with increasing force, featuring a slip bond where the bond weakens with the applied force. The slip bond is consistent with previous results obtained from the optical tweezer measurements at a low-force regime for slow force-loading rates(5). Further, above a critical force ($F_{C1}$) of 52 pN, the bond-lifetime increases and reaches maxima at a critical force ($F_{C2}$) of 90 pN, featuring catch-bond behavior. Catch-bond is counterintuitive where the bond strengthens with the force and increases the bond lifetime. Furthermore, beyond 90 pN, the lifetime decreases monotonously with further force elevation, indicating a slip-type behavior again. So, the bond-lifetime of the complex does not monotonously slip with force but rather follows a roller-coaster ride of slip-catch-slip bonds. A transition from slip to catch above a critical force of 52 pN, certainly elevates the survival of tip-links at loud noise.

### 2.3.2 Molecular details shed light on the slip-catch-slip transition

To understand the effect of force on the molecular interactions between Cdh23 and Pcdh15, we performed Steered Molecular Dynamics (SMD) simulations* using the Infinite Switch Simulated Tempering in Force approach (FISST). FISST is simulated tempering in force in an infinite switch limit. It is a collective variable based enhanced sampling tool which is computationally relatively inexpensive. It involves a random walk on a force ladder with various transition step sizes. Before the simulation starts, there is a learning phase in which the weights are optimized based on the collective variable. Optimization of weights is important to sample all the forces with equal probability and therefore, create a random walk. Further, weights are used to compute the average of a structural quantity within the simulated force range.

We applied constant forces in the range of 10 to 150 pN using the X component of the end-to-end distance as the collective variable (with the long axis of the complex aligned to the X-axis). The complex was stable under this range of forces in the time scale of microseconds. Therefore, the application of this range of forces doesn't cause the complex to dissociate or the proteins to unfold but alters the energetic landscape which is sampled by FISST simulations. We estimated the force-induced variation in inter-domain angles of both the proteins and subsequent alterations in the buried surface area of the tip-link complex with force (**Figure 2a**). Interestingly, we observe a shift to larger buried surface area concomitantly with an increase in the applied force. Additionally, at intermediate forces of 40-90 pN, we observe the appearance of conformations with a much larger buried surface area than seen without the application of force. An increase in the buried surface area implies the strengthening of the complex in response to the applied force in agreement with the slip-to-catch transition as measured experimentally. Further, we calculated the differential per-residue buried surface area for the force range of 70-80 pN (compared to 10-20 pN). We observe that the residues on EC1 and EC2 domains as well as the N-termini of both proteins get more buried on the application of force **(Figure 2b**). Unlike experiments, we did not observe any SMD feature that explains the slip-behaviour of tip-

** All the SMD simulations have been performed in collaboration with Dr. Amin Sagar from University of Montpellier, France*

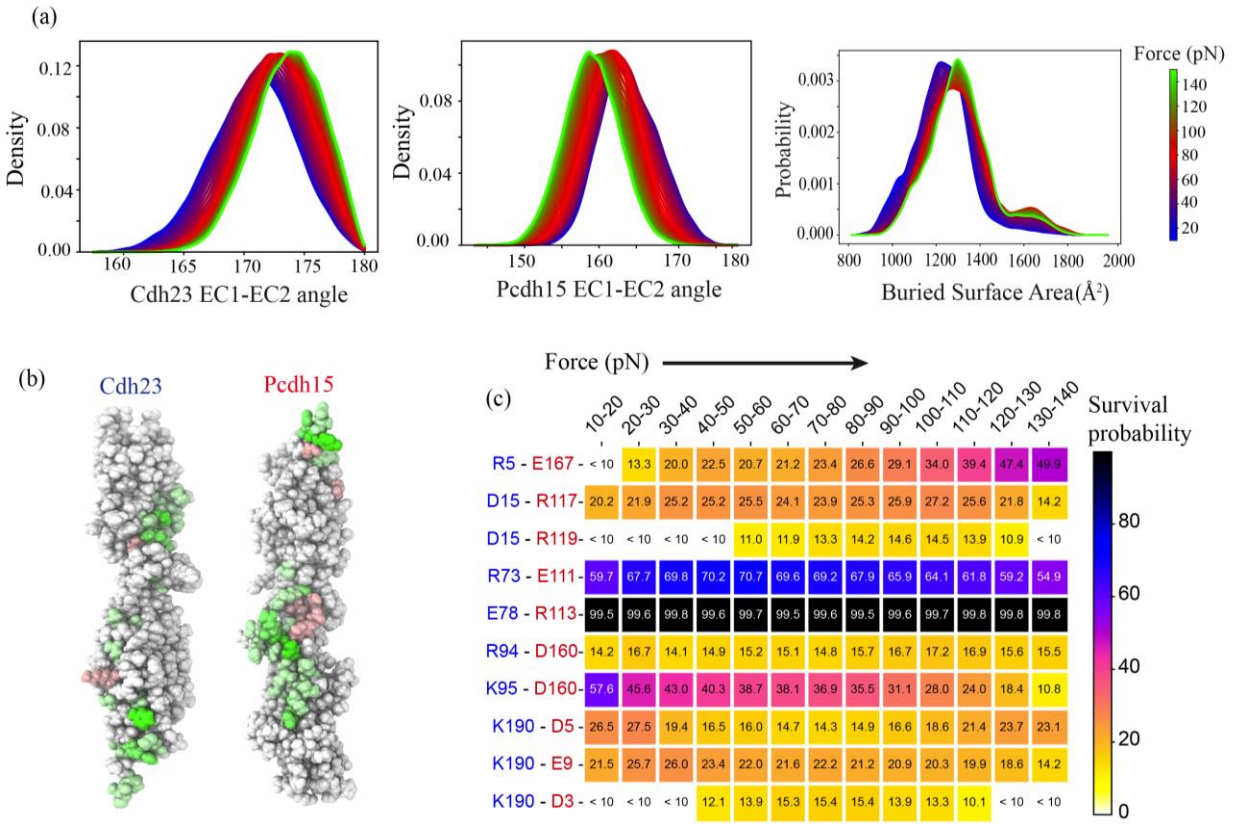


**Figure 2: Force-dependent behavior of Cdh23-Pcdh15 complex.** (a) The distributions of buried surface area at the 61 interpolated points between the force range of 10 and 150 pN from FISST simulations. (b) The per-residue differential buried surface area is calculated by subtracting the buried surface area at the 10-20 pN force range from the 70-80 pN force range. The residues with the positive differential buried surface area are colored green with darker shades representing higher values. The residues colored red show a negative differential buried surface area with darker shades representing larger negative values. (c) The percentage of frames showing the existence of specified salt-bridges at varying force ranges. Here, residue pair on the left side indicate the salt bridge between Cdh23 (blue) and Pcdh15 (red).

links at low force regime. The absence of a slip phase in the MD simulations could be because of the formation of a weaker initial encounter complex in the force-clamp experiments which settles into a conformation similar to the crystal structure at very low forces. Such a transition would not be seen in our simulations as we start from the crystal structure. To understand the molecular interactions that are stabilized by the tension, we

calculated the probability of the formation of salt-bridges, hydrogen bonds, and hydrophobic interactions between Cdh23 and Pcdh15 at the force range of 10 - 140 pN in steps of 10 pN (**Figure 2c)**. We observe that the salt-bridge between Pcdh15-R113 and Cdh23-E78 remained intact at all forces emphasizing its importance in the stability of the complex **(Figure 2c)**. Interestingly, the probability of all the salt-bridges increases slightly

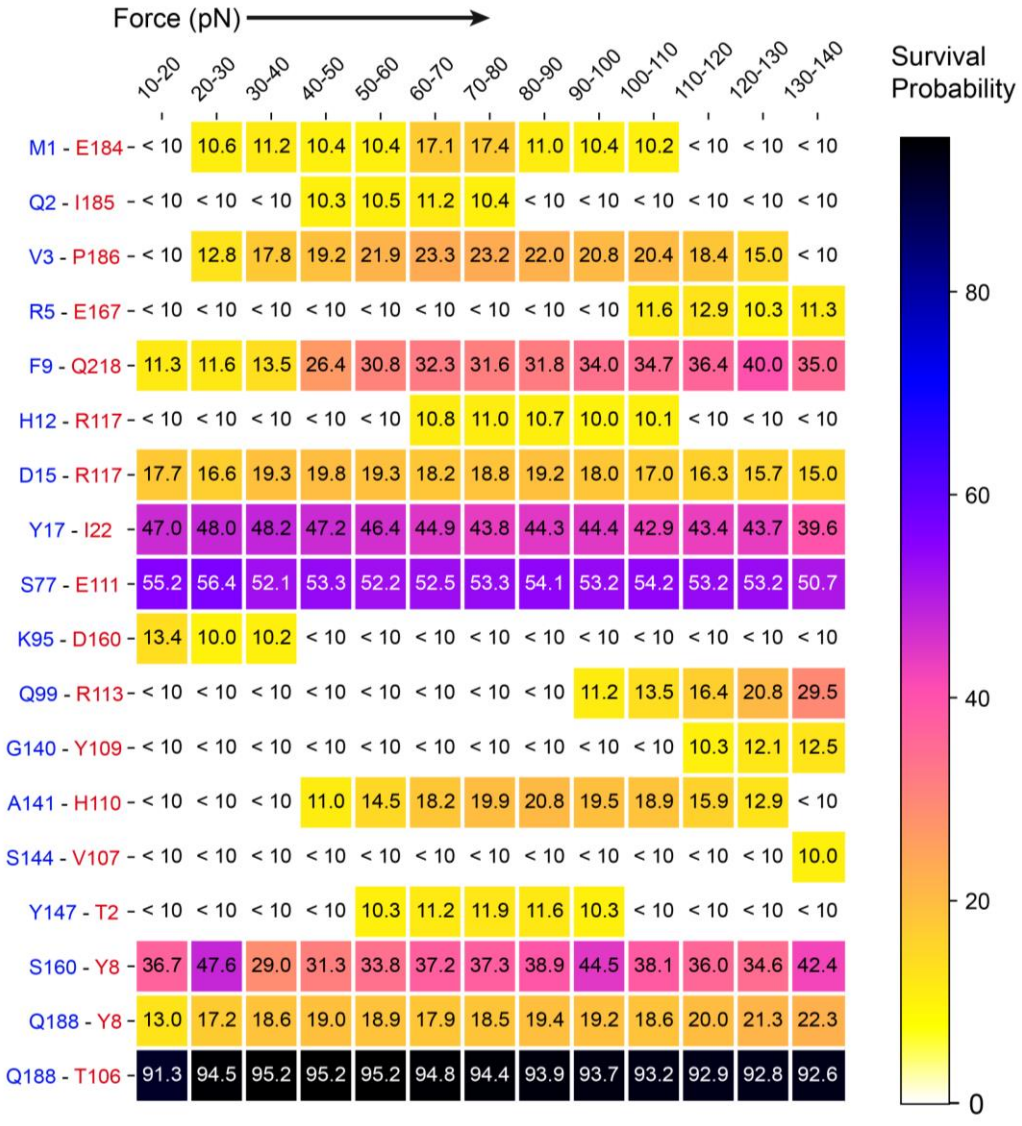


**Figure 3: Percentage of frames showing the hydrogen bonds at varying force ranges**. Hydrogen-bond survival between various residues pairs of Cdh23 and Pcdh15 with varying force.

at small forces of 20-30 pN. At higher forces, some of the salt-bridges, viz. K95(Cdh23)-D160(Pcdh15), K190(Cdh23)-D5(Pcdh15), and K190(Cdh23)-E9(Pcdh15) became weaker with force (less probable). On the other hand, other salt-bridges viz. R73(Cdh23)-E111(Pcdh15) and R5(Cdh23)-E167(Pcdh15) became stronger (more probable) with increasing force. Additionally, new salt-bridges appear at higher forces that are either absent or present in a negligible number of frames at low forces. This includes R5(Cdh23)-E167(Pcdh15), K190(Cdh23)-D3(Pcdh15), and D15(Cdh23)-R119(Pcdh15). Similarly, some of the hydrogen bonds between the EC1 domain of one partner and the EC2 domain of the other also became more probable at higher forces including V3(Cdh23)-P186(Pcdh15), F9(Cdh23)-Q218(Pcdh15) and Q188(Cdh23)-Y8(Pcdh15) (**Figure 3)**. A similar trend is seen for the hydrophobic interaction between V3(Cdh23)-L187(Pcdh15) **(Figure 4)**.

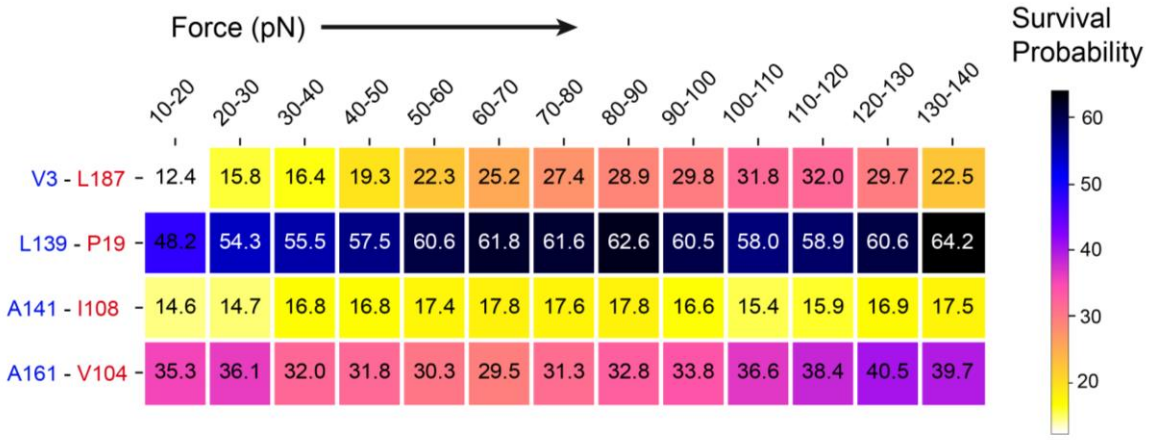


**Figure 4: Percentage of frames showing the hydrophobic interactions at varying force ranges.** Survival of hydrophobic interactions between various residues pairs of Cdh23 and Pcdh15 with varying force.

### 2.3.3 Dynamic force balancing protects the essential interactions in the Cdh23-Pcdh15 complex

The salt-bridge between R113(Pcdh15) and E78(Cdh23) remains unaltered in the entire clamping force and as a pivot, might be influencing the slip-to-catch switch under tension.

To understand the mechanics that conserve the pivotal role of this salt-bridge interaction at a large range of tension, we quantified how force is stored and transmitted in the complex. We estimated the pairwise inter-residue force distributions for each clamping force range. At the clamping force of 10-20 pN, which are extremely small forces for this complex, the two most important inter-protein salt-bridges i.e., R73(Cdh23) – E111 (Pcdh15) and E78(Cdh23) – R113(Pcdh15) are most tensed (**Figure 5a**) i.e., they tend to pull the proteins closer. Interestingly, the salt-bridge between E78(Cdh23) – R113(Pcdh15) maintains a constant degree of tension across the entire loading force (**Figure 5b**). A bond bearing a constant tension across large tensile forces indicates a form of load balancing activity inside the protein complex. This load balancing drives the force away from this critical interaction. On the other hand, the force between Cdh23(R73) – Pcdh15(E111) gradually becomes less negative with the applied force, indicating that this interaction will break at higher forces or at the longer time (**Figure 5b**). This kind of load distribution within the structure has already been shown for titin and ubiquitin proteins(34). It is analogous to Buckminster's geodesic dome which distributes the stress within its structure and can withstand a very high load(35). Similarly, proteins can also be considered as pre-stressed (pre-existing tension) molecules due to their local frustration, where the balance between the tensile and compressive forces determines the overall mechanical stability.

To decipher the inter-residue interactions that might absorb the applied force and steer it away from these critical salt-bridges, especially from E78-R113, we calculated the correlation of pairwise inter-residue forces with the applied force ($r_{af}^{f}$) (**Figure 5c)**. The residue pairs with $|r_{af}^{f}|$ significantly greater than zero experience a change in the inter-residue force as a function of applied force. These residue pairs should be responsible for actively distributing the load inside the proteins and the complex. On the other hand, residue pairs with $r_{af}^{f} \approx 0$ bear a consistent load irrespective of the applied force. **Figure 5c** shows $r_{af}^{f}$ for inter-protein residue pairs. We observe that the load balancing is performed by interactions between the EC1-EC1 and EC1-EC2 domains of Cdh23 and Pcdh15 respectively. Using these correlation plots, we can find multiple residue pairs at

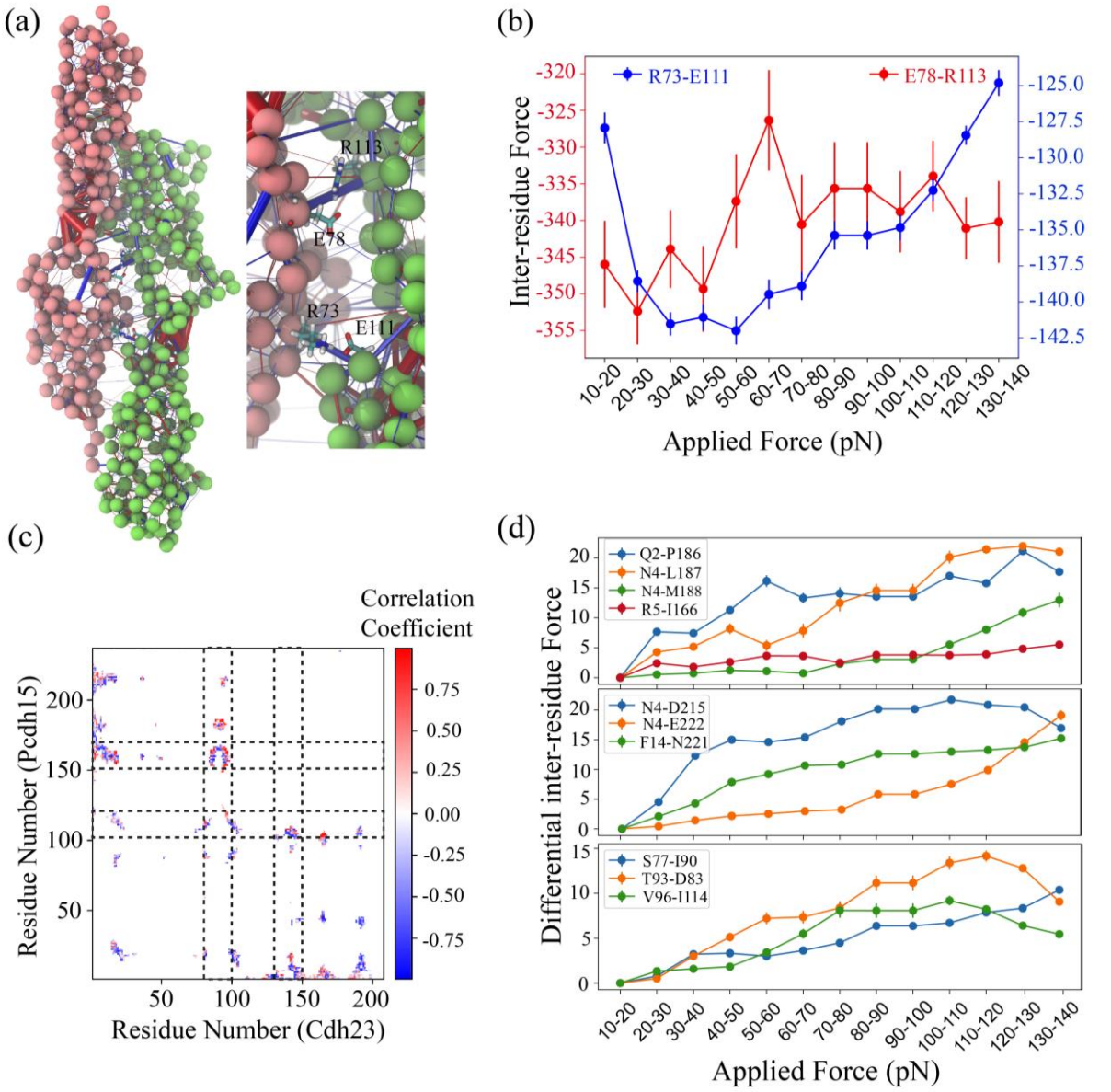


**Figure 5: Load balancing in Cdh23-Pcdh15 complex.** (a) The pairwise inter-residue forces plotted over the structure of the Cdh23-Pcdh15 complex. The color of the cylinders represents the sign of the force with blue being negative and red being positive. The width of the cylinders represents the magnitude of the force. (b) The inter-residue forces for the salt-bridge paired residues E78-R113 and R73-E111. (c) A plot showing the correlation coefficient between the inter-residue forces and the applied force. (d) Some examples of residue pairs for which the inter-residue force is highly correlated with applied force ($r > 0.7$).

various contact areas between the two proteins which absorb the applied force. The differential inter-residue force (inter-residue force at a force range – inter-residue force at

minimum force (10-20 pN) for some of these pairs is plotted in **Figure 5d**. Additionally, the force correlation plots show that the residues in certain regions of the proteins (e.g., residues 150-175 and 100-125 for Pcdh15 and 75-100 and 130-150 for Cdh23) have multiple partners with inter-residue forces strongly correlated with the applied force (black dashed lines, **Figure 5c**). This network of interconnected residue pairs bears and distributes the applied force to maintain the integrity of the complex.

### 2.3.4 The slip-to-catch transition is abolished in an inherited deafness mutation in Pcdh15 (R113G)

In reference to the SMD results, inter-protein salt-bridge E78 (Cdh23)-R113 (Pcdh15) remains intact with a dominant survival throughout the force range. The proteins undergo inter-domain rotations to make new contacts or strengthen existing ones to allow the

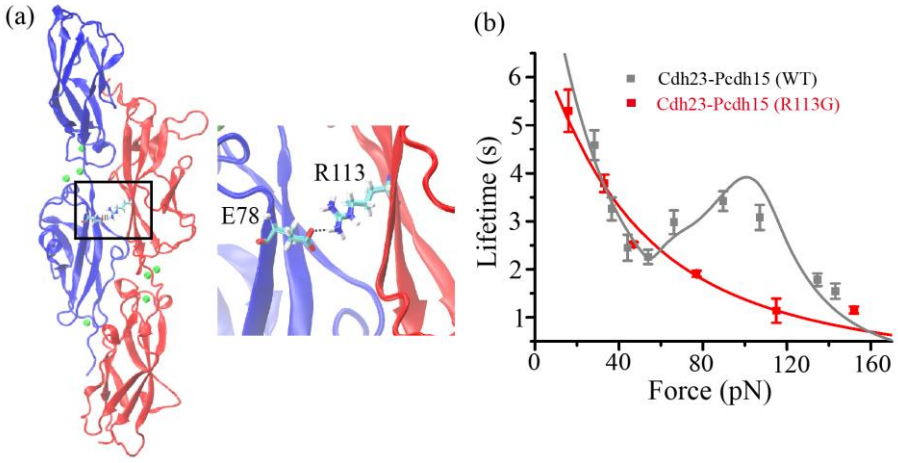


**Figure 6: Mutant tip-links R113G slip with the force.** (a) Cartoon representation of the Crystal structure of tip-link complex highlighting the salt bridge between E78 (Cdh23) and R113 (Pcdh15) at the binding interface. The right panel shows the zoomed view of the salt-bridge interaction. (b) Force-dependent lifetime behavior of mutant tip-links (R113G) showed slip-bond behavior (red) in contrast to the slip-catch-slip observed for WT tip-link complex (grey). The solid red line is the fit from Bell's model.

complex to resist the applied force. From these observations, it is apparent that this robust bridge serves as a molecular pivot/axle which drives the switch from a weaker binding-

interface to a stronger binding-interface of the complex under the tensile force. A transition from a weaker binding interface to a stronger interface is responsible for the catch-bond behavior. The tensile force here acts as a catalyst and exposes the cryptic binding interface by imparting entropic energy for extension and rotation of the interacting partners. Incidentally, the importance of R113 of Pcdh15 is also known in physiology, where the mutation of R113 to glycine (R113G) is found in patients suffering from inherited deafness(36). Accordingly, we recombinantly synthesized Pcdh15 EC1-2 (R113G) and studied the bond-lifetime dynamics of the mutant tip-links Cdh23 EC1-2 (WT)-Pcdh15 EC1-2 (R113G) with force using force-clamp spectroscopy. We found that Pcdh15 R113G fails to steer the slip-to-catch transition and the complex monotonously slips towards dissociation with force **(Figure 6b)**. This implies that the slip-catch-slip bond feature of the wild-type tip-link complex is essential for normal hearing and once the slip-to-catch transition is lost, it cause impaired hearing.

### 2.3.5 A kinetic (force-induced stronger-binding) model to explain slip-catch-slip transitions

Once the molecular details of the slip-to-catch transition are revealed and verified using mutational studies, we aimed to fit our experimental slip-catch-slip data using a mathematical model to estimate the kinetic parameters that govern the slip-to-catch transition and the complex unbinding.

In literature, the kinetic model of catch, slip, and ideal bonds were proposed prior to even experimental findings. A dynamic switch in the mechanical stiffness of the biological bonds under tension was proposed to be responsible for all three types of bonds(13). Subsequently, several phenomenological theories, including a two-pathway model(37), allosteric bond model(38), deformation-model(39), and sliding-rebinding model(32) were derived to explain the catch bonds. From *in-silico* studies, we learned that the force-induced transition to a denser binding interface is responsible for catch. Accordingly, we derived a

'force-induced stronger-binding model' from the 'sliding-rebinding model' and fit our data. This kinetic model best describes the *in-silico* results. We proposed two pathways for dissociation of the complex. One pathway involves the force-induced conformational transition to a stronger binding interface. The other pathway is the direct dissociation of the heteromeric complex. We define a critical force ($F_{C1}$) to tune the probabilities of enhanced-binding or direct dissociation, and a second critical force, $F_{C2}$, to limit the maximum catch regime (Eq 1, Methods). Above $F_{C2}$, bond-lifetime decreases monotonously. The rate of sliding ($k_{+1}$) and rebinding ($k_{+2}$) are considered independent of force whereas the rates of dissociation ($k_{-1}$, $k_{-2}$) in both the pathways are force-dependent**.** We fit the lifetime vs. force data of Cdh23 EC1-2 (WT)-Pcdh15 EC1-2 (WT) by a nonlinear least square curve-fitting algorithm using MATLAB. Our model fits the experimental data convincingly (**Figure 1d and Table 1)**.

**Table 1: Kinetic parameters obtained from the force-induced rebinding fit of lifetime-force data for Cdh23 EC1-2-Pcdh15 EC1-2.**

| | $k_{-1}^{0}$ ($s^{-1}$) | $x_\beta$ (Å) | $k_{+1}$ ($s^{-1}$) | $k_{+2}$ ($s^{-1}$) | $F_{c2}$ (pN) | $n$ |
|---|---|---|---|---|---|---|
| Cdh23 EC1-2-Pcdh15 EC1-2 (WT) | 0.2 | 1.1 | 0.1 | 10 | 116 | 2.1 |
| Cdh23 EC1-2-Pcdh15 EC1-2 (R113G) | 0.3 | 0.8 | - | - | - | - |

Further, we fitted the slip-bond lifetime-force data of mutant complex with Bell's model and obtained the intrinsic off-rate, $k_{-1}^{0}$ and distance to transition state $x_\beta$. Interestingly, $k_{-1}^{0}$ (0.3 $s^{-1}$) and $x_\beta$ (0.8 Å) of mutant tip-links are comparable to that of WT tip-links data (0.2

$s^{-1}$ & 1.1 Å, respectively) (Table 1). However, the bond-survival for mutant drops rapidly with force while WT tip-links survive high-intensity stimuli by switching to a stable conformation under tension.

## 2.4 Discussion

Direct measure of force-lifetime of tip-links using single-molecule force-clamp experiments revealed a counterintuitive slip-catch-slip bond. We deciphered the molecular mechanism of catch-bond formation from *in silico* simulations using FISST. We observed a change in the inter-domain angles for both the proteins accompanied with an increase in buried surface area with the application of force. An increase in the buried surface area is directly correlated to the binding affinity. This indicates that the strength of the tip-link complex increases with force which also corroborates with experimental catch-bond observation where lifetime increases with tensile force. Further, we found that some new salt bridges are formed with the application of force while some others get strengthened. We noticed that survival of salt bridge E78-R113 at the interface does not vary with force and further, the inter-residue force of this interaction almost becomes constant after 40 pN. This indicates that while the external force applied to the complex increases, the force experienced by this bond stays constant. In physiology, R113G mutation causes inherited deafness in humans emphasizing the importance of this interaction in maintaining the integrity of the complex. The analysis of inter-residue forces and their correlation with applied force reveals a dynamic load balancing system in the complex which absorbs the applied force and distributes it away from this crucial interaction. Further, in the AFM experiment with the R113G mutant, slip-to-catch transition is abolished and mutant tip-link exhibits an exclusive slip bond with force. From the mutational study, we verify that this salt bridge serves as a molecular pivot and is responsible for the switch to a stronger binding interface. A previous single-molecule force-ramp study using optical tweezers also reported the drop in lifetime for this mutation in full-length dimeric tip-link(5).

In the past two decades, catch bond has been identified in numerous biological complexes, such as FimH with its ligand mannose(11), VWF binding to platelet glycoprotein(10), P, L, and E-selectins and their leukocyte glycoprotein ligand PSGL-1(8, 40–42), integrins(43), actin-myosin complex(44), classical cadherins(12), cadherin-catenin-actin complex(45), etc. In all these complexes, the catch bond resists counterforce by strengthening the complex and utilizes mechanical perturbations as cues. In the same line, for non-classical tip-links' cadherins, catch bond was speculated from SMD(46), but never experimentally observed. Rather, force-ramp experiments using optical tweezers on tip-link reported a slip-only behavior up to a maximum applied force of 60 pN(5). These measurements were limited to relatively lower loading rates varying from 0.39 pN/s to 95.6 pN/s. We performed experiments at comparatively higher loading rates of 60,000 pN/s which is more physiologically relevant since, at a resting tension of 5 pN at 1kHz frequency, theoretical force loading is ~5000 pN/s(47). At higher forces and large frequency range of hearing, the force-loading rates would be even more. Interestingly, squeezing of the tip-links' dimer complexes with increasing force was considered responsible for catch bonds in SMD(46). However, we found that the slip-to-catch transition is the phenomenon of the single tip-link interface itself. Further, using the force-induced enhanced-binding model, we fitted the experimental data and obtained the kinetic parameters. Overall, we conclude that the slip-to-catch transition which drives the tip-link complex to a more stable state prolongs the tip-links' survival at higher forces from loud sound.

**Bibliography**

1. M. Schwander, B. Kachar, U. Müller, The cell biology of hearing. *J. Cell Biol.* **190**, 9–20 (2010).

2. A. J. Hudspeth, Hair-bundle mechanics and a model for mechanoelectrical

transduction by hair cells. *Soc. Gen. Physiol. Ser.*, 357–370 (1992).

3. M. Sotomayor, W. Weihofen, R. Gaudet, D. P. Corey, Structure of a Force-Conveying Cadherin Bond Essential for Inner-Ear Mechanotransduction. *Nature* **492**, 128–132 (2012).

4. J. P. Hazra, *et al.*, Broken force dispersal network in tip-links by the mutations induces hearing-loss. *Biochem. J.* **476**, 2411–2425 (2019).

5. E. M. Mulhall, *et al.*, Single-molecule force spectroscopy reveals the dynamic strength of the hair-cell tip-link connection. *Nat. Commun.* **12**, 1–15 (2021).

6. A. A. Indzhykulian, *et al.*, Molecular Remodeling of Tip Links Underlies Mechanosensory Regeneration in Auditory Hair Cells. *PLoS Biol.* **11**, 1–15 (2013).

7. G. Binnig, C. F. Quate, C. Gerber, Atomic force microscope. *Phys. Rev. Lett.* **56**, 1–5 (1986).

8. B. T. Marshall, *et al.*, Direct observation of catch bonds involving cell-adhesion molecules. *Nature* **423**, 190–193 (2003).

9. K. Manibog, C. F. Yen, S. Sivasankar, "Measuring Force-Induced Dissociation Kinetics of Protein Complexes Using Single-Molecule Atomic Force Microscopy" in *Methods in Enzymology* **582**, 297-320 (2017).

10. T. Yago, *et al.*, Platelet glycoprotein Ibα forms catch bonds with human WT vWF but not with type 2B von Willebrand disease vWF. *J. Clin. Invest.* **118**, 3195–3207 (2008).

11. O. Yakovenko, *et al.*, FimH forms catch bonds that are enhanced by mechanical force due to allosteric regulation. *J. Biol. Chem.* **283**, 11596–11605 (2008).

12. S. Rakshit, Y. Zhang, K. Manibog, O. Shafraz, S. Sivasankar, Ideal, catch, and slip bonds in cadherin adhesion. *Proc. Natl. Acad. Sci. U. S. A.* **109**, 18815–18820 (2012).

13. M. Dembo, D. C. Torney, K. Saxman, D. Hammer, The reaction-limited kinetics of membrane-to-surface adhesion and detachment. *Proc. R. Soc. B Biol. Sci.*, 55–83 (1988).

14. S. Srinivasan, J. P. Hazra, G. S. Singaraju, D. Deb, S. Rakshit, ESCORTing proteins directly from whole cell-lysate for single-molecule studies. *Anal. Biochem.* **535**, 35–42 (2017).

15. P. E. Marszalek, H. Li, A. F. Oberhauser, J. M. Fernandez, Chair-boat transitions in single polysaccharide molecules observed with force-ramp AFM. *Proc. Natl. Acad. Sci. U. S. A.* **99**, 4278–4283 (2002).

16. A. F. Oberhauser, P. K. Hansma, M. Carrion-Vazquez, J. M. Fernandez, Stepwise unfolding of titin under force-clamp atomic force microscopy. *Proc. Natl. Acad. Sci. U. S. A.* **98**, 468–472 (2001).

17. I. Popa, P. Kosuri, J. Alegre-Cebollada, S. Garcia-Manyes, J. M. Fernandez, Force dependency of biochemical reactions measured by single-molecule force-clamp spectroscopy. *Nat. Protoc.* **8**, 1261–1276 (2013).

18. J. L. Hutter, J. Bechhoefer, Calibration of atomic-force microscope tips. *Rev. Sci. Instrum.* **64**, 1868–1873 (1993).

19. S. Jo, T. Kim, V. G. Iyer, W. Im, CHARMM-GUI: A web-based graphical user interface for CHARMM. *J. Comput. Chem.* **29**, 1–7 (2008).

20. J. Lee, *et al.*, CHARMM-GUI Input Generator for NAMD, GROMACS, AMBER, OpenMM, and CHARMM/OpenMM Simulations Using the CHARMM36 Additive Force Field. *J. Chem. Theory Comput.* **12**, 405–413 (2016).

21. J. Huang, *et al.*, CHARMM36: An Improved Force Field for Folded and Intrinsically Disordered Proteins. *Nature Methods* **14**, 71-73 (2017).

22. W. L. Jorgensen, Quantum and statistical mechanical studies of liquids. 10.

Transferable intermolecular potential functions for water, alcohols, and ethers. Application to liquid water. *J. Am. Chem. Soc.* **103**, 335–340 (1981).

23. M. J. Abraham, *et al.*, Gromacs: High performance molecular simulations through multi-level parallelism from laptops to supercomputers. *SoftwareX* **1**–**2**, 19–25 (2015).

24. M. Bonomi, *et al.*, PLUMED: A portable plugin for free-energy calculations with molecular dynamics. *Comput. Phys. Commun.* **180**, 1961–1972 (2009).

25. G. A. Tribello, M. Bonomi, D. Branduardi, C. Camilloni, G. Bussi, PLUMED 2: New feathers for an old bird. *Comput. Phys. Commun.* **185**, 604–613 (2014).

26. B. Hess, H. Bekker, H. J. C. Berendsen, J. G. E. M. Fraaije, LINCS: A Linear Constraint Solver for molecular simulations. *J. Comput. Chem.* **18**, 1463–1472 (1997).

27. T. Darden, D. York, L. Pedersen, Particle mesh Ewald: An N·log(N) method for Ewald sums in large systems. *J. Chem. Phys.* **98**, 1–5 (1993).

28. M. J. Hartmann, Y. Singh, E. Vanden-Eijnden, G. M. Hocky, Infinite switch simulated tempering in force (FISST). *J. Chem. Phys.* **152**, 1–10 (2020).

29. N. Michaud-Agrawal, E. J. Denning, T. B. Woolf, O. Beckstein, MDAnalysis: A toolkit for the analysis of molecular dynamics simulations. *J. Comput. Chem.* **32**, 1–9 (2011).

30. M. Tiberti, *et al.*, PyInteraph: A framework for the analysis of interaction networks in structural ensembles of proteins. *J. Chem. Inf. Model.* **54**, 1537–1551 (2014).

31. B. I. Costescu, F. Gräter, Time-resolved force distribution analysis. *BMC Biophys.* **6**, 1–5 (2013).

32. J. Lou, C. Zhu, A structure-based sliding-rebinding mechanism for catch bonds.

*Biophys. J.* **92**, 1471–1485 (2007).

33. G. I. Bell, Models for the Specific Adhesion of Cells to Cells. *Science.* **200**, 618–627 (1978).

34. S. A. Edwards, J. Wagner, F. Gräter, Dynamic prestress in a globular protein. *PLoS Comput. Biol.* **8**, 1–11 (2012).

35. D. E. Ingber, The origin of cellular life. *BioEssays*, 1160–1170 (2000).

36. Z. M. Ahmed, *et al.*, Gene structure and mutant alleles of PCDH15: nonsyndromic deafness DFNB23 and type 1 Usher syndrome. *Hum. Genet.* **124**, 215–223 (2008).

37. Y. V. Pereverzev, O. V. Prezhdo, M. Forero, E. V. Sokurenko, W. E. Thomas, The two-pathway model for the catch-slip transition in biological adhesion. *Biophys. J.* **89**, 1446–1454 (2005).

38. W. Thomas, *et al.*, Catch-bond model derived from allostery explains force-activated bacterial adhesion. *Biophys. J.* **90**, 753–764 (2006).

39. A. Nair, S. Chandel, M. K. Mitra, S. Muhuri, A. Chaudhuri, Effect of catch bonding on transport of cellular cargo by dynein motors. *Phys. Rev. E* **94**, 1–5 (2016).

40. K. K. Sarangapani, *et al.*, Low Force Decelerates L-selectin Dissociation from P-selectin Glycoprotein Ligand-1 and Endoglycan. *J. Biol. Chem.* **279**, 2291–2298 (2004).

41. T. Yago, *et al.*, Catch bonds govern adhesion through L-selectin at threshold shear. *J. Cell Biol.* **166**, 913–923 (2004).

42. A. M. Wayman, W. Chen, R. P. McEver, C. Zhu, Triphasic force dependence of E-selectin/ligand dissociation governs cell rolling under flow. *Biophys. J.* **99**, 1166–1174 (2010).

43. F. Kong, A. J. García, A. P. Mould, M. J. Humphries, C. Zhu, Demonstration of

catch bonds between an integrin and its ligand. *J. Cell Biol.* **185**, 1275–1284 (2009).

44. B. Guo, W. H. Guilford, Mechanics of actomyosin bonds in different nucleotide states are tuned to muscle contraction. *Proc. Natl. Acad. Sci. U. S. A.* **103**, 9844–9849 (2006).

45. C. D. Buckley, *et al.*, The minimal cadherin-catenin complex binds to actin filaments under force. *Science.* **346**, 1–8 (2014).

46. D. Choudhary, *et al.*, Structural determinants of protocadherin-15 mechanics and function in hearing and balance perception. *Proc. Natl. Acad. Sci. U. S. A.* **117** 24837–24848 (2020).

47. T. F. Bartsch, F. E. Hengel, A. Oswald, G. Dionne, I. V Chipendo, The elasticity of individual protocadherin 15 molecules implicates cadherins as the gating springs for hearing. *Proc. Natl. Acad. Sci.* **116**, 11048–11056 (2018).

# Chapter 3

## Non-interacting domains of Cdh23 aid in the force-dissemination

## 3.1 Introduction

In the previous chapter, we deciphered that the tip-links' binding interface undergoes a slip-catch-slip bond transition under tension. Further, *in-silico* studies revealed the molecular mechanism of slip-to-catch binding conformation of the complex. Interestingly, Cdh23 and Pcdh15 are very long proteins with 27 and 11 EC domains, respectively. However, only two N-terminal domains interact to mediate the heterophilic interaction(1). The rest of the non-interacting domains may interact laterally to facilitate the formation of cis-homodimer(2, 3). In addition, these spare domains also modulate the elasticity of the tip-links. Tip-links as gating springs must possess an elastic module(4, 5). The elastic behavior of individual tip-link proteins is previously reported by observing force-induced unfolding dynamics using single-molecule and in-silico tools(6–9). However, the effect of protein elasticity and contribution of force-induced alterations on tip-links lifetime dynamics is not yet deciphered. We aimed to understand how the slip-catch-slip bond nature of the tip-link varies when we introduce the other non-interacting domains which will manifest the overall elasticity of the tip-links. To achieve this objective, we designed different fragments of Cdh23 with varying domain lengths to systematically incorporate the elasticity factor into the tip-link complex. We synthesized Cdh23 EC1-5, Cdh23 EC1-10, Cdh23 EC1-21, and Cdh23 EC1-27 with entire 27 domains. These deletion mutants of Cdh23 were selected on the basis of structural variation among the different domains. The solved crystal structure of the first three domains, EC1-3, didn't show any significant structural deviation. Further, few unusual loops have been observed in the solved crystal structure of EC6-8(3). These unusual or non-canonical features increases as we go further towards the higher domain numbers. Selected truncated variants of Cdh23 accommodate these deviations sequentially in increasing order. To delineate the effect of such canonical and non-canonical loops and connecting domains on force-response of tip-links, we studied the mechanoresponsive behavior of all the tip-link complexes of different lengths at the single-molecule level using force-clamp spectroscopy.

## 3.2 Experimental Section

### 3.2.1 Cloning of domain deletion mutants of Cdh23

Cadherin 23 with 27 EC domains, one transmembrane, and one cytosolic domain was a generous gift from Dr. Raj Ladher, NCBS, Bangalore. To perform single-molecule force-spectroscopy experiments we only required the EC domain region. Therefore, we cloned Cdh23 EC1-27 (with only the extracellular part) in pcDNA 3.1 (+) between the restriction sites NheI and XhoI. Since Cdh23 with the entire 27 domains is a very large construct with ~10k base pairs, so we ligated the two fragments of Cdh23 having overlapping regions using Gibson assembly(10).

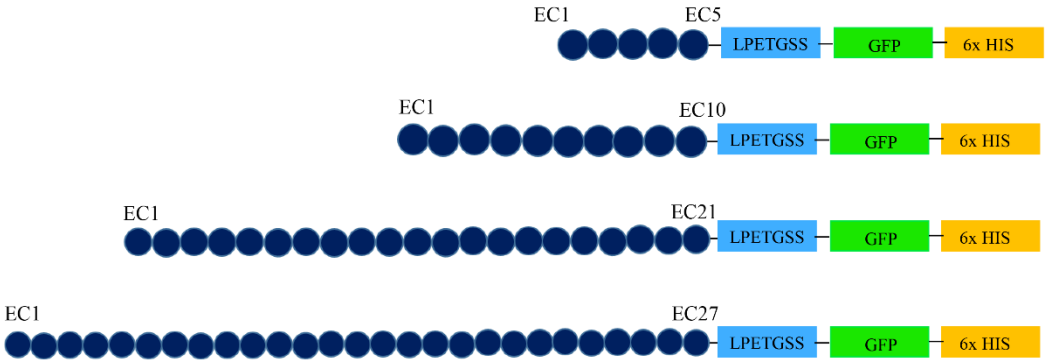


**Figure 1: Schematic of the different truncated variants of Cdh23.** All the truncated variants of Cdh23 with 5, 10, and 21 domains were generated from the original construct Cdh23 EC1-27 using primers specific to the desired domain. In all the constructs, C-terminus has LPETGSS (sort-tag), GFP, and 6x His.

From the Cdh23 EC1-27, we generated all the domain deletion mutants; EC1-5, EC1-10, and EC1-21 using DNA the recombination method*. All the constructs have sort-tag (LPETGG), GFP, and 6xHis-tag at the C-terminus **(Figure 1**). Sort-tag was inserted for covalent attachment of the protein to the surface for single-molecule experiments, GFP tag helped in tracking the protein expression after transfection and His-tag was necessary for protein purification. All the constructs have signal peptide at the N-terminus to guide the

** Cloning of full-length Cdh23 EC1-27 has been done by Dr. Amin and Anuj Kumar. Truncated variants of Cdh23 have been cloned by Sayan Das and Gaurav Kumar Bhati.*

expressed protein in the media. Cloning of all the constructs was verified using double-digestion, PCR amplification, and DNA-sequencing.

### 3.2.2 Expression and purification of all the constructs

For protein expression, we have used Expi-CHO suspension cells (#A29133, Thermo Fisher Scientific). This system is modified to optimize the expression of mammalian proteins in large amounts. For transfection, we followed the prescribed protocol. Cells were transfected at the cell density of $10^7$ with the 1µg/mL DNA plasmid. During the transfection, plasmid DNA and Expifectamine reagent were diluted in OPTIPRO Serum-Free Media (SFM) followed by the drop-wise addition of their mixture to the culture media with ExpiCHO cells while mixing continuously. 20 h post-transfection, the culture media was supplemented with additional reagents like feed and enhancer to maintain the viability of the cells and to enhance the protein expression. The cells were then incubated for 7-10 days depending on their viability and optimum protein expression at 37 °C, 125 rpm, and 6% $CO_2$. Cells were monitored regularly during this incubation period to check their viability. The media was collected afterward by pelleting down the cells at 2000 rpm for 15 min at RT. The collected media was then dialyzed against dialysis buffer (25 mM HEPES, 150 mM NaCl, 50 mM KCl and 5 mM $CaCl_2$) for 32 hours and intermittently changing the buffer every 8 h. The dialyzed media with proteins were purified using Ni-NTA-based affinity chromatography. After the steps of equilibration, protein-loading, and washing with 25 mM imidazole; proteins were eluted with 100 mM, 250 mM imidazole, and 500 mM imidazole dialysis buffer. The purity of the samples was checked using SDS-PAGE at various acrylamide percentages depending on the molecular weight of proteins.

### 3.2.3 Single-molecule force spectroscopy experiments with AFM

To perform single-molecule experiments, we first cleaned the glass coverslips with plasma cleaner and piranha solution as described before in section 2.2.2 in chapter 2. Further, silanization of the coverslips and cantilever with APTES was followed by the PEGylation.

However, this time, instead of using PEG of Molecular weight 5kDa, we used PEG2 (with 2 units of PEG) for both mono and bi-functional PEG.

After surface functionalization, we covalently anchored the C-terminus of different Cdh23 variants on the coverslip using sortagging chemistry for each of the experiment(11) and Pcdh15 EC1-2 on the cantilever to mediate the heterophilic interaction. Subsequently, we performed force-clamp spectroscopy as described previously in section 2.2.3 in chapter 2. All the experiments were performed in the buffer with 25 mM HEPES, 100 mM NaCl, 50 mM KCl and 50 µM $CaCl_2$. Data analysis including lifetime measurements and step heights estimation carried out by using home-written MATLAB programs.

### 3.2.4 Kinetic model fitting of force-lifetime data for different tip-link complexes using Force-induced stronger-binding Model

To fit the force-lifetime relationship for different length variants of tip-links, we used the similar force-induced stronger-binding model (chapter 2, section 2.2.5) by including the additional parameters for unfolding probability. To incorporate the unfolding dynamics in the kinetic model, we calculated the force-dependent unfolding probabilities for the most predominant unfolding step heights (~5 and ~12 nm) by using the following equations(12, 13)

$$P_{1u} = 1 - \exp(-k_{1u}t)$$

$$P_{2u} = 1 - \exp(-k_{2u}t) \quad (1)$$

Where $P_{1u}$ and $P_{2u}$ are the unfolding probabilities of 5 nm and 12 nm step height respectively. $k_{1u}$ and $k_{2u}$ are their corresponding force-dependent unfolding rates which are estimated from the Bell equation(14)

$$k_{1u} = k_{1u}^{0} \times \exp(f.x_{1u}/k_B T)$$

$$k_{2u} = k_{2u}^{0} \times \exp(f.x_{2u}/k_B T) \quad (2)$$

Zero-force unfolding rate ($k_u^0$) and distance to transition-state ($x_u$) for individual step height of 5 and 12 nm were obtained by exponential fitting of their force-lifetime data.

Next, we determined the unfolding probabilities $P_{1u}$ and $P_{2u}$ at each force using equations 1 and 2. Total unfolding probability ($P_U$) will be the addition of $P_{1u}$ and $P_{2u}$ as both types of unfoldings can occur simultaneously and thus, given as:

$$P_U = (n_{1N} \times P_{1u} + n_{2N} \times P_{2u}),$$

here, $n_{1N} = n_1/(n_1 + n_2)$

$$n_{2N} = n_2/(n_1 + n_2)$$

$n_1$, $n_2$ are the force-dependent number of unfoldings for 5 nm and 12 nm respectively, observed from the experimental data for all the tip-link variants.

Total unfolding-unbinding probability $(P_{00u})$ can be given as the multiplication of total unfolding probability ($P_U$) and the dissociation probability ($P_{00}$)

$$P_{00u} = P_U \times P_{00}$$

Finally, the survival probability was determined as before, $1 - P_{00u}$.

## 3.3 Results

### 3.3.1 Slip-catch-slip behavior is inherent for all domain length variants of the tip-links

In order to decipher the bond-lifetime dynamics of tip-links coupled with the molecular elasticity of the long proteins, we systematically incorporated the non-interacting domains in Cdh23 to increase the protein elasticity. We designed and expressed four different variants of Cdh23, Cdh23 EC1-5, Cdh23 EC1-10, Cdh23 EC1-21, and full-length Cdh23

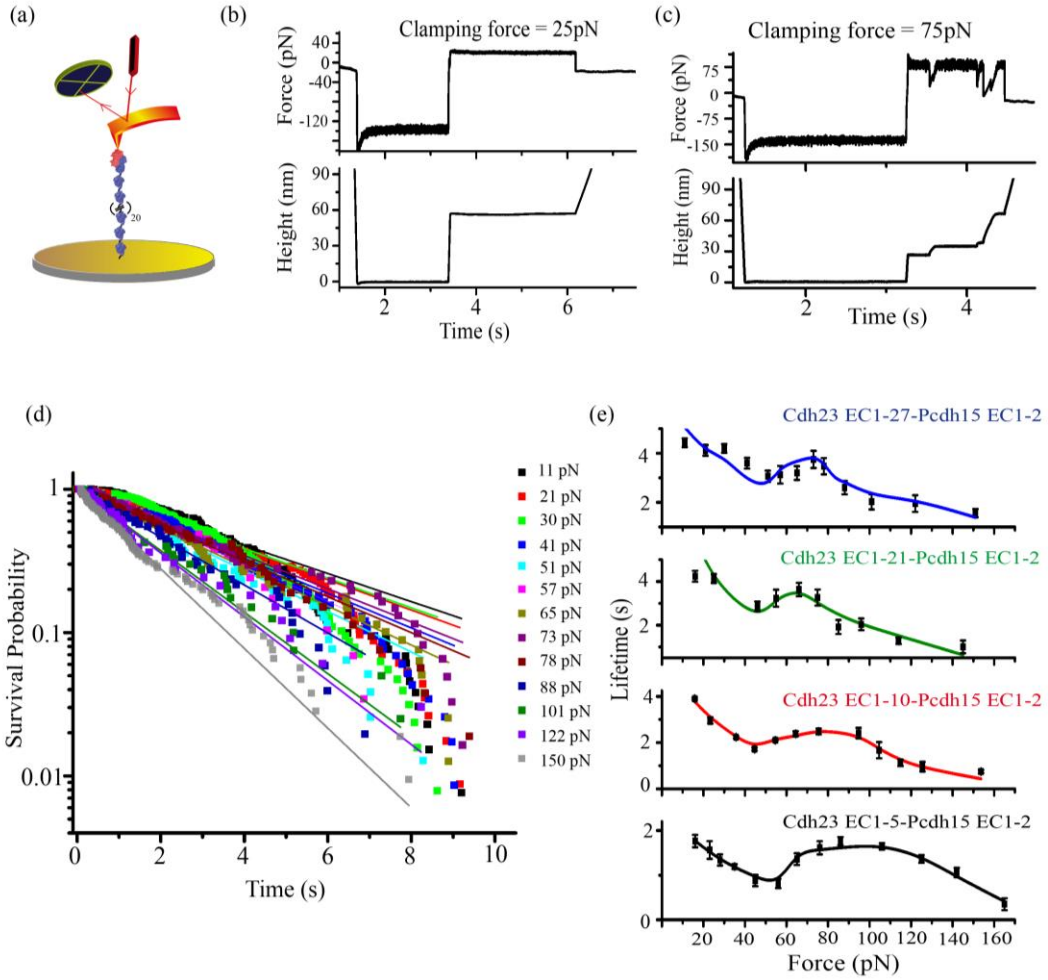


**Figure 2: Slip-catch-slip feature is conserved for the tip-links of varying lengths.** (a) Schematic representation of AFM-based force-clamp experiment for Cdh23 EC1-27-Pcdh15 EC1-2 complex. We performed the force-clamp measurements with Cdh23 constructs of varying domain numbers (n) of 5, 10, 21, and 27. (b and c) Representative force vs. time and height vs. time plot for clamp measurements of Cdh23 EC1-27-Pcdh15 EC1-2 interaction complex. In the measurement using full-length Cdh23 and other truncated variants, we observe instantaneous dropping of force followed by restoration to clamping force which is also reflected in the corresponding length vs. time plot as instantaneous height change. Due to the feedback control loop, the cantilever maintains the constant clamping force after each unfolding by re-adjusting the piezo position. (d) Survival probability plot for Cdh23 EC1-27-Pcdh15 EC1-2 complex. Data best fitted to mono-exponential decay and provide the average lifetime of the bond at all the clamping forces. (e) The lifetime-force behavior for tip-link complexes for different lengths of Cdh23 constructs. All the complexes have shown slip-catch-slip transition for force-mediated lifetime evolution.

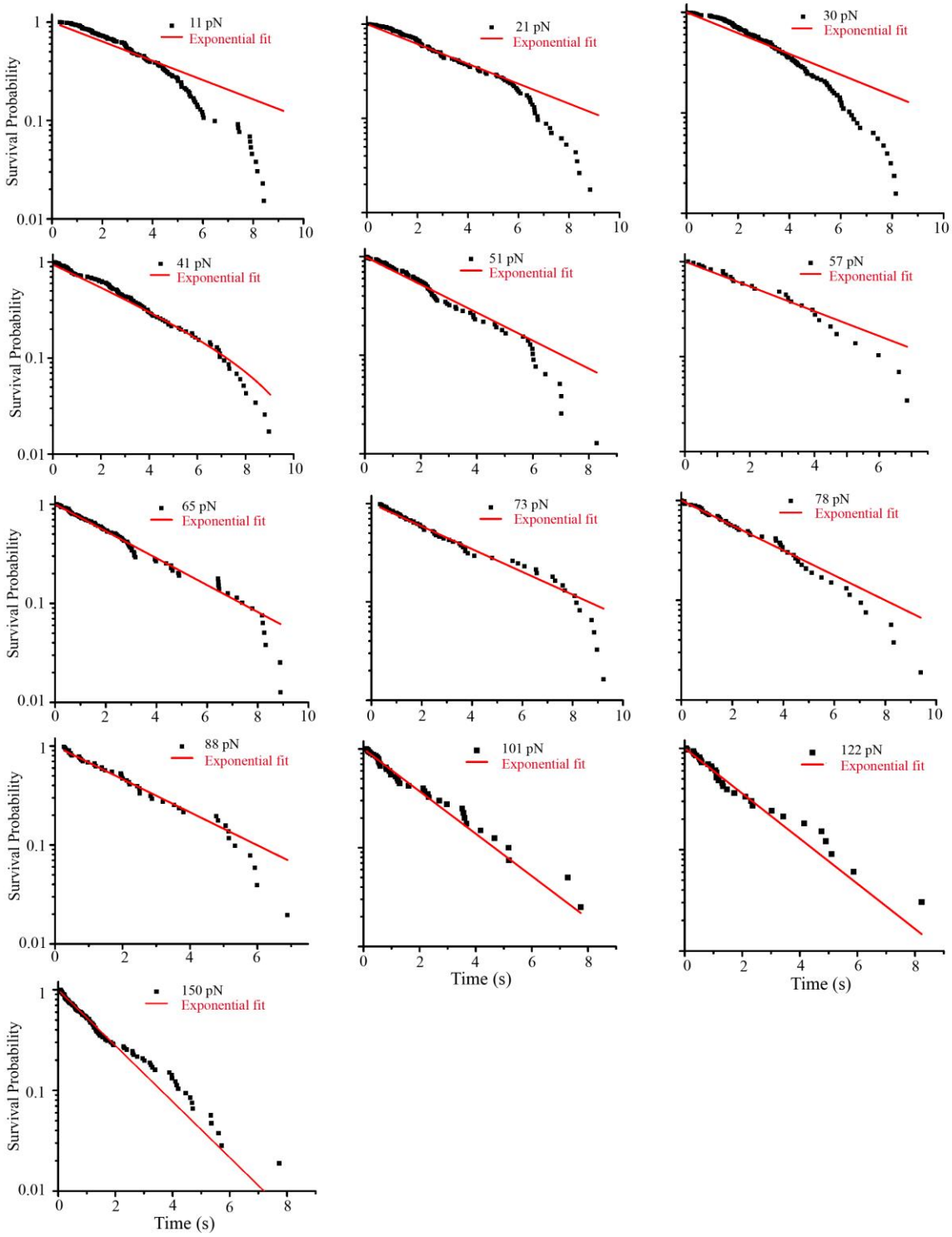


**Figure 3: Exponential decay fitting of survival plot for Cdh23 EC1-27-Pcdh15 EC1-2 at different clamping forces.** For Cdh23 EC1-27-Pcdh15 EC1-2, mono-exponential decay fitting of the survival plot is shown separately at each clamping force for the sake of clarity. Overlaid graph is shown in Figure 2 (d).

EC1-27. To perform the force-clamp experiments, we covalently attached Cdh23-variants independently on the coverslip and used the two outermost domains of Pcdh15 EC1-2 on the cantilever as a pulling handle **(Figure 2a**). We recorded the force-clamp data at various clamping forces while scanning through multiple points on the surface. After the experiment, while analyzing the obtained force-clamp data, we noticed two different types of force curves. One with the direct unbinding in which the constant force is maintained throughout the clamping time **(Figure 2b)** and the other where we observed a drop in the force followed by its restoration as depicted in the force vs time graph. We also observed a corresponding increase in the distance between the cantilever and surface as shown in the height vs time plot resembling a staircase-like pattern **(Figure 2c).** Thi**s** relaxation in force and the gain in length indicates that the protein is undergoing extension during the clamping time. Thus, in the tip-links with the non-interacting domains, unfolding is associated with unbinding. Next, we estimated the survival time for each unbinding and generated the survival plots. Subsequently, from the exponential decay fitting of the survival plots **(Figure 2d and Figure 3)**, we extracted the bond lifetime at each clamping force for all the variants of tip-links. Interestingly, the slip-catch-slip feature remains unaltered for all the complex-variants **(Figure 2e),** indicating the bond behavior as the trademark for tip-links. However, the overall lifetime increases systematically with increasing the number of domains. Also, the critical force ($F_{C2}$), at which lifetime is maximum in the catch regime, is shifted towards lower forces with increasing EC domains from Cdh23 EC1-5 to Cdh23 EC1-27.

### 3.3.2 Unfolding mediated unbinding controls the force-dissemination process in tip links

From the force-clamp experiments, we observed unfolding features prior to the unbinding of the tip-link complex. Such entropic and enthalpic elongation of domains of individual tip-link proteins under mechanical tension are reported previously in force-ramp studies(9, 15). However, their contribution to the tip-links' complex lifetime is not known. To delineate the effect of unfoldings on the tip-links bond lifetime, we segregated the force

curves for Cdh23 EC1-27 that do not feature any unfolding and estimated their bond lifetime with force. We found that the force-lifetime trend exhibits similar slip-catch-slip bond behavior, however, the overall lifetime of the tip-link is dropped compared to when unfolding associated events were also considered **(Figure 4a)**. This indicates that unfolding indeed elevates the tip-link bond lifetime. Further, we noticed a surge in the percentage of unfolding associated unbinding events with increasing EC domains **(Figure 4b)**, possibly due to a manifold increase in the force-propagation path. A longer propagation path provides more spatial freedom to the transmission of force prior to the dissociation of the tip-link complex, thus making it more resistant to tensile force.

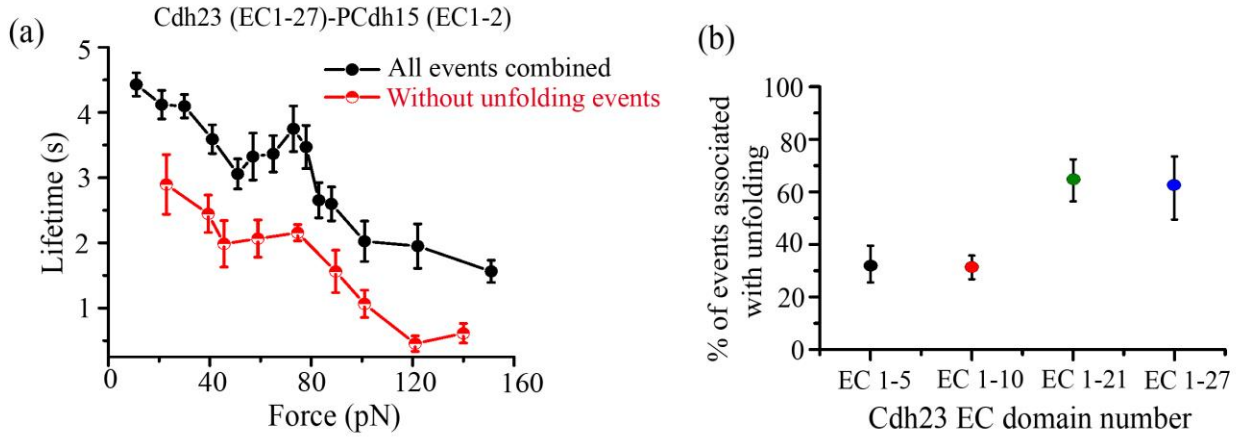


**Figure 4: Unfolding prior to unbinding prolongs the bond lifetime.** (a) Lifetime-force graph depicts that events without undergoing any unfolding registered a lower overall lifetime (red) compared to the events which showed unfolding before unbinding (black). (b) % of force-clamp events undergoing unfolding before unbinding increases with increasing domain numbers.

For quantitative analysis, we estimated all the step height gains in the height vs time graph and generated a histogram for all the domain variants. Histograms of the extensions featured four major distributions with peak maxima at ~5 nm, ~12 nm, ~22 nm, and ~ 34 nm, irrespective of the complex variant (**Table 1, Figure 5a**). Interestingly, the probabilities of the respective length gains varied across the complex variants. We noted

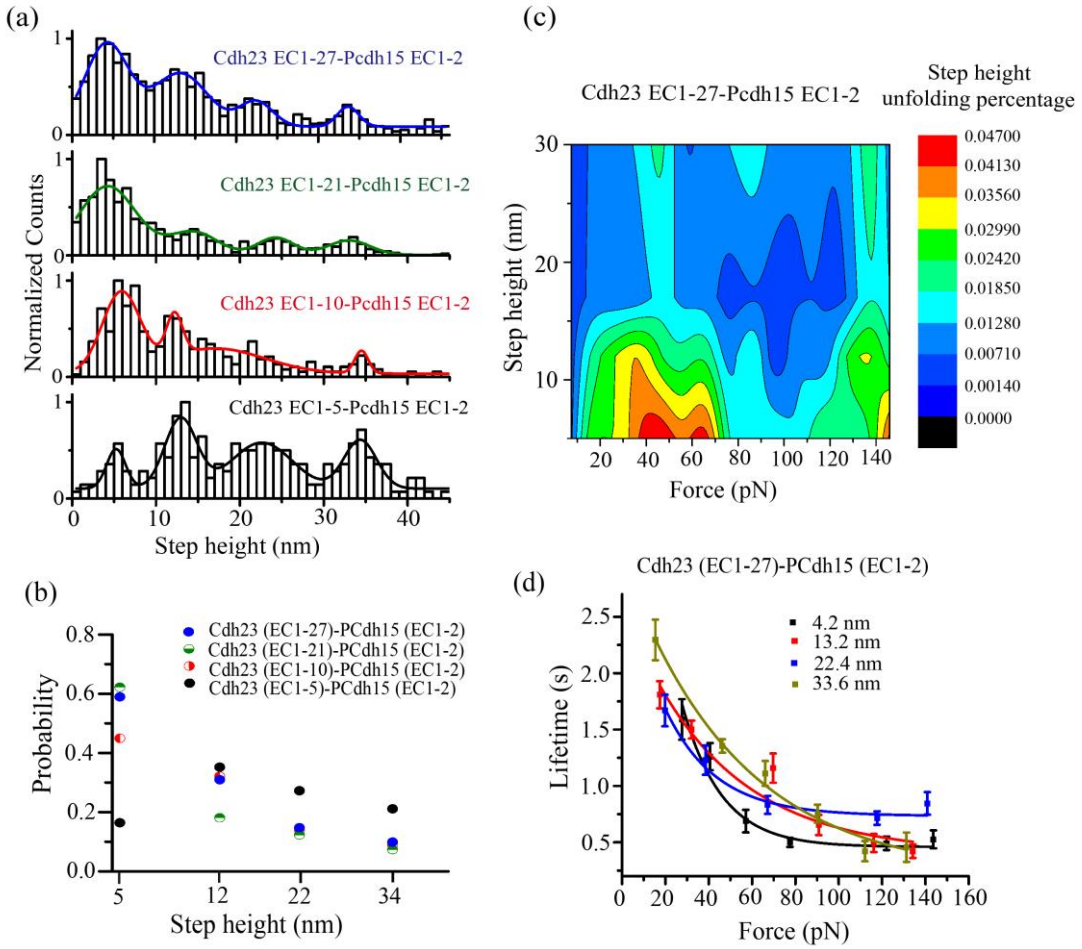


**Figure 5: Quantification of the elongations of tip-links cadherins under tension.** (a) Unfolding step-height distributions calculated from the force curves for all Cdh23 variants, Cdh23 EC1-5 (black), Cdh23 EC1-10 (red), Cdh23 EC1-21 (green), and Cdh23 EC1-27 (blue). Gaussian fits to the step-height distribution fitted the four most probable step-height at ~5 nm, ~12 nm, ~22 nm, and ~34 nm for the tip-link variants. (b) Relative probabilities for each type of the step-height change for all the truncated tip-links with varying lengths of the Cdh23. This analysis reflects the inter-relation between the probabilities for each length gain for all the constructs. (c) Contour plot depicting the unfolding probability of each step-height with the force for Cdh23 EC1-27-Pcdh15 EC1-2 complex. Smaller extensions of ~5 nm and ~12 nm have more propensity to unfold compared to ~22 and ~34 nm extensions. (d) Force-dependent lifetime behavior for all four major step-heights for Cdh23 EC1-27-Pcdh15 EC1-2 tip-link complex is fitted to Bell's model to obtain the kinetic parameters like unfolding rate at zero force ($k_u^0$) and distance to transition state ($x_\beta$).

that the probability of the ~5 nm extension (first peak) increases with increasing the EC domain numbers, from ~0.2 for Cdh23 EC1-5 to ~0.6 for full-length Cdh23 EC1-27 tip-link complex (**Figure 5b**). Generally, one residue contributes ~0.38 nm to the extension of a protein. Accordingly, length gain of ~5 nm originates from the unfolding of 13 residues that might be coming from the extension of the inter-domain linkers. With the increase in the number of EC domains, the extent of non-canonical linkers also increases, which in turn increases the probability of occurrence of ~5 nm extension. Further, an extension of ~34 nm corresponds to the contour length of one EC domain comprising ~110 residues on average. The other two extensions, ~12 nm, and ~22 nm might correspond to the partial unfolding of domains along with linker extension.

**Table 1: Most probable step heights from peak maxima of the unfolding step height distributions for different tip-link complexes.**

| | **Step height 1 (nm)** | **Step height 2 (nm)** | **Step height 3 (nm)** | **Step height 4 (nm)** |
|---|---|---|---|---|
| Cdh23 EC1-5 | 5.2±0.3 | 12.9±0.3 | 22.6±0.5 | 34.3±0.3 |
| Cdh23 EC1-10 | 5.8±0.3 | 12.2±0.2 | 17.1±2.9 | 34.4±0.9 |
| Cdh23 EC1-21 | 4.3±0.2 | 14.6±0.4 | 24.4±0.5 | 33.6±0.6 |
| Cdh23 EC1-27 | 4.2±0.2 | 13.2±0.4 | 22.4±0.4 | 33.6±0.4 |

The unfolding of ~34 nm dumps the maximum enthalpic energy and undoubtedly, cannot be the natural selection for force-dissipation. We, too, noted that the extent of domain unfolding decreases rapidly with increasing domains **(Figure 5b)**. The switch in the propensity of relatively shorter extensions with the number of EC domains is comparable to the ‘gear-shift’ mechanism. Gear-shift mechanism modulates the conformational alterations in the tip-link proteins and aids in the process of smooth force-dissemination. Further, we observed a similar trend in the unfolding propensity of individual step height

with force for Cdh23 EC1-27-Pcdh EC-1-2 complex. We observed a high unfolding propensity for 5 nm and 12 nm at all the forces **(Figure 5c)**. In contrast, 22 nm and 32 nm showed unfolding at mostly intermediate and high force ranges.

### 3.3.3 Kinetic model fitting of slip-catch-slip data by incorporating unfolding dynamics

Further, for Cdh23 EC1-27, we monitored the force-induced lifetime behavior of each extension individually **(Figure 5d)**. Towards this, we estimated the unfolding lifetime for each of the step heights and separately monitored their lifetime dynamics with force. In contrast to the slip-catch-slip features of tip-links, unfolding lifetimes of all extensions exhibit slip-only behavior with force. We fitted the data with Bell's model and obtained the zero-force unfolding rate ($k_u^0$) and distance to the transition state, $x_\beta$ **(Table 2).** Notably, the $x_\beta$, 2.3±0.4 Å, is highest for ~5 nm extension, indicating the linker-unfolding is most susceptible to force, as expected.

**Table 2: Kinetic parameters obtained from Bell's-model fitting of force-dependent lifetime data of individual step height in Cdh23 EC1-27-Pcdh15 EC1-2 complex.**

| **Step height gain (nm)** | **4.2±0.2** | **13.2±0.4** | **22.4±0.4** | **33.6±0.4** |
|---|---|---|---|---|
| $x_\beta$**(Å)** | 2.3±0.4 | 1.0±0.2 | 1.8±0.6 | 0.7±0.1 |
| $k_u^0$ **($s^{-1}$)** | 0.17±0.06 | 0.45±0.06 | 0.45±0.15 | 0.36±0.03 |

To accommodate the unfolding kinetics in the tip-links survival, we modified the force-induced stronger-binding model (described in section 2.2.5 in chapter 2) and incorporated the experimental unfolding probabilities. For simplicity, we included the two most-probable unfolding of ~5 nm and ~12 nm in the model and fit to the force-induced bond-dissociation dynamics of all the complex variants independently. From the fits, we obtained the intrinsic lifetime of the tip-links bond which increases with increment in the number of

EC domains. We found that zero-force lifetime is increased from ~1.5 s for Cdh23 EC1-5 to ~10 s for the Cdh23 EC1-27 complex variant. Critical force $F_{C2}$ above which catch to slip transition occurs, shifts to lower force, 108 pN to 68 pN as the length of tip-link complex increases. Further, we noted a decreasing trend in the distance to transition state ($x_\beta$), sliding rate ($k_{+1}$), and rebinding rate ($k_{+2}$) with the increasing number of domains **(Table 3)**.

**Table 3: Kinetic parameters obtained from the modified force-induced rebinding fit of lifetime-force data for different variants of Cdh23 in complexation with Pcdh15 EC1-2.**

| | $k^0_{-1}(s^{-1})$ | $x_\beta$ (Å) | $k_{+1}(s^{-1})$ | $k_{+2}(s^{-1})$ | $Fc2$ $(pN)$ | $n$ |
|---|---|---|---|---|---|---|
| Cdh23 EC1-5 | 0.6 | 1.2 | 1.2 | 20 | 108 | 1.0 |
| Cdh23 EC1-10 | 0.4 | 1.0 | 1.0 | 7.8 | 99 | 1.9 |
| Cdh23 EC1-21 | 0.2 | 0.8 | 1.1 | 1.0 | 69 | 3.8 |
| Cdh23 EC1-27 | 0.1 | 0.5 | 0.7 | 0.2 | 68 | 5.8 |

On contrary, the parameter referring to the force-enhanced binding, $n$, increases with the domain number, with the smallest value of 1.0 for 5 EC domains to the highest value of 5.8 for 27 EC domains. The lowest $x_\beta$, 0.5 Å for the full-length complex variant signifies the importance of the increased EC domains of tip-link proteins in force tolerance, lower the value higher the force resistance. Further, we observed that the sliding rate ($k_{+1}$) or the re-organization rate of the binding interface, however, remains unaffected with increasing domains. This re-organization to the stronger binding-interface is facilitated by the salt bridge, Cdh23 (E78)- Pcdh15 (R113) which itself did not show any alteration with increasing clamping forces (chapter 2, section 2.3.3). On similar lines, since the binding interface is conserved in all the truncated variants of tip-link complexes, it could explain the nearly constant values of the observed sliding rate.

## 3.4 Discussion

We showed the unfolding induced length gain before unbinding of tip-links in force-clamp measurements for all the length variants of tip-link. Four major types of protein stretching have been observed, out of which ~5 nm is probably due to straightening of the linker and associated small domain portion. Linker unfolding is enthalpically least expensive and, thus, physiologically most probable. Further, it is easier and faster for a small extension to be refold back to its original conformation once the force is released. Refolding of small extension (~4 nm) was already noticed in individual Pcdh15 unfolding studies using optical tweezers(15). Each extension elevates the lifetime of the complex providing mechanical stability to the tip-links. In platelet signaling, the force-induced unfolding of the LRRD (leucine-rich repeat domain) motif has been shown to prolong the lifetime of the VWF-GPIbα bond which forms a catch-slip bond(16, 17).

In TEM studies, the observed length distribution of the tip-links varies from 120-180 nm(18–20). These varying lengths could be due to the presence of varying conformation of tip-links(19). Especially, both Cdh23 and Pcdh15 are calcium-binding proteins and endolymphatic calcium concentration is 20-50 μM in the cochlea. This suggests some calcium-binding sites may not be saturated in physiological conditions, making the protein more flexible and vulnerable to force(1, 21, 22).

Further, an overall increase in the unfolding propensity with EC domain number elevates the bond lifetime with more force-dissemination. At higher forces, the probability of observing higher extension increases which suggest that in the case of loud sound, tip-link protein can undergo higher extension for the force-dissemination. Recent reports also suggest the gradients of gating spring stiffness from base to apex(5). Our results implicate that pulling at a high ramp induces a varying degree of unfolding, which consequently results in tip-links possessing varying stiffness. As different frequencies of sound exert varying extent of forces, so, tip-links at different parts of the cochlea may undergo different extent of unfolding, which attributes to the varied elasticity of the tip-link complex. This outcome may explain the gradient of stiffness observed in tip-links localized at different

portions of the Cochlea(5).

Further, fitting lifetime-force data to a force-induced stronger binding model gives the kinetic parameters for the unfolding-associated unbinding of the tip-links. We observed a continuous blue-shift in the critical force ($F_{C2}$) which is corresponding to maximum catch bond lifetime while going from lower to higher EC domain number of Cdh23. Also, the distance to transition state ($x_\beta$) decreases with an increase in the EC domain number. Moreover, the overall bond-lifetime increases with increasing EC domain numbers of Cdh23. Increasing domain number increases the number of inter-domain hinges and thus, the flexibility of the protein. Increasing hinge-flexibility is known to prolong bond lifetimes at small forces and thus, lowers the forces of catch-slip transitions(23). Lowering of $x_\beta$ also corroborates to less work-done and more force-dissipation as expected with increasing flexibility. We observed a significant drop in the rates of force-induced rebinding ($k_{+2}$) with increasing flexibility. Though re-binding to a stronger bound state is key for a slip to catch transitions, an increase in flexibility allows slow propagation of force through the protein and thus, a slower force-induced transition to stronger states. Notably, the rebinding-rate is many-fold faster than the intrinsic off-rate ($k^0_{-1}$) of the complex. Further, we noticed a gradual increase in the *n* value with domain numbers. *n* value indicates the interdomain angle. An increment in *n* thus implies the increase in flexibility with increasing hinge contribution in the protein. Overall, our results with varying fragments of Cdh23 marked the protein as a good candidate for force-dissipation.

## Bibliography

1. M. Sotomayor, W. Weihofen, R. Gaudet, D. P. Corey, Structure of a Force-Conveying Cadherin Bond Essential for Inner-Ear Mechanotransduction. *Nature* **492**, 128–132 (2012).

2. B. Honig, *et al.*, Mechanotransduction by PCDH15 Relies on a Novel cis-Dimeric Architecture. *Neuron* **99**, 480–492 (2018).

3. A. Jaiganesh, *et al.*, Zooming in on Cadherin-23 : Structural Diversity and Potential Mechanisms of Inherited Deafness. *Structure* **26**, 1–16 (2018).

4. J. Howard, A. J. Hudspeth, Compliance of the hair bundle associated with gating of mechanoelectrical transduction channels in the Bullfrog's saccular hair cell. *Neuron* **1**, 189–199 (1988).

5. M. Tobin, A. Chaiyasitdhi, V. Michel, N. Michalski, P. Martin, Stiffness and tension gradients of the hair cell's tip-link complex in the mammalian cochlea. *Elife*, 497222 (2019).

6. T. F. Bartsch, *et al.*, Elasticity of individual protocadherin 15 molecules implicates tip links as the gating springs for hearing. *Proc. Natl. Acad. Sci. U. S. A.* **116**, 11048–11056 (2019).

7. D. Choudhary, *et al.*, Structural determinants of protocadherin-15 mechanics and function in hearing and balance perception. *Proc. Natl. Acad. Sci. U. S. A.* **117**, 24837–24848 (2020).

8. J. Oroz, *et al.*, Nanomechanics of tip-link cadherins. *Sci. Rep.* **9**, 1–9 (2019).

9. N. Arora, J. P. Hazra, S. Rakshit, Anisotropy in mechanical unfolding of protein upon partner-assisted pulling and handle-assisted pulling. *Commun. Biol.* **4**, 1–10 (2021).

10. D. G. Gibson, *et al.*, Enzymatic assembly of DNA molecules up to several hundred

kilobases. *Nat. Methods* **6**, 343–345 (2009).

11. S. Srinivasan, J. P. Hazra, G. S. Singaraju, D. Deb, S. Rakshit, ESCORTing proteins directly from whole cell-lysate for single-molecule studies. *Anal. Biochem.* **535**, 35–42 (2017).

12. J. Brujić, R. I. Z. Hermans, S. Garcia-Manyes, K. A. Walther, J. M. Fernandez, Dwell-time distribution analysis of polyprotein unfolding using force-clamp spectroscopy. *Biophys. J.* **92**, 2896–2903 (2007).

13. Y. Cao, R. Kuske, H. Li, Direct observation of Markovian behavior of the mechanical unfolding of individual proteins. *Biophys. J.* **95**, 782–788 (2008).

14. G. I. Bell, Models for the Specific Adhesion of Cells to Cells. *Science.* **200**, 618–627 (1978).

15. T. F. Bartsch, F. E. Hengel, A. Oswald, G. Dionne, I. V Chipendo, The elasticity of individual protocadherin 15 molecules implicates cadherins as the gating springs for hearing. *Proc. Natl. Acad. Sci.* **116**, 11048–11056 (2018).

16. L. Ju, J. Lou, Y. Chen, Z. Li, C. Zhu, Force-Induced Unfolding of Leucine-Rich Repeats of Glycoprotein Ibα Strengthens Ligand Interaction. *Biophys. J.* **109**, 1781–1784 (2015).

17. L. Ju, Y. Chen, L. Xue, X. Du, C. Zhu, Cooperative unfolding of distinctive mechanoreceptor domains transduces force into signals. *Elife* **5**, 1–24 (2016).

18. V. Tsuprun, R. J. Goodyear, G. P. Richardson, The structure of tip links and kinocilial links in avian sensory hair bundles. *Biophys. J.* **87**, 4106–4112 (2004).

19. D. N. Furness, Y. Katori, B. Nirmal Kumar, C. M. Hackney, The dimensions and structural attachments of tip links in mammalian cochlear hair cells and the effects of exposure to different levels of extracellular calcium. *Neuroscience* **154**, 10–21 (2008).

20. M. Auer, *et al.*, Three-dimensional architecture of hair-bundle linkages revealed by electron-microscopic tomography. *JARO - J. Assoc. Res. Otolaryngol.* **9**, 215–224 (2008).

21. R. E. Powers, R. Gaudet, M. Sotomayor, A Partial Calcium-Free Linker Confers Flexibility to Inner-Ear Protocadherin-15. *Structure* **25**, 482–495 (2017).

22. M. Sotomayor, W. A. Weihofen, R. Gaudet, D. P. Corey, Structural Determinants of Cadherin-23 Function in Hearing and Deafness. *Neuron* **66**, 85–100 (2010).

23. J. Lou, C. Zhu, A structure-based sliding-rebinding mechanism for catch bonds. *Biophys. J.* **92**, 1471–1485 (2007).

# Chapter 4

## Heterotetramer tip-links feature slip-ideal-slip bonds under force

## 4.1 Introduction

Tip-links in the inner ear exist as a heterotetramer where the cis-homodimer of Pcdh15 involves in the trans-binding with the cis-dimer of Cdh23(1, 2). Recent studies confirmed the cis-homodimer formation of Pcdh15 in tip-links(3). Crystal structure and negative staining Transmission Electron Microscopy of the Pcdh15 showed two points of dimerization; one is the EC2-3 domain and the other is a membrane adjacent domain (MAD or Pcdh15 interacting-channel associated (PICA) domain) between EC11 and the transmembrane region(3, 4). However, no experimental and structural studies have been reported so far for the specific cis-dimerization sites of Cdh23. Though, indirect experimental and structural evidence gives a hint for Cdh23 cis-homodimer formation. Few deafness mutations in the Cdh23 present in EC7, EC14, EC17, EC20, EC21, EC23, and EC25 domains are predicted to disrupt the formation of cis-homodimer(5). Further, the squeezed crystal structure of heterotetramer, (Pcdh15 EC1-3)$_2$-(Cdh23 EC1-2)$_2$ showed that two Cdh23 come closer to each other and form a salt bridge between E50 of one protein and R53 of the other(6). Furthermore, a recent single-molecule study using optical tweezers has shown the effect of rebinding in the heterotetramer of tip-links which is facilitated by the cis-homodimerization and results in a substantial increase in the lifetime of the tip-links(7).

In chapters 2 and 3, we reported the triphasic slip-catch-slip bond lifetime behavior of single tip-link with force. The catch feature makes the tip-link more resilient toward force. Next, we wanted to further explore the effect of rebinding on the force-lifetime behavior for the heterotetramer tip-links involving parallel dimer of both the proteins. To achieve this objective, we recombinantly cloned Pcdh15 EC1-11 with the PICA domain to facilitate the cis-dimerization while Cdh23 EC1-2 and Cdh23 EC1-27 tagged with the Fc-region at C-terminus to bring a pair of Cdh23 protein in close proximity. We then performed similar force-clamp measurements among the dimers using AFM.

## 4.2 Experimental Section

### 4.2.1 Cloning, expression, and purification of Cdh23 proteins with Fc-region and Pcdh15 with PICA domain

We recombinantly modified the C-terminus of Cdh23 EC1-2 and EC1-27 with fragment crystallizable region (Fc-region) of a human antibody. The Fc constructs can self-ligate via disulfide linkages and bring a pair of Cdh23 proteins in close proximity. For Cdh23 EC1-2 Fc, we PCR amplified the insert using specific primers and subsequently followed the digestion and ligation protocol. For full-length Cdh23 EC1-27 Fc, we used the Gibson assembly protocol as described in chapter 3, section 3.2.1. Both the Cdh23 Fc constructs were cloned in the pcDNA3.1 (+) vector between the restriction sites NheI and XhoI.

Mouse Pcdh15 with 11 EC domains, one transmembrane, and one cytosolic domain was a gift from Dr. Raj Ladher, NCBS, Bangalore. For Pcdh15 EC1-11 PICA, we PCR amplified the full Pcdh15 plasmid up to the PICA domain using specific primers and cloned in pcDNA 3.1 (+) vector between the restriction sites KpnI and XhoI. All three constructs were sequence verified and checked by double-digestion.

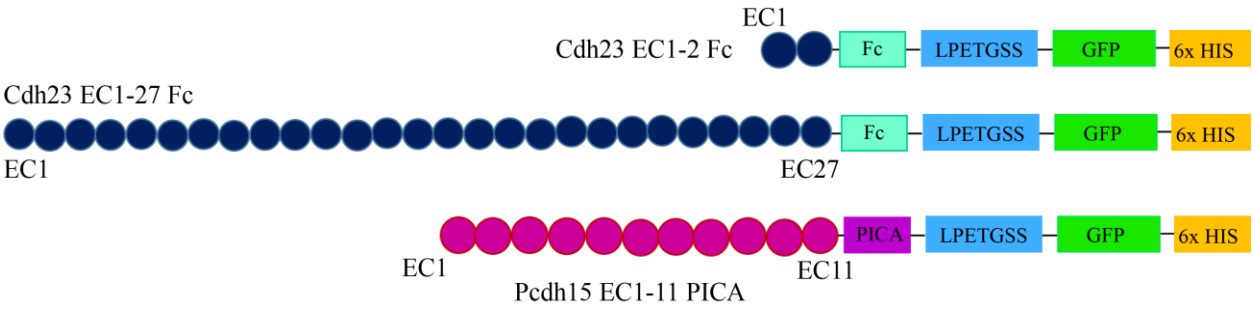


**Figure 1: Schematic of the cadherin constructs designed to form the heterotetrameric tip-links.** Cdh23 EC1-2 and Cdh23 EC1-27 (blue) modified with Fc-region at the downstream C-terminus followed by LPETGSS (sort-tag), GFP, and 6x His-tag. Pcdh15 EC1-11 (magenta) has PICA domain at C-terminus which helps in Pcdh15 dimerization.

We have incorporated the signal peptide at the N-terminus and sortase-tag, GFP, and 6x His-tag at the C-terminus of all the designed constructs. Protein expression was carried out

in suspension Expi-CHO cell lines as explained in chapter 3, section 3.2.2. After the protein expression, all the proteins were purified using Ni-NTA based affinity chromatography.

### 4.2.2 SMFS experiments using AFM

For the single-molecule experiments using AFM, we covalently immobilized one protein on the cleaned, functionalized glass coverslip and another protein on the functionalized $Si_3N_4$ cantilever. We bring the two proteins together and let them interact for 1 s followed by retracting the cantilever for 50-70 nm to break the non-specific interactions and finally clamped the protein complex at a certain constant force.

For Cdh23 EC1-2 Fc- Pcdh15 EC1-11 PICA experiment, the clamp duration at constant force was kept for 10 s while for Cdh23 EC1-27 Fc it was extended till 20 s as most of the events didn't unbind in the preset time of 10 s.

All the data analyses of lifetime measurements and step heights calculations have been performed using home-written MATLAB programs.

### 4.2.3 Langevin dynamics simulations with the polymer chains*

The semiflexible polymer is described as a bead-spring chain of N beads constituting (N-1) bonds of equilibrium length σ, where the chain length L = (N − 1)σ. The polymer has the spring constant K, and the finite bending rigidity κ. The energy of the entire polymer comes from two parts, one is the stretching of the polymer and the other is the bending of the polymer. The polymer is placed in contact with a heat bath (environment/surrounding of the polymer). This is described by the Hamiltonian(8),

$$\beta H = \sum_{i=1}^{N-1} \frac{K}{2\sigma} \left[\vec{b}_i - \vec{t}_i\right]^2 + \sum_{i=1}^{N-2} \frac{k}{2\sigma} \left[\vec{t}_{i+1} - \vec{t}_i\right]^2$$

with $\beta = 1/k_BT$, the inverse temperature of the heat bath. The bond vector $\vec{b}_i = \vec{r}_{i+1} - \vec{r}_i$, where $\vec{r}_i$ defines the position of the $i^{th}$ bead. The local tangent is defined as $\vec{t}(i) = [\vec{r}_{i+1} - \vec{r}_i]/b_i$. The monomers of the polymer occupy some space in real life and therefore they cannot penetrate each other. This change is included in the system by adding short-range

** The Langevin dynamics simulations have been performed by Sandip Roy and Dr. Abhishek Chaudhuri, IISER Mohali.*

repulsion or excluded volume interactions (a kind of potential energy). Excluded volume interactions between the non-bonded beads of the polymer are added via Weeks-Chandler-Anderson(WCA) potential(9),

$\beta V_{WCA}(r_{ij}) = 4[(\sigma/r_{ij})^{12} - (\sigma/r_{ij})^{6} + 1/4]$, if $r_{ij} < 2^{\frac{1}{6}}\sigma$

0, otherwise.

Off-rate is estimated by using the following equation(10):

$$k_{off} = k_s \exp\left(\frac{f_1 x_1}{k_B T}\right) + k_c \exp\left(\frac{-f_1 x_2}{k_B T}\right)$$

where $k_c >> k_s$, $f_1$ is the load force, $x_1$ and $x_2$ are the distance to transition state for the slip and catch energy-barrier, respectively. For simulation, the parameters used are,

$k_s = 4.2 * 10^{-6}$ s$^{-1}$, $k_c = 0.1$ s$^{-1}$, K = 5000 pN/ $\mu$ m$^2$, $\kappa$ = 4.34 pN/ $\mu$ m$^2$, N = 30, Integration time step = 0.001s.

## 4.3 Results

### 4.3.1 Partial and full-length dimer of tip-links are insensitive to force

To delineate the effect of stochastic rebinding on the force-induced bond-dissociation of tip-links, we first estimated the bond-lifetime dynamics of a partial tip-link complex comprising Pcdh15 EC1-11 PICA dimer and Cdh23 EC1-2 Fc-dimer under force. Such a simplistic model of tip-link duplex, not only reflects the effect of rebinding on the force-lifetime but also deciphers the flexibility contribution from Pcdh15 EC1-11 PICA dimer. We performed force-clamp measurements among dimers by covalently immobilizing the Cdh23 EC1-2 Fc dimer on the cantilever and Pcdh15 EC1-11 PICA dimer onto the surface **(Figure 2a)**. We estimated the survival time of recorded events and generated the survival plots. The survival probability of bonds for the dimer of tip-link complex best fitted to a bi-exponential decay **(Figure 2b and Figure 3)**.

From the fitting of survival plots, we estimated the lifetimes $\tau_1, \tau_2$ and corresponding amplitudes $A_1, A_2$. The higher bond-lifetime ($\tau_2$) component featured a slip-ideal-slip bond

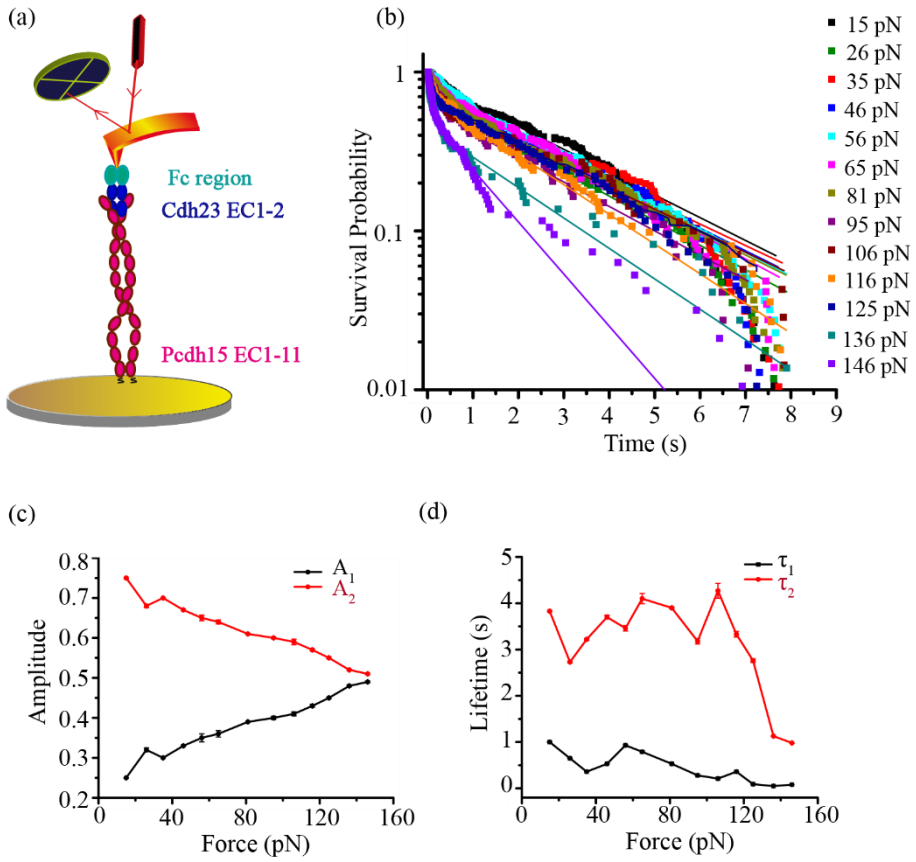


**Figure 2: Tetrameric tip-link complex feature ideal-slip bond.** (a) Schematic representation of the tetrameric tip-link complex. Cdh23 EC1-2 (blue) with Fc region (green) at the C-terminus is covalently attached to the cantilever and dimer of Pcdh15 EC1-11 PICA is attached to the surface. (b) The survival probability plot at various clamping forces is best fitted with a double-exponential decay model. (c, d) Amplitudes $A_1$, $A_2$ and lifetimes $\tau_1, \tau_2$ were obtained after fitting the survival plot. The higher lifetime component, $\tau_2$ (red) shows ideal-slip bond behavior with a decrease in corresponding amplitude with force whereas the lower lifetime component, $\tau_1$ (black) exhibits a slip-catch-slip bond feature and its corresponding amplitude continuously increases with force.

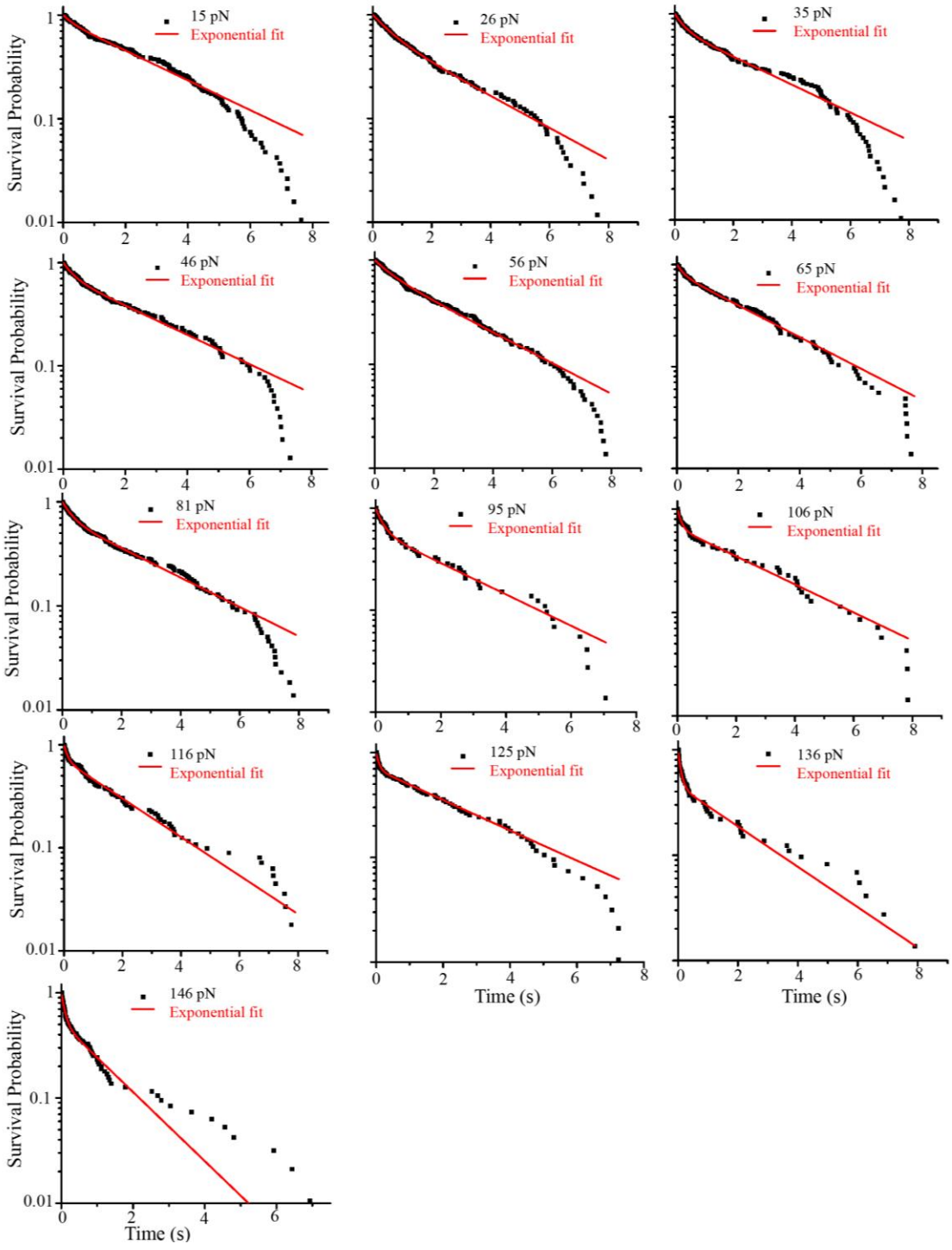


**Figure 3: Exponential decay fitting of survival plots for Cdh23 EC1-2 Fc-Pcdh15 EC1-11 PICA tip-link complex at different clamping forces.** For Cdh23 EC1-2 Fc-Pcdh15 EC1-11 PICA, double-exponential decay fitting of the survival plot is shown separately at each clamping force for clarity. Overlaid graph for the same is shown in Figure 2b.

with force **(Figure 2d)**. An ideal bond is non-responsive to the tensile force, indicating that the lifetime of the tip-link complex as doublet does not alter with force. Notably, the corresponding amplitude, $A_2$, dropped gradually with increased clamping force **(Figure 2c)**. We propose that this component is an effect of rebinding-associated dissociation. Since the probability of rebinding decreases with force, we observed a monotonous drop in $A_2$.

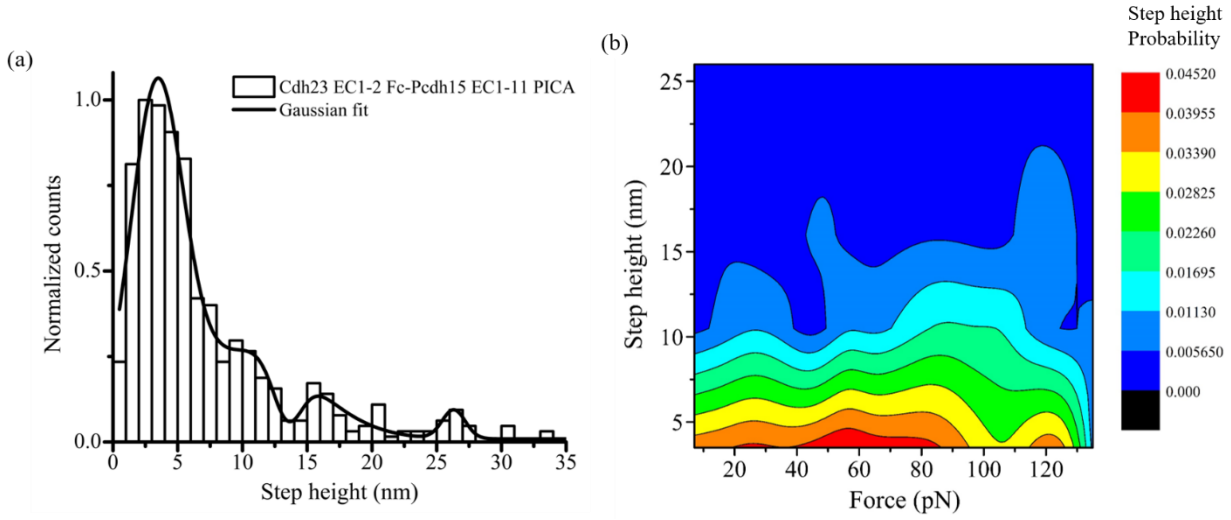


**Figure 4: Distributions of length-gains of the partial heterotetrameric tip-link complex under force.** (a) We obtained the most preferred unfolding step-height of 3.4±0.1 nm for the tip-link complex of Cdh23 EC1-2 Fc-dimers and Pcdh15 PICA cis-dimers, followed by a relatively smaller contribution from 10.5±3.5 nm, 15.6±0.4 nm, and 26.3±0.7 nm. (b) Contour plot depicting the occurrence probability of step-heights with force.

Interestingly, the lower lifetime ($\tau_1$) component displayed a slip-catch-slip bond, however, with strikingly lower bond-lifetime than the individual tip-link complex. This lower lifetime could be due to the intrinsic filtering of low-lifetime events that survived shorter than the on-time of rebinding. In other words, the fraction of interactions ($A_1$) that registered low bond-lifetime could not survive long enough for rebinding. $A_1$ showed an increasing trend with force in anti-correlation with $A_2$. Further, we observed that the cis-dimers of Pcdh15 EC1-11 PICA too respond to external tensile force and undergo stretching of 3.4±0.1 nm predominantly. Apart from the 3.4 nm extension, we do notice a

vanishingly small contribution from the stretching of larger step heights across all the applied tensile forces **(Figure 4a, b)**.

We next performed the force-clamp experiment with both the full-length cadherin doublets in tip-links, i.e., the cis-dimers of Cdh23 EC1-27 and Pcdh15 EC1-11 PICA. For cis-dimer of Cdh23, similarly, we recombinantly tagged the C-terminal of the protein with the Fc-region of the antibody. Next, for single-molecule force clamp experiments, we covalently

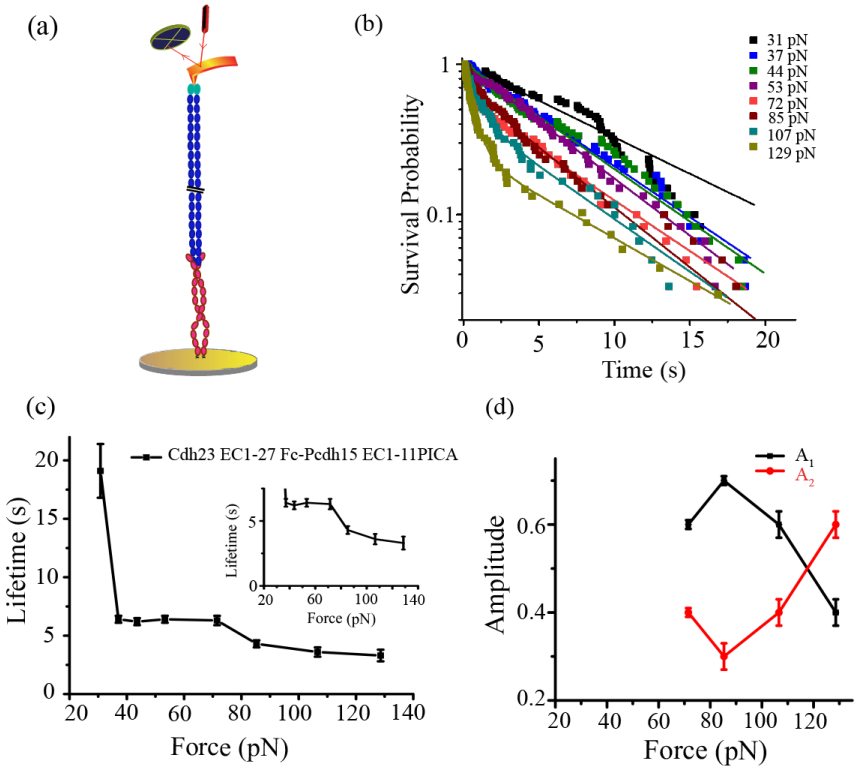


**Figure 5: Full-dimeric tip-link complex features a slip-ideal-slip bond.** (a) Schematic representation of the complete tetrameric tip-link complex. Cdh23 EC1-27 (blue) with Fc region (green) on its C-terminus is covalently attached to the cantilever while the dimer of Pcdh15 EC1-11 (PICA) is attached on the surface. (b) Survival probability plot at various clamping forces fitted with exponential decay model to obtain the bond lifetime. (c) Slip-ideal-slip bond lifetime feature of the dimeric tip-links with force. Inset shows the zoomed view of the ideal-slip bond regime. (d) Amplitudes $A_1$, and $A_2$ obtained from the double-exponential fitting of survival probability curves for forces >70 pN. Amplitude corresponding to a higher lifetime component($A_1$, black) decreases with force whereas for lower lifetime component (red) increases with force.

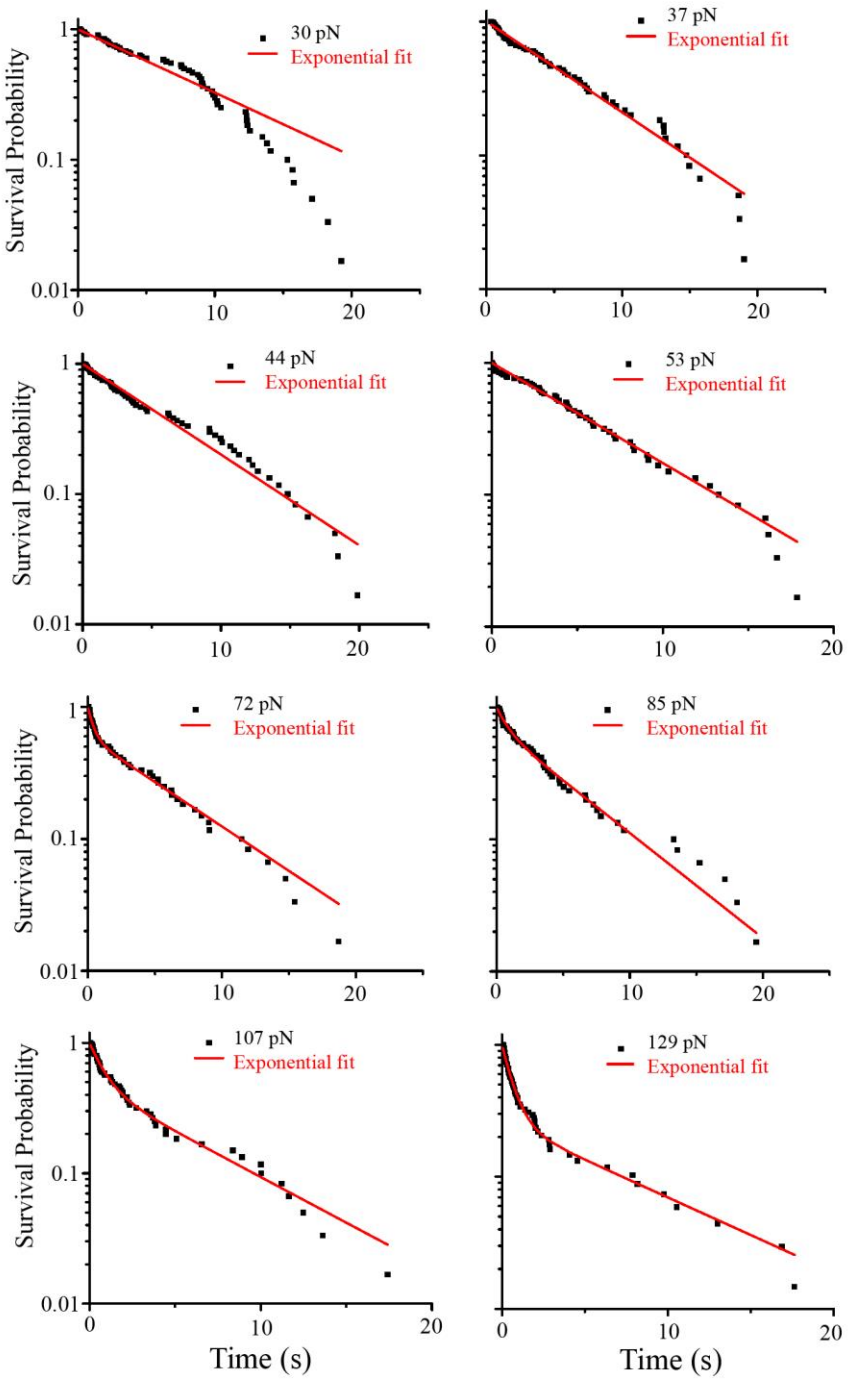


**Figure 6: Exponential decay fitting of survival plots for Cdh23 EC1-27 Fc-Pcdh15 EC1-11 PICA tip-link complex at different clamping forces.** For Cdh23 EC1-27 Fc-Pcdh15 EC1-11 PICA, exponential decay fitting of the survival plot is shown separately at each clamping force. Survival plots at low forces from 30pN to 53pN are fitted with mono-exponential decay while at higher forces from 72pN to 129pN are fitted with bi-exponential decay. Overlaid graph is shown in Figure 5b.

attached the Cdh23 EC1-27 Fc-dimer to the cantilever and Pcdh15 EC1-11 PICA dimer to the glass-coverslip **(Figure 5a)**. In the experiment, we lifted the cantilever 75 nm away from the surface prior to clamping and then clamped the complex at varying forces by further lifting the probe. The initial lift of the AFM cantilever is optimized on the basis of specific vs non-specific attachments due to the longer proteins. We found that at very low-force range, almost one-third of the clamps did not dissociate within the clamp-time of 20 s, indicating that the intrinsic bond-lifetime of the tip-links estimated from the extrapolation of slip-region may be under-valued. Further, we noted that the survival probability of tip-link complexes at high forces (> 70 pN) followed bi-exponential decays with time, instead of mono-exponents at low-forces **(Figure 5b and Figure 6)**. We suggest that at higher forces, a faster dissociation is contributing towards the second component and that may be arising from the dissociations of tip-links without rebinding as also observed for the partial heterotetramer of tip-links. Corresponding amplitudes $A_1$, and $A_2$ followed the anti-correlated trend as before **(Figure 5d)**.

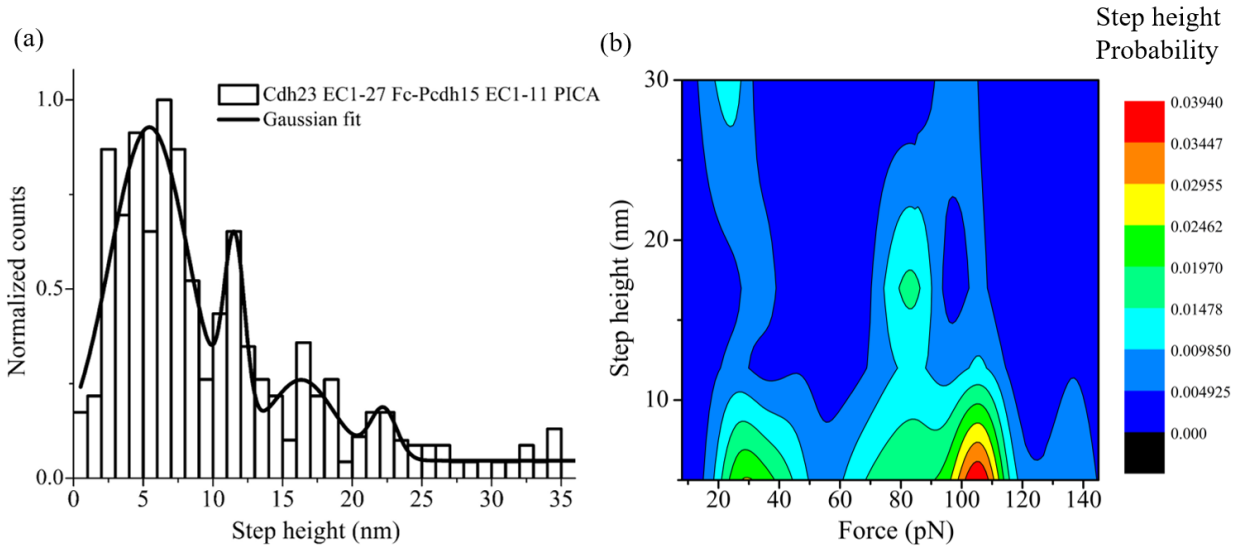


**Figure 7: Distributions of length-gains of the full-length heterotetrameric tip-link complex with force.** (a) Gaussian fitting of the step-height distribution resulted in four major peaks at 5.4±0.2, 11.5±0.2, 16.4±1.0 nm, and 22.2±0.9 nm. (b) Contour plot depicting the occurrence probability of step-heights with force

For the heterotetramer of tip-links, slip bond at low-force regime indicates a long-lasting lifetime at resting force. While an ideal bond nature does imply that the tip-link complex interface can't differentiate the magnitude of tensile forces, a filtering of force by tip-links. This ideal feature in bond-lifetime for a wide range of force is essential to perceive sound signals of any magnitude at constant efficiency.

We further noticed the force-induced extensions during the experiment. Most probable step height peak at 5.3±0.3 nm, followed by other longer step heights of 11.5±0.2 and 16.4±2.8 nm **(Figure 7)**. These force-induced length gains originated from the extension of both the constituted proteins, Cdh23 EC1-27 and Pcdh15 EC1-11.

### 4.3.2 Theoretical model for the experimental data

What is the origin of the ideal bond? Ideal-bond is not the property of the binding interface of the individual tip-link. Molecular-elasticity from the non-interacting domains only diffuses the applied tension to uplift the survival but does not alter the force-response nature of the binding interface. It is, thus, logical to hypothesize that the switch from slip-catch to slip-ideal bonds may be steered through dimerization of two independent tip-links. To understand the emergence of the slip-ideal-slip behavior in the tetrameric assembly of tip-links, we perform coarse grained Langevin dynamics simulations of coupled polymeric systems in two dimensions. We first considered an arrangement of two semiflexible filaments partially attached to one another via elastic bonds with catch-slip dissociation characteristics **(Figure 8a)**. The bonds dissociate in the presence of load when one of the filaments is pulled externally. The average lifetime of the attachment defined as the time beyond which all bonds between the two filaments break leading to two separated filaments, is plotted as a function of the external load force. The lifetime of the complex followed slip-catch-slip feature, an arrangement that mimicked individual tip-link at a coarse-grained level **(Figure 8a)**. It is important to note that the characteristic slip-catch-slip feature is independent of the stiffness of the individual filaments.

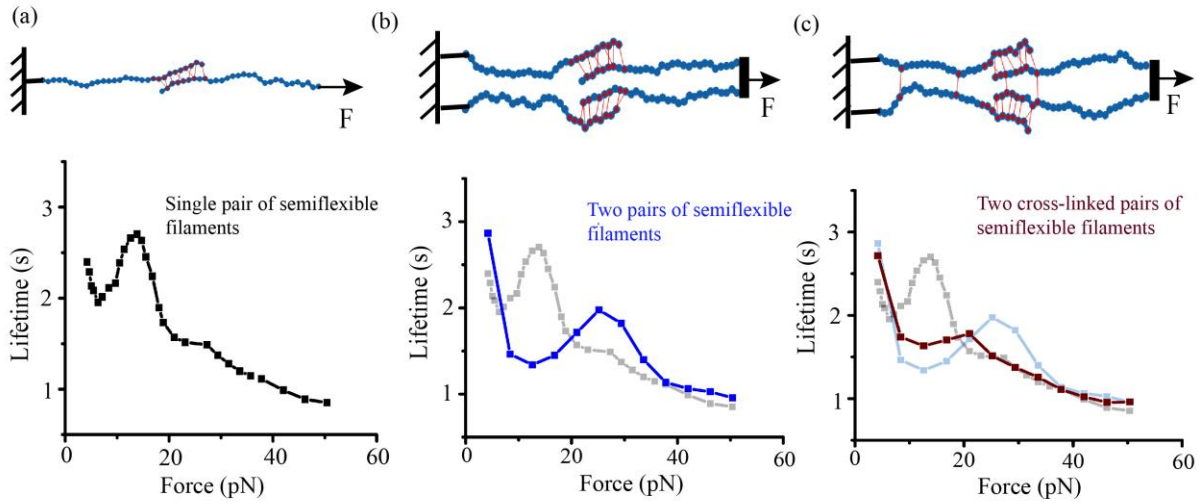


**Figure 8: The coarse grained Langevin dynamics simulations of coupled polymeric systems.** (a) Schematic representation (top) of two semiflexible filaments coupled with multiple elastic slip-catch bonds resembling the individual tip-link, and clamped at constant forces to perform the coarse-grained Langevin dynamics simulations. Bottom curve shows the resulting force-dependent lifetime that depicts the slip-catch-slip behavior. (b) Schematically representing the two pairs of the semiflexible polymers coupled and pulled in combination at constant forces. Slip-catch-slip feature remain unaltered (blue curve, bottom) for this polymer system, however, lifetime in the catch-regime is dropped compared to single pair of filaments (grey curve in background). (c) A modified polymer model from (b) where the chains from the same sides are connected. This model mimics the heterotetrameric geometry of the tip-links. The characteristic force-lifetime curve exhibits a slip-ideal-slip feature (dark red, bottom). Grey and light blue curves in the background are from model (a) and (b).

After training our dimeric system of two coupled filaments under external force, we next considered the tetrameric arrangement as shown in **Figure 8b.** Here, two filaments from each of the dimeric arrangement are pulled at one end simultaneously. We first looked at the situation where there are no elastic bonds cross-linking the two dimeric systems, except for the end monomers which are held at the same position for both. The force-response of the bonded interface still follow a slip-catch-slip characteristic, although this feature is significantly reduced in the tetrameric arrangement with the peak in the lifetime shifting to

higher force value. Finally, we cross-linked the polymers that are anchored, near terminals but away from cross-coupling region, resembling cis-dimers of Pcdh15 **(Left side chain in Figure 8c)**. We also cross-linked the polymer couples that are pulled at their cross-linking interface **(Right side chain in Figure 8c)**. This polymer couple resembles Cdh23. Cross-linking the dimeric systems via elastic bonds leads to an even further reduction in the catch-slip peak. In fact, for a choice of parameter values, we noticed the emergence of slip-ideal-slip behaviour as observed in the experiments.

## 4.4 Discussion

From the force-responsive behavior of tip-links at the single-molecule level, we observed that a heterotetramer of tip-links converts the binding interface to ideal i.e., force-independent dissociation across a large range of forces. The ideal nature of tip-links ensures the steady efficiency of hearing across all the varying sound intensities and appeared as the most appropriate mechanism for tip-links to function uniformly. However, at very high force, we noticed a transition from ideal to slip. This slip nature or dissociation of the complex at very large sound is required to protect against the disintegration of tip-links from the membrane.

Theoretically, the existence of an ideal bond is conceptualized as if the direction of force-application and bond-dissociation are orthogonal to each other. However, in our study, the origin of the ideal bond is different. Langevin dynamics simulations with the polymer chains indicate that the cis-dimeric architecture is required for the tip-links proteins to exhibit the ideal-bond feature. While previous studies suggested that the tip-links are too rigid to act as gating springs, our experimental and simulation studies demonstrated that the tip-links alone can serve as a gating spring. The dimeric conformation of the tip-links can function as a low-force pass-filter due to the existence of a slip-ideal-slip bond. At low forces, it conveys the force to the ion-channel while at higher forces, it dissipates all the extra force that makes the binding interface ideal. Thus, the unique force-conveyor and force-dissipator characteristics of the tip-links justify its role as gating spring in hearing.

## 4.5 Conclusion

In this thesis, we deciphered the mechanism used by tip-links binding interface to maintain its integrity at high range of forces. Apart from the strong binding interface, the presence of non-interacting domains of Cdh23 helps in the force-dissemination by undergoing extensions. These dynamic modulations of the protein length relax the effective tension on tip-links and uplift their survival under moderate to extreme stimuli. In addition, the rebinding in the heterotetramer of tip-links further hikes the bond-lifetime and the ideal nature makes the complex insensitive to the tensile force. A slip-ideal-slip bond in the heterotetramer of tip-links indicate that the tip-links may serve as a low-force pass filter. A low-force pass-filter aptly demonstrates the working mechanism of tip-links as gating springs which dissipate the surplus of tension from loud noise while conveying a threshold force to the mechano-gated ion-channels.

Overall, we deciphered the functional motive of the unique configuration of cadherin duos in tip-links. Our single-molecule force-clamp experiments and detailed simulations clearly demonstrated that the force-insensitive ideal-bond feature is an outcome of the hetero-tetrameric assembly of cadherins with significant contributions from the homotypic cross-links among cis-dimers. However, the overarching mechanism of such cooperative force-transmission is not clear yet.

## Bibliography

1. B. Kachar, M. Parakkal, M. Kurc, Y. Zhao, P. G. Gillespie, High-resolution structure of hair-cell tip links. *Proc. Natl. Acad. Sci.* **97**, 13336–13341 (2000).

2. P. Kazmierczak, *et al.*, Cadherin 23 and protocadherin 15 interact to form tip-link filaments in sensory hair cells. *Nature* **449**, 87–91 (2007).

3. B. Honig, *et al.*, Mechanotransduction by PCDH15 Relies on a Novel cis-Dimeric Architecture. *Neuron* **99**, 480–492 (2018).

4. P. De-la-Torre, D. Choudhary, R. Araya-Secchi, Y. Narui, M. Sotomayor, A

Mechanically Weak Extracellular Membrane-Adjacent Domain Induces Dimerization of Protocadherin-15. *Biophys. J.* **115**, 2368–2385 (2018).

5. A. Jaiganesh, *et al.*, Zooming in on Cadherin-23 : Structural Diversity and Potential Mechanisms of Inherited Deafness. *Structure* **26**, 1–16 (2018).

6. D. Choudhary, *et al.*, Structural determinants of protocadherin-15 mechanics and function in hearing and balance perception. *Proc. Natl. Acad. Sci. U. S. A.* **117**, 24837–24848 (2020).

7. E. M. Mulhall, *et al.*, Single-molecule force spectroscopy reveals the dynamic strength of the hair-cell tip-link connection. *Nat. Commun.* **12**, 1–15 (2021).

8. N. Gupta, A. Chaudhuri, D. Chaudhuri, Morphological and dynamical properties of semiflexible filaments driven by molecular motors. *Phys. Rev. E* **99**, 1–10 (2019).

9. A. Shee, N. Gupta, A. Chaudhuri, D. Chaudhuri, A semiflexible polymer in a gliding assay: reentrant transition, role of turnover and activity. *Soft Matter* **17**, 2120–2131 (2021).

10. E. A. Novikova, C. Storm, Contractile fibers and catch-bond clusters: A biological force sensor? *Biophys. J.* **105**, 1336–1345 (2013).

11. T. F. Bartsch, F. E. Hengel, A. Oswald, G. Dionne, I. V Chipendo, The elasticity of individual protocadherin 15 molecules implicates cadherins as the gating springs for hearing. *Proc. Natl. Acad. Sci.* **116**, 11048–11056 (2018).

12. J. Howard, A. J. Hudspeth, Mechanical relaxation of the hair bundle mediates adaptation in mechanoelectrical transduction by the bullfrog's saccular hair cell. *Proc. Natl. Acad. Sci. U. S. A.* **84**, 3064–3068 (1987).

13. E. A. López-Guerra, S. D. Solares, Modeling viscoelasticity through spring-dashpot models in intermittent-contact atomic force microscopy. *Beilstein J. Nanotechnol.* **5**, 2149–2163 (2014).

# *Appendix 1*

## Anisotropy in mechanical unfolding of protein upon partner-assisted pulling and handle-assisted pulling

Proteins as force-sensors respond to mechanical cues and regulate signaling in physiology. Proteins commonly connect the source and response points of mechanical cues in two conformations, independent proteins in end-to-end geometry and protein complexes in handshake geometry. The force-responsive property of independent proteins in end-to-end geometry is studied extensively using single-molecule force spectroscopy (SMFS). The physiological significance of the complex conformations in force-sensing is often disregarded as mere surge protectors. However, with the potential of force-steering, protein complexes possess a distinct mechano-responsive property over individual force-sensors. To decipher, we choose a force-sensing protein, cadherin-23, from tip-link complex and perform SMFS using end-to-end geometry and handshake complex geometry. We measure higher force-resilience of cadherin-23 with preferential shorter extensions in handshake mode of pulling over the direct mode. The handshake geometry drives the force-response of cadherin-23 through different potential-energy landscapes than direct pulling. Analysis of the dynamic network structure of cadherin-23 under tension indicates narrow force-distributions among residues in cadherin-23 in direct pulling, resulting in low force-dissipation paths and low resilience to force. Overall, the distinct and superior mechanical responses of cadherin-23 in handshake geometry than single protein geometry highlight a probable evolutionary drive of protein-protein complexes as force-conveyors over independent ones.

communications biology

ARTICLE

https://doi.org/10.1038/s42003-021-02445-y OPEN

# Anisotropy in mechanical unfolding of protein upon partner-assisted pulling and handle-assisted pulling

Nisha Arora[1], Jagadish Prasad Hazra[1✉] & Sabyasachi Rakshit[1,2✉]

Proteins as force-sensors respond to mechanical cues and regulate signaling in physiology. Proteins commonly connect the source and response points of mechanical cues in two conformations, independent proteins in end-to-end geometry and protein complexes in handshake geometry. The force-responsive property of independent proteins in end-to-end geometry is studied extensively using single-molecule force spectroscopy (SMFS). The physiological significance of the complex conformations in force-sensing is often disregarded as mere surge protectors. However, with the potential of force-steering, protein complexes possess a distinct mechano-responsive property over individual force-sensors. To decipher, we choose a force-sensing protein, cadherin-23, from tip-link complex and perform SMFS using end-to-end geometry and handshake complex geometry. We measure higher force-resilience of cadherin-23 with preferential shorter extensions in handshake mode of pulling over the direct mode. The handshake geometry drives the force-response of cadherin-23 through different potential-energy landscapes than direct pulling. Analysis of the dynamic network structure of cadherin-23 under tension indicates narrow force-distributions among residues in cadherin-23 in direct pulling, resulting in low force-dissipation paths and low resilience to force. Overall, the distinct and superior mechanical responses of cadherin-23 in handshake geometry than single protein geometry highlight a probable evolutionary drive of protein-protein complexes as force-conveyors over independent ones.

[1] Department of Chemical Sciences, Indian Institute of Science Education and Research Mohali, Mohali, Punjab, India. [2] Centre for Protein Science Design and Engineering, Indian Institute of Science Education and Research Mohali, Mohali, Punjab, India. ✉email: jagadish.hazra@gmail.com; srakshit@iisermohali.ac.in

Mechanical tension, as one of the critical cues in physiology, regulates several biological processes, including gene-expression[1–4], blood-coagulation[5], cell adhesion[6,7], muscle function[8,9], hearing[10–12], bacterial anchorage[13–15], and more. Biomacromolecules, especially proteins with unique viscoelastic properties, primarily serve as force-sensors or conveyors and orchestrate such mechanoresponsive processes. Interestingly, two configurations among the protein-based force-sensors/conveyors are commonly observed in physiology. In one, a single protein links the source and the response points of the mechanical cue in an end-to-end configuration and transmits further. Connectin protein that regulates contraction of striated muscle tissues[16,17], elastin in the extracellular (EC) matrix that imparts elasticity and resilience to tissues[18,19] fall in this category. The second configuration is more abundant in nature. The mechanical stimuli in this configuration are transmitted through protein-complexes where the protomers interact over an overlapping binding interface in a handshake configuration. Von-Willebrand factor interacts with the cell-surface glycoproteins of platelets in this configuration and facilitates blood coagulation under the mechanical cue from hydrodynamic shearing[20,21]. Nonclassical cadherins form heterophilic tip-link complexes in handshake configuration and transduce mechanical inputs in hearing and balance[22]. Other cadherins, too, form homophilic handshake complexes at the cell-cell junction and regulate morphogenesis[23]. Actomyosin complexes regulate mechanoresponsive cell-motility[24–26]. Interestingly, the function and evolution of protein-protein interactions in signal transduction are well versed, the evolutionary importance of such protein complexes in force-transduction is still elusive.

Conventionally, force spectroscopy (preferably at the single-molecule level) is utilized to decipher the thermodynamics, kinetics[27,28], and molecular mechanisms[29,30] of force-transduction through force-sensor proteins under in-vitro mechanical stimuli. In single-molecule force spectroscopy (SMFS), the protein of interest (POI) is either attached with marker polyproteins or DNA and pulled from one end with a mechanical spring. This can be described as 'handle (or hook)-assisted pulling' (HAP). In HAP, the mechanical spring-handle connects to the POI either specifically via thiol-bonds[31–33], non-covalent ligand-receptor interactions using biotin-streptavidin complexes[34], cohesin-dockerin complexes[35], Ni-NTA-His complexes[36], or non-specifically. Finally, the quantitative dependency of force-resilience on the intrinsic factors like the secondary-structure compositions, conformational entropy, short-range and long-range interactions, hydrogen-bond (H-bond) network, hydrophobic core, domain arrangements[37], etc. are deciphered from the unfolding/refolding force-extension relations. It is interesting to note that the force-response of proteins is also sensitive toward the directions of pulling. Anisotropy in the mechanical response of proteins like GFP[38,39], ankyrin[40], GB1[39,41], srcSH3[42], etc., are observed with the change in pulling direction or tethering geometry.

While SMFS undoubtedly enriched the mechanobiology of proteins, the HAP conveniently imitates the working model for type one configuration of force-sensors/conveyors. Therefore, the fundamental question, whether the HAP based force-spectroscopy is suitable to decipher the force-responsive nature of proteins in the second type of force-sensors, remains still elusive. Instead, the SMFS for the second type of force-sensing configuration is exclusively used to understand the force-resilience of the complexes but not for the constituent proteins. We define the second configuration of pulling in force spectroscopy as 'partner-assisted pulling' or PAP. Intuitively, PAP and HAP are geometrically different and expected to follow different force-resilience mechanisms. With an overarching objective of elucidating the evolutionary thirst for developing two configurationally different force-sensors, here, we plan to experimentally decipher the difference in the force-responsive properties of HAP and PAP and highlight the underlying molecular mechanisms.

To elucidate the difference between HAP and PAP, we plan to use a natural force-sensor from the second configuration but with a strong binding affinity to partners. Tip-links that serve as gating-spring in hearing[43,44] are known to form strong adhesive interactions between constituent proteins, cadherin-23 (Cdh23) and protocadherin-15 (Pcdh15)[45]. These two proteins as tip-links receive tensile forces of varying magnitudes ranging from 10 to 100 pN from sound-stimuli and convey the force to ion channels during mechanotransduction in hearing. Interestingly, the life-time of the tip-links complex is measured at varying tensile forces using PAP-based SMFS[46]; however, the force-responsive behaviour of the constituent cadherins has conveniently been measured using HAP configuration[47,48]. Whether the complex configuration of tip-link has any implication on the force-response of constituent cadherins is thus unclear. Here, we plan to utilize the strong binding affinity of the Cdh23-Pcdh15 to understand the mechanoresponsive behaviour of Cdh23 in PAP mode and decipher how PAP is different from HAP. To note, SMFS using AFM has obtained an off-rate of $4.5 \times 10^{-3} \pm 4.9 \times 10^{-5}\ s^{-1}$ and distance to the transition state of $0.18 \pm 0.03$ nm of the tip-link complex when measured using the two outermost domains of tip-link cadherins[49]. We notice higher mechanical resilience of Cdh23 during pulling in PAP mode compared to HAP. The aggravated mechanical response of Cdh23 in PAP may also have an impact on the evolution of protein-protein complexes as force-conveyors over a single spring protein.

## Results

**Design of HAP and PAP modes**. Being a nonclassical cadherin family of proteins, Cdh23 has 27 EC domains and Pcdh15 has 11 EC domains, apart from the transmembrane and cytosolic components. Two outermost EC domains at the N-terminals, EC1-2, of both cadherins overlap in a handshake geometry and form the tip-link complex[45]. For SMFS using HAP and PAP modes with an Atomic Force Microscopy (AFM), we use the entire EC region of Cdh23 (Cdh23 EC1-27). The C-terminus of Cdh23 is recombinantly modified with sortag (-LPETGSS) for covalent anchorage to glass-coverslips using sortase A[50] and expressed in mammalian Expi-CHO cell lines (Supplementary Fig. 1). For HAP, we have recombinantly modified the N-terminus of Cdh23 with Avitag (See Methods) for enzymatic conjugation of single biotin using BirA (Fig. 1a). For PAP, the N-terminus of Cdh23 is left unaltered; however, the AFM cantilever is covalently modified with Pcdh15 EC1-2 as a partner for pulling Cdh23 by utilizing tip-link complexation (Fig. 1b) (See Methods).

**HAP and PAP feature distinctly different unfolding patterns of Cdh23**. Single-molecule pulling of polyproteins comprising repeats or identical domains in tandem feature sawtooth pattern of protein-unfolding where the unfolding peaks are evenly separated along the extension. Though Cdh23 possesses multiple EC domains in tandem, such well-behaved unfolding force-extension patterns are not observed in both HAP and PAP. This is expected for Cdh23 as the EC domains, though feature similar structural architectures with seven β-strands and connecting loops, possess diversity in constituent amino acid residues with sequence similarities <30%[51]. The variety is reported even in the interdomain linkers that are usually 11–12 residues long but vary in the amino acid sequences and their affinities toward $Ca^{2+}$-ions. It is important to note that the interdomain linkers in cadherins bind with $Ca^{2+}$-ions (three for canonical linkers)[52], and reduce the conformational entropy of the proteins. Cdh23

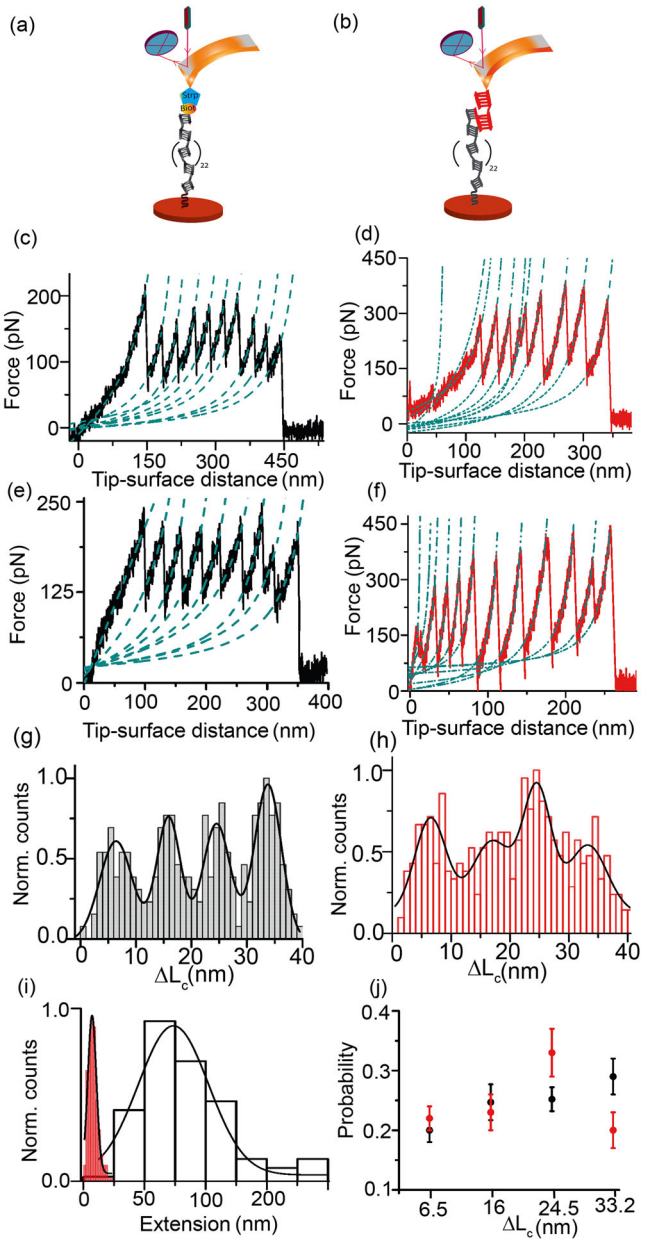


**Fig. 1 Distinct unfolding propensity of Cdh23 in HAP and PAP configurations. a** Schematic representation of HAP of Cdh23 using AFM where the C-terminus of Cdh23 is covalently attached to glass coverslip using sortagging. The N-terminal of Cdh23 is recombinantly modified with biotin and pulled by streptavidin-coated cantilevers. **b** Scheme of PAP configuration depicting the partner-assisted pulling of Cdh23 EC1-27 with Pcdh15 EC1-2 (red). **c** and **e** Representative force-extension curves of Cdh23 in HAP (black) at 2000 nm $s^{-1}$ and 3000 nm $s^{-1}$ pulling speeds, respectively. Both curves depict an initial long stretch followed by sawtooth patterns. **d** and **f** Representative force-extension features of Cdh23 in PAP (red) at 2000 nm $s^{-1}$ and 3000 nm $s^{-1}$ pulling speeds respectively. Both curves exhibit multiple unfolding peaks at the initial stretches, followed by sawtooth patterns of unfolding. The dotted green lines in (**c**–**f**) are the WLC model fit. **g** and **h** Distributions of $\Delta L_c$ of Cdh23-stretching in HAP (black line) ($n = 838$ unfolding events) and PAP (red) ($n = 946$ unfolding events), respectively. The data are combined for all loading rates. Solid lines represent the Gaussian fits exhibiting four unfolding peaks. **i** Distributions of initial long and short stretches of Cdh23 obtained in HAP (black) and PAP (red), respectively. The data are plotted for all the force curves obtained at different pulling velocities. Gaussian fittings of the histograms (solid black line) exhibit a mean length gain of 75.0 ± 2.2 nm in HAP and 6.5 ± 0.3 nm in PAP. Errors mentioned are the standard error of fitting. **j** Probability distributions of four different stretches of Cdh23 in HAP (black) and PAP (red).

possesses both canonical and noncanonical linkers. Noncanonical linkers lack the $Ca^{2+}$-affinity and bind to two or less $Ca^{2+}$-ions in physiological conditions, thus increasing the conformational entropy of proteins.

We observe multiple unfolding peaks from the single-molecule pulling of Cdh23 in both HAP and PAP (Fig. 1c–f and Supplementary Fig. 2). Interestingly, distinctly higher force resistance by Cdh23 is noticed in PAP configuration than HAP from the overall unfolding force-distributions at varying loading rates (LR) (Supplementary Fig. 3). To highlight the differential effects of pulling stereography on Cdh23, we measure the change in contour length ($\Delta L_C$) from the Worm-like chain (WLC) model fit to the force-extension curves and generate histograms of $\Delta L_C$ including all unfolding events for HAP and PAP[53] (Eq. 1, Methods). Four distributions of $\Delta L_C$ is observed for both HAP and PAP, with peak-maxima at 6.4 ± 0.4, 15.9 ± 0.3, 24.5 ± 0.3, 33.7 ± 0.2 nm and 6.5 ± 0.5, 16.9 ± 1.4, 24.6 ± 0.6, 33.2 ± 0.9 nm, respectively (Fig. 1g, h). Four distributions of $\Delta L_C$ indicate the multistep unfolding of Cdh23 in both HAP and PAP. It may be noted that the multistep unfolding is already reported from an in silico pulling of a single domain of Cdh23 (Cdh23 EC1)[54]. Further, while analyzing individual force-extension curves, we notice differences in the unfolding patterns in the spectra for both HAP and PAP (Fig. 1c–f). Incidentally, the static distribution of $\Delta L_C$ fails to highlight differences; however, the probability distributions of each extension distinctly point out the differences in unfolding preference for HAP and PAP (Fig. 1j). Across all extensions, we observe a higher probability for a shorter extension of 6.5 nm for PAP. On the contrary, the probabilities of longer stretches of 24.5 nm and 33.2 nm are dominant in HAP. Further, HAP features an initial low-force (most-probable force, $F_{mp} = 52.4 \pm 3.2$ pN) extension of 75.0 ± 2.2 nm followed by a sawtooth pattern of unfolding (Fig. 1c, e, i, & Supplementary Fig. 4). The initial low-force stretching may correspond to the entropic extension of the protein. Contrary to HAP, multiple unfoldings with short extensions with a peak-maximum of 6.5 ± 0.3 nm is preferentially observed for PAP configuration at the initial low-force regime ($F_{mp} = 44.6 \pm 2.4$ pN) (Fig. 1i & Supplementary Fig. 4).

Generally, one residue contributes 0.38 nm to the extension of a protein. Accordingly, ~6.5 nm, ~16 nm, ~24.5 nm, and ~33 nm of extensions originate from the unfolding of 17, 42, 64, and 89 residues. On average, linkers and domains are comprised of 12 and 96 residues, respectively. Therefore, ~6.5 nm and ~33 nm extensions can intuitively be attributed to the unfolding of linker and domain, respectively. Likewise, the origins of ~16 nm and ~24.5 nm extensions cannot be assigned explicitly due to a lack of in-depth knowledge on the domain-wise unfolding. These extensions may arise from the partial unfolding of domains (intermediate states) or partial unfolding of both domain and linker.

To derive the quantitative kinetic models for all four $\Delta L_C$ extensions, we segregate the unfolding events based on $\Delta L_C$ and plot the comparative unfolding force-distributions with LR for both HAP and PAP (Fig. 2a–d). Raw data for force-distributions are provided in Supplementary Data 1. Here, too, the higher unfolding forces are observed for PAP for all $\Delta L_C$ (except for ~6.5 nm) at all LR. From the Bell–Evans model fit (Eq. 2, Methods)[55,56] to the $F_{mp}$ vs. *loading rate* plots (Fig. 2e–h, Supplementary Fig. 5), we determine the intrinsic unfolding transition rates ($k_u^0$) and the widths ($x_\beta$) of their potential barriers of the extensions, and further

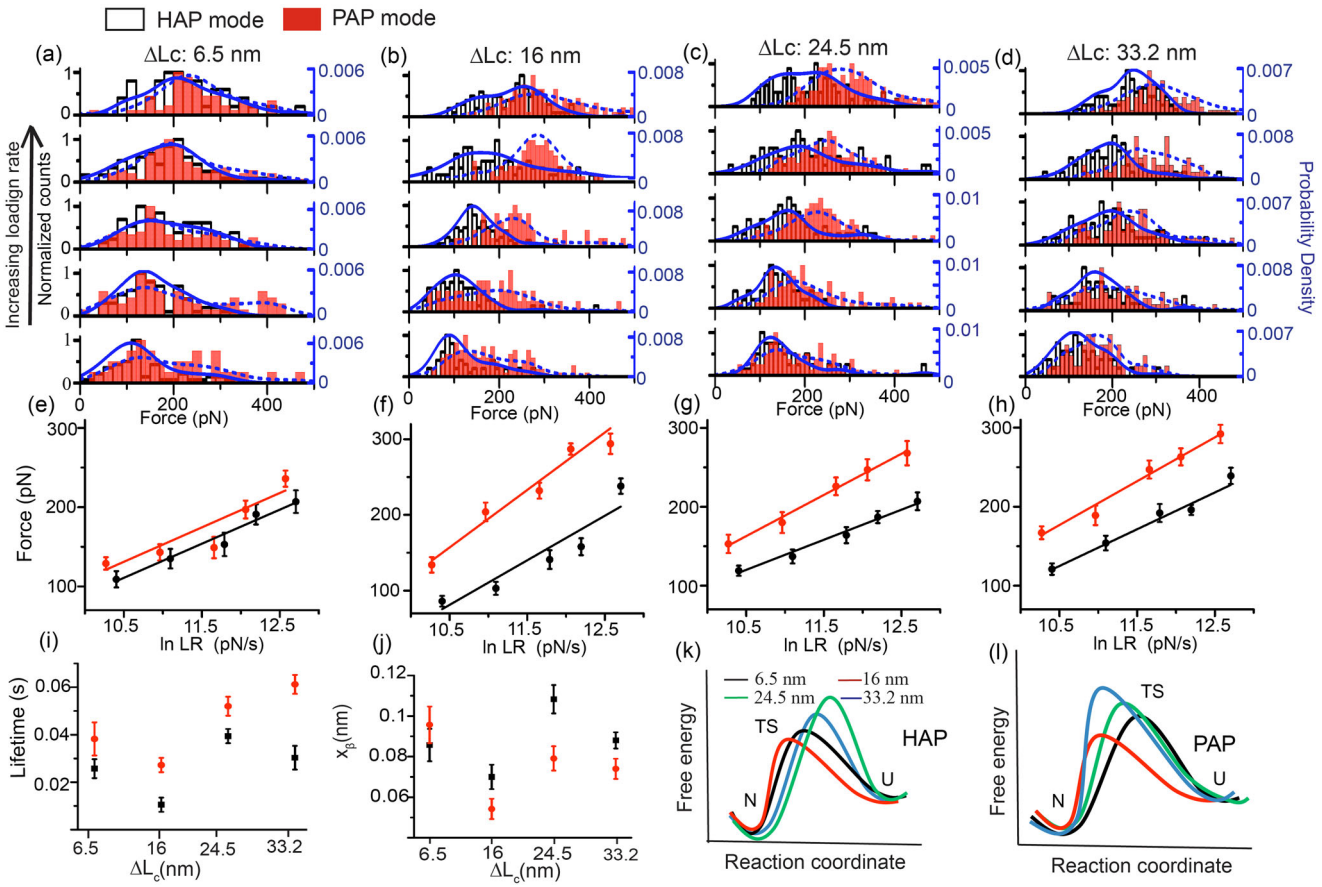


**Fig. 2 Cdh23 exhibits higher mechanical tolerance in PAP configuration compared to HAP.** The distributions of unfolding forces of Cdh23 at different pulling velocities (500, 1000, 2000, 3000, 5000 nm $s^{-1}$) have been plotted for four different extensions of (**a**) ~6.5 nm, **b** ~16 nm, **c** ~24.5 nm, and (**d**) ~33 nm for both HAP (black) and PAP (red). The solid and the dashed blue lines are the kernel density estimates (KDE) for HAP and PAP, respectively. The most probable unfolding forces are chosen from the maximum counts in the KDE. **e**–**h** The monotonous increase in the most probable unfolding forces with loading rates (loading-rate = pulling velocity × spring constant of the cantilever) is plotted for four different $\Delta L_c$s. Errors reported are the standard error. The solid lines are the Bell–Evans model fit to the force-loading rate data for (**e**) ~6.5 nm, **f** ~16 nm, **g** ~24.5 nm, and (**h**) ~33 nm. **i** and **j** Distributions of the intrinsic lifetime ($\tau_{off}$) and $x_\beta$ of all four extensions are shown respectively for HAP (black) and PAP (red) (mean ± SD from $n = 3$ independent experiments). **k** and **l** Schematics of potential energy barriers for extensions of Cdh23 of ~6.5 nm (black), ~16 nm (red), ~24.5 nm (green), and ~33 nm (blue) are drawn as per the kinetic parameters for HAP and PAP, respectively.

activation barrier height ($\Delta G^*$) of the escape-energy diagrams (Tables 1 and 2 and Supplementary Tables 1 and 2). We obtain higher $x_\beta$ and faster $k_u^0$ in HAP than PAP for $\Delta L_C$ of ~16 nm, ~24.5 nm and ~33 nm. While the faster-unfolding transition rates directly indicate easier escape in HAP (Fig. 2i), higher $x_\beta$ values (Fig. 2j) make the potential energy barrier of protein folding more susceptible to force in HAP (Fig. 2k, l, Supplementary Fig. 6). Overall, we measure four unfolding states of Cdh23 in both HAP and PAP; however, their relative populations and potential energy diagrams differ between HAP and PAP. We estimate the critical force ($F_C$) for unfolding from the kinetic parameters of protein folding, i.e., the force-equivalent to diminish the potential barrier of extensions. We notice the lowest $F_C$ for ~6.5 nm extension in PAP and ~24.5 nm extension in HAP, indicating two different most susceptible states in two pulling geometries. Incidentally, the distributions of $\Delta L_C$ do not directly reflect the same, and the discrepancy may arise from the assumption that the pulling direction (in both HAP and PAP) is always aligned with the distortion or the $x_\beta$. However, in likelihood, the pulling directions alter with extensions.

**Dynamic network structures of Cdh23 under tension differ for HAP and PAP**. PAP steers the unfolding of longer extensions through a steeper and narrower energy barrier, thus makes proteins more resilient to large perturbations in response to force than the HAP. However, the molecular mechanisms that provide more mechanical stability in proteins in PAP configuration than HAP are still elusive. To decipher, we plan for all-atom steered molecular dynamics (SMD) simulations[57,58] mimicking experimental PAP and HAP methods and perform dynamic network analysis to identify the structural contributions in force-dissipation for both PAP and HAP[59]. We further construct the force-propagation pathways in the proteins in response to mechanical tension using the Floyd–Warshal algorithm from the dynamic network structure of the protein.

However, the major roadblock for SMD of Cdh23 is its giant length of EC domain (Cdh23 EC1-27, MW: 320 kD) and lack of structural knowledge of all the EC domains[51]. We, therefore, use a truncated variant of Cdh23, Cdh23 EC1-5 that can form the complete complex with Pcdh15 as in tip-links (EC1-2 of Cdh23 and Pcdh15) and also propose the force-propagation pathways through the noninteracting domains after mechanical perturbations. Among EC1-5 of Cdh23, only EC1-3 is structurally solved (PDB: 5W4T). We thus modeled the EC 4-5 domains using the I-TASSER server[60,61] and aligned EC1-3 and EC 4-5 in PyMOL[62] based on amino acid sequence match. Next, we used the aligned

**Table 1 The kinetic parameters of all unfolding steps of Cdh23 EC1-27 in PAP mode.**

| Extension (nm) | Lifetime (s) (mean ± s.d.) | Transition state distance ($x_\beta$) (nm) (mean ± s.d.) | Energy barrier ($\triangle G^*$) | $F_C(pN) = \triangle G^*/x_\beta$ |
|---|---|---|---|---|
| 6.5 ± 0.5 | 0.038 ± 0.007 | 0.096 ± 0.009 | 17.4 $k_BT$ | 181.2 |
| 16.9 ± 1.4 | 0.027 ± 0.003 | 0.054 ± 0.005 | 17.1 $k_BT$ | 316.6 |
| 24.6 ± 0.6 | 0.052 ± 0.004 | 0.079 ± 0.006 | 17.7 $k_BT$ | 224.0 |
| 33.2 ± 0.9 | 0.061 ± 0.004 | 0.074 ± 0.005 | 17.9 $k_BT$ | 241.9 |

**Table 2 The kinetic parameters of all unfolding steps of Cdh23 EC1-27 in HAP mode.**

| Extension (nm) | Lifetime(s) (mean ± s.d.) | Transition state distance ($x_\beta$) (nm) (mean ± s.d.) | Energy barrier ($\triangle G^*$) | $F_C(pN) = G/x_\beta$ |
|---|---|---|---|---|
| 6.4 ± 0.4 | 0.026 ± 0.004 | 0.086 ± 0.008 | 17.1 $k_BT$ | 198.8 |
| 15.8 ± 0.3 | 0.010 ± 0.003 | 0.071 ± 0.006 | 16.2 $k_BT$ | 228.2 |
| 24.5 ± 0.3 | 0.039 ± 0.003 | 0.108 ± 0.007 | 17.5 $k_BT$ | 162.0 |
| 33.7 ± 0.2 | 0.030 ± 0.005 | 0.088 ± 0.004 | 17.2 $k_BT$ | 195.4 |

structures of Cdh23 domains (EC 1-3 and EC 4-5) and constructed the Cdh23 EC1-5 using template-based homology modeling in SWISS-MODEL[63]. Finally, we minimized the energy of the modeled Cdh23 EC1-5 structure using all-atom Gaussian Accelerated Molecular Dynamics (GAMD) simulations using NAMD (version 2.14) (See Methods). CHARMM36 force field and TIP3P water model are used for the simulations. Finally, the refined structures from GAMD are used in the constant velocity SMD simulations at three relatively slow pulling velocities, 1 Å/ns, 2.5 Å/ns, 5 Å/ns, and with spring of stiffness 7 kcal $mol^{-1}$ $Å^{-2}$. To model the HAP configuration in SMD we anchored the C-terminus of the protein and pulled from N-terminal (Fig. 3a). For PAP configuration, we first obtained the complex structure of Cdh23 EC1-5 and Pcdh15 EC1-2 from the homology modeling of the known heterodimeric structure of Cdh23 EC1-2-Pcdh15 EC1-2 complex (PDB ID: 4AQ8). To model PAP configuration, we used the tip-link complex comprising Cdh23 EC1-5 and Pcdh15 EC1-2, where the C-terminus of Cdh23 EC1-5 was anchored and the complex was pulled from the axially opposite C-terminus end of Pcdh15 EC1-2 (Fig. 3b).

We construct the dynamic network structure of the protein from the correlation of positional fluctuations of residues over a large number of SMD trajectories. We consider SMD trajectories till the domain unfolding. αC atoms of all residues are regarded as nodes in the network structure. Edges in the network are created between nodes if both of them stay within the vicinity of 4.5 Å for 75% of the simulation time. To illustrate the physical meaning of a network structure, we then perform the centrality measurements and deduce the importance of nodes in the network. 'Closeness centrality' denotes the inverse of all possible shortest distances from one node to others[64,65]. A Higher value of closeness centrality of a node indicates shorter distances to all other connected nodes. Thus, the traverse of information (directed mechanical tension) is more effective through a node possessing higher closeness centrality. We measure higher closeness centrality for each residue in HAP than PAP (Fig. 3c), indicating that the transfer efficiency of mechanical force is more elevated in the HAP mode of unfolding. 'Betweenness centrality' of a node denotes the number of times it falls in the shortest distance between two nodes. We estimate higher betweenness centrality of residues in PAP than HAP (Fig. 3d), indicating a more compact, homogeneous, and well-connected residue in PAP than HAP. Overall, the high betweenness centrality and low closeness centrality for PAP suggest a dense intramolecular communication for information passage in PAP than HAP, and thus a better dissipation of information in PAP over HAP.

To identify the web of nodes critical for information transmission, we determine all possible suboptimal paths of force-propagation that are within the 20 nodes from the optimal path. As reported previously, suboptimal paths of force transmission from one protein to the partner in PAP pass through an orthogonal pathway, thus reducing mechanical perturbation on the partner complex[49,66]. Further, we notice a wider spread of suboptimal paths throughout the β-strands and loops in the noninteracting domains of Cdh23 EC1-5 in PAP configuration (Fig. 3f), indicating high efficiency in force-dissipation. Whereas, in HAP, the suboptimal paths instead follow narrow spreading in Cdh23 EC1-5, encompassing fewer nodes. The narrow distribution of the paths limits the propagation of external stimuli through a smaller number of nodes, hence less dissipation of stimuli, making the protein vulnerable toward mechanical force (Fig. 3e).

**PAP is equivalent to spatially distributed multiple-point pulling over a single-point pulling in HAP**. In HAP, the first point of pulling is at the terminal where force transmission occurs from the handle to the anchored protein via a single point. Whereas, in PAP, the force transmission from one protein to the partner depends on the binding strength and the area of the binding interface. The Cdh23-Pcdh15 complex engages in multiple H-bonds and salt-bridge interactions between the interacting EC1-2 domains. Thus, an applied mechanical tension at the C-terminal of Pcdh15 transfers to Cdh23 at multiple points in the binding interface (Fig. 3f, Supplementary Fig. 7). We, therefore, hypothesize that the PAP mode is stereographically a 'spatially distributed multiple-point pulling' of HAP. To test, we have identified the residues on Cdh23 that fall in the suboptimal paths of force transmission from Pcdh15 to Cdh23 with high probability. We then perform SMD simulation by anchoring the C-terminal of Cdh23 and pulling the Arg(71), Gln(137), Ser(142) in independent simulations (Fig. 3g, inset). The SMDs mimic the HAP mode of pulling except for different pulling residues. Subsequently, we determine the suboptimal path of force propagation for individual SMD trajectory and superimpose all paths on Cdh23 E C1-5 (Fig. 3g). As expected, the combined network of three different SMDs from three different residue pulling shows the characteristics of suboptimal paths obtained in PAP mode. Paths are widely distributed throughout β-strands in the individual domain, thus validating our hypothesis that PAP mode of pulling can be attributed to a spatially distributed multipoint pulling scenario.

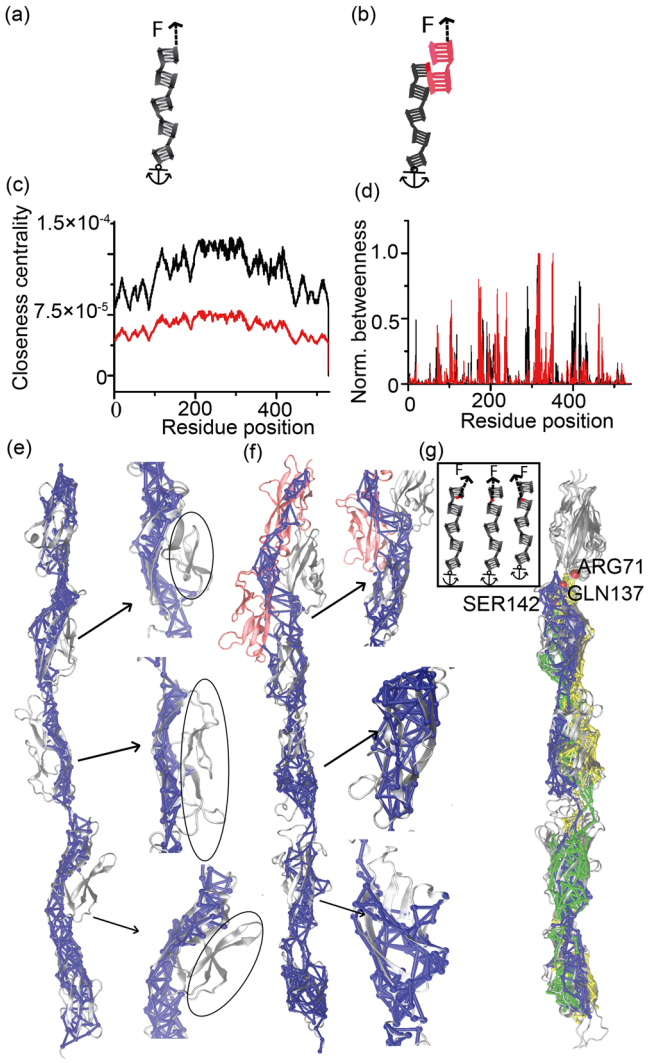


**Fig. 3 Dynamic network structures of Cdh23 under tension in HAP and PAP modes. a** Schematic representation of HAP in SMD. Black blocks represent the domains of Cdh23 EC1-5, where the C-terminal is anchored, and the N-terminal is pulled with a spring. **b** Schematic representation of PAP in SMD, depicting Cdh23 EC1-5 in black and Pcdh15 EC1-2 in red. Arrows guide the direction of the force. **c** Closeness centrality obtained for all the residues of Cdh23 EC1-5 in HAP (black) and PAP (red) configurations have been plotted. Residues register a higher closeness centrality value in HAP compared to PAP. **d** Normalized betweenness centrality obtained for all the residues of Cdh23 EC1-5 in HAP (black) and PAP (red) shows higher betweenness values in PAP than HAP for most of the residues. **e** All the sub-optimal force-propagation paths (blue) from N-termini of Cdh23 EC1-5 to C-termini for HAP obtained from a dynamic network analysis of SMD pulling trajectory are overlaid on the ribbon structure of Cdh23 EC1-5 (gray). Here, solid blue tubes denote edges, and blue spheres denote nodes. Arrows guide the zoomed regions of respective EC2, EC3, EC4 domains and the domain regions devoid of any suboptimal path of force propagation are marked with black oval lines. **f** Sub-optimal force-propagation paths for PAP overlaid on the ribbon diagram of complex Cdh23 (EC1-5) -Pcdh15 (EC1-2). Zoomed regions of EC2, EC3, and EC4 highlight the widely distributed sub-optimal paths in all the strands of domains, unlike suboptimal paths in HAP of Cdh23. **g** Inset shows schematics of three independent SMD simulations of Cdh23 EC1-5 pulling from residues R71, Q137, and S142 and anchoring C-termini of Cdh23 EC1-5. Suboptimal paths of force propagation are constructed for all three independent simulations. Suboptimal paths obtained from pulling using R71 (yellow), Q137 (blue), S142 (green) are overlaid on the cartoon representation of Cdh23 EC1-5 (gray).

## Discussion

Mechanical force orchestrates many significant biological processes via directly triggering signaling pathways, inducing allostery, altering conformations of bio-macromolecules, and changing ligand-receptor affinities or more. Nature has thus developed various biological force sensors/conveyors (natural spring) to aid the process of force perception in organisms. Some force-sensors bridge the loading point and support point independently and respond to mechanical stimuli directly. Titin protein that defines the elasticity of muscle is the most popular member in this group. Generally, springs in this group perceive a higher magnitude of mechanical stimuli. The other group of force-sensors, prevalent in nature, are protein-protein complexes with an overlapping binding interface. Tip-links, cell-adhesion complexes are typical examples in this group. They perceive a relatively low magnitude of force. While the mechanics of the independent force sensors have extensively been elucidated using state-of-the-art single-molecule manipulation tools, the functional difference of the second type of force-sensors is largely missing. A clear understanding of the functional difference may lead us to identify the evolutionary thirst of nature for both types of force-sensors. Using an AFM-based force-generator, here we decipher the differences in the force-responsive properties of a biological spring protein, Cdh23, between direct pulling (HAP) and indirect pulling via a partner (PAP).

The mechanical response of Cdh23 differs in HAP and PAP. In PAP mode, Cdh23 not only withstands a higher magnitude of force than HAP but also prefers unfolding with the shorter extension of contour lengths. The shorter extension of Cdh23 of ~6.5 nm refers to linker extension. Preference in linker extension over domain unfolding in PAP may facilitate the faster response of tip-links as force-conveyor as well as dissipater. It may be noted that force-induced extension in contour length directly relates to energy-dissipation. Lower the extension, lower is the dissipation, conversely lower energy storage with the folded form. Thus, it is pertinent to say that the protein-complex as force-conveyor may be effective at the low-force stimuli. The potential energy landscape of unfolding of Cdh23 also differs between HAP and PAP; noticeably, the width ($x_\beta$) of the potential barrier is higher in HAP than PAP. Higher resistance to mechanical perturbation and steep potential barrier of protein unfolding in PAP clarifies why unbinding of protein-protein complexes under force in SMFS rarely notice any unfolding prior to dissociation. In contrast, the same force range is sufficient to unfold proteins via direct pulling[67–69].

In-depth analysis of the dynamic network structures of Cdh23 under mechanical tension reveals higher efficacy in the information transformation through the amino acid residues in Cdh23 during HAP than PAP. Mechanical stimulus is the information here. Efficient force transfer makes the amino acid network in Cdh23 less mechano-resistive in HAP. Estimation of force propagation pathways that correlate with the mechnaostability of proteins supports the distinct differences between HAP and PAP. In HAP, the sub-optimal paths of force propagation from the force-loading point to support point are narrowly distributed among Cdh23 domains, thus impeding the load distribution evenly throughout Cdh23, effectively reducing the dissipation efficiency of external mechanical perturbations. In PAP, the force propagation from the force-loading partner to support partner transmits through orthogonal paths, thus limiting the effective work done by the force on support protein instantaneously. Further, the suboptimal paths of force-propagation through Cdh23 are evenly distributed throughout the domains, thus involving a large number of amino acid residues in disseminating the external perturbations and making the complex spring less vulnerable.

Why are the suboptimal paths distributed throughout the domains of Cdh23 in PAP? We hypothesized that the simultaneous pulling of Cdh23 from spatially distributed multiple points in PAP is responsible for the difference in mechanoresponse in oppose to terminal pulling in HAP. Anisotropy in the mechanoresponse of proteins with the pulling geometry and directions is known[38,40]. We thus refer PAP as combinations of the anisotropic response of proteins when simultaneously pulled from spatially distributed multiple points, thus effectively at multiple directions. Accordingly, we run three independent SMD simulations on Cdh23 EC1-5 pulling from the three most probable residues that lie at the overlapping interface of the complex and play a seminal role in force transmission from Pcdh15 to Cdh23. Combined suboptimal paths from all three SMD trajectories show that the network is well distributed throughout the domains. So, pulling from one point in the HAP mode concentrates the force on certain paths rather than distributing it throughout the complex, making certain regions extremely vulnerable toward applied force and initiates unfolding of domains in Cdh23. Contrary to HAP, multiple points of force transmission to Cdh23 in PAP diverge the applied force throughout the domains of Cdh23 protein and reduce the effect of applied force on the domains.

## Conclusion

Force application on Cdh23 using its interacting partner Pcdh15 and traditional handle-assisted pulling from terminals (using streptavidin-biotin conjugate handle here) yield variable elastomeric responses of Cdh23 exhibiting stronger mechanical fold architecture in the preceding approach. Stronger mechanical fold architecture is inferred from the higher force-resilience properties in SMFS studies. Higher force-resilience is attributed to the multipoint force application in a partner-assisted pulling leading to distribution of force throughout Cdh23 fold modules. A narrow distribution of force in distinct regions of Cdh23 is noticed in direct pulling using streptavidin-biotin conjugation. Our study may infer that the force-sensors in the inner ear as a heteromeric complex of Cdh23 and Pcdh15 provide extra resilience to input force from a wide range of sound stimuli (5–120 dB in human). Although, the universal applicability of our method requires extensive study with other elastic protein systems in both of the force-steering configurations, our findings indicate the importance of measuring the viscoelastic properties of biological springs in their physiological configuration.

## Materials and methods

**Cloning, expression, and purification of mammalian expressed proteins**. We recombinantly modified the N-terminus of Cdh23 EC1-27 construct with Avitag (15 amino acid sequence, PLGGIFEAMKMELRD)[70] and the C-terminus with sort-tag (LPETGSS), GFP, and 6× His-tag, respectively. While GFP was to monitor the expression level, the sort-tag was used to covalently attach the protein onto the surface for force spectroscopy studies. Avitag was used for HAP using streptavidin-biotin. Further, to express the protein in the media, we included a signal peptide sequence before Avitag. All constructs, recombinant Cadh23 EC1-27 and Pcdh15 EC1-2, were cloned in pcDNA3.1 (+) vector for expression. All proteins were expressed in the Expi-CHO expression system (ThermoFisher Scientific). Transfection was done according to the manufacturer's guidelines and then incubated for 7 days. After 7 days, we centrifuged the cells at 2000 *rpm* for 15 min and collected the media. We dialyzed the media in HEPES buffer at 4 °C and purified the proteins using $Ni^{2+}$-NTA (Qiagen) based affinity chromatography. The composition of the buffer is: 25 mM HEPES, 50 mM KCl, 200 mM NaCl, and 50 μM $CaCl_2$ (pH-7.6)(Hi-Media). After purification, the presence of proteins was confirmed from the SDS-PAGE and western blots.

**Surface modification protocol**. Glass-coverslips were activated using air plasma and subsequently washed with piranha solution for 2 h, followed by a thorough wash with deionized water. Coverslips were then etched using 1 M KOH for 15 min and washed with deionized water by sonicating for 10 min three times. Subsequently, the surfaces were silanized using v/v 2% APTES (3-Aminopropyltriethoxy silane) (Sigma-Aldrich) in 95% acetone and cured at 110 °C for 1 h. The amine exposed surfaces were reacted with Maleimide-PEG-Succinimidyl ester (Mal-PEG2-NHS) (Sigma-Aldrich) in a base buffer (100 mM $NaHCO_3$, 600 mM $K_2SO_4$, pH 8.5) for 4 h. The PEGylated surfaces were subsequently incubated with 100 μM polyglycine peptide, GGGGC, at room temperature (RT) for 7 h for cysteine–maleimide reaction. Polyglycine on coverslip acts as a nucleophile for sortagging. Coverslips were then washed thoroughly with water and stored in a vacuum desiccator prior to protein attachment.

We used less stiff $Si_3N_4$ cantilevers (NITRA-TALL from AppNano Inc., USA) for force-spectroscopy studies. After silanization, the cantilevers were treated differently for PAP and HAP. For PAP, the cantilevers were PEGlyated with Maleimide-PEG-Succinimide ester (Mal-PEG2-NHS), and then Polyglycine reaction was performed as described above to attach Pcdh15 EC1-2 covalently.

For HAP, after silanization, cantilevers were PEGylated with NHS-PEG2-NHS followed by incubation with 0.1 mg/mL Streptavidin (Sigma-Aldrich). Finally, cantilevers were washed in a buffer to remove excess streptavidin and stored at 4 °C until use.

**Single-molecule force spectroscopy using AFM**. C-terminus of Cdh23 was immobilized on the polyglycine coated glass coverslip using sortagging reaction in the presence of enzyme Sortase A[50]. After sortagging, biotinylation reaction was performed at the N-terminus of attached Avitag-Cdh23 protein using in-vitro BirA biotinylation protocol[71,72]. For this, we incubated the Cdh23 attached coverslip with mixture of Biotin (50 μM), ATP (10 mM), BirA (1 μM), $MgCl_2$ (10 mM) in low salt SEC buffer (10 mM HEPES, 50 mM KCl, 10 mM NaCl, and 50 μM $CaCl_2$) at RT for 1 h. Then, we washed the coverslip two times with buffer. Similarly, the C-terminus of Pcdh15 EC1-2 was immobilized on $Si_3N_4$ cantilevers using sortagging protocol. The Spring constant of the cantilevers was measured following the thermal fluctuation method[73]. After modifying the coverslip and cantilever with proteins, we performed dynamic force-ramp measurements using Atomic Force Microscope (AFM) (Nano wizard 3, JPK Instruments, Germany). We brought the cantilever down at 2000 nm $s^{-1}$, waited for 0.5 s for proteins to interact, and finally retracted at velocities varying from 500, 1000, 2000, 3000, and 5000 nm $s^{-1}$. At each pulling speed, we recorded 10,000 force curves. All experiments were repeated three times with fresh batch of proteins. Analyses of the force-extension curves were performed using already validated home-written MATLAB programs.

For the control experiment, we modified the surface of the coverslip with Cdh23 EC1-27 and pulled the protein with polyglycine-coated cantilevers via non-specific attachments. We obtained an overall 0.4 ± 0.2% of events for each loading rate which is 1/5 times lower than specific pulling either in HAP or PAP. Further, we observed an end-to-end extension of 48.7 ± 1.2 nm for all the events obtained in the control experiment, whereas end-to-end extension for specific pulling peaks at 256.6 ± 27.2 nm in HAP and 186.6 ± 24.4 nm in PAP.

Multiple binding/unbinding is another crucial issue in SMFS. To overcome, several strategies are out in the literature. The density of molecules on surfaces is one such important parameter that is controlled to reduce multiple interactions in SMFS. Interactions with multiple molecules at a single pulling are a common problem in both HAP and PAP. We took a systematic approach to reduce such multi-molecule interactions. We control the density of specific protein molecules by using a mixture of bi-functional and mono-functional PEG at varying ratios. In our previous work (*Biochem J* (2019) 476 (16): 2411–2425), we have measured the interaction strength between Cdh23 EC1-2 and Pcdh15 EC1-2 using dynamic force spectroscopy. For Cdh23 EC1-2 vs. Pcdh15 EC1-2, where no unfolding associated unbinding was noticed, 2% bi-functional PEG was doped with mono-functional PEG. We observed more than 97% of force curves with single unbinding features, indicating that 2% surface coverage by proteins is good enough for detecting single unbinding events accurately for proteins with two domains. We then performed unbinding experiments with Cdh23 EC1-10 and Pcdh15 EC1-2 at 2% and 1% surface coverages. Notably, pulling Cdh23 EC1-10 with Pcdh15 EC1-2 undergo unfolding associated unbinding. We observed 41 ± 3% of events featuring unfolding before unbinding irrespective of surface coverage, indicating that the features are majorly contributed from unfolding associated unbinding and not from multiple unbinding. We, thereafter, fixed the surface coverage to 1% and performed experiments with Cdh23 EC1-27 by pulling with Pcdh15 EC1-2. The percentage of force curves featuring multiple unfolding did not increase significantly. However, the number of unfolding per force curves increased with domain numbers. Together with Poisson distributions, these observations indicate that our experimental data are dominated by unfolding associated unbinding and not by multiplex unbinding. However, absolute quantification of the contributions from multiple interactions is impossible in our case.

**Worm-like chain (WLC) model fit**. Unfolding force and change in contour length ($\Delta L_c$) of proteins upon unfolding was measured from the fitting of WLC equation (Eq. 1) of polymer elasticity[53] to the sawtooth force-extension patterns.

$$F(x) = \frac{k_B T}{p}\left[\frac{1}{4}\left(1-\frac{x}{Lc}\right)^{-2} - \frac{1}{4} + \frac{x}{Lc}\right] \quad (1)$$

where $F$ is the unfolding force, $p$ is the persistence length, $x$ is the end-to-end length, and $Lc$ is the contour length of the protein, $k_B$ is the Boltzmann's constant, and $T$ is the temperature. After fitting each peak, unfolding force ($F$) and contour length ($Lc$) is obtained for all different pulling velocities.

Contour length change ($\Delta L_C$) was measured from the difference between two consecutive *Lc* values of unfolding peaks and plotted as histograms. Most probable $\Delta L_C$ values were estimated from the Gaussian fitting of the histograms. Unfolding forces measured from the WLC fits were plotted as histograms for each pulling velocity. For each histogram, we construct frequency distribution using the Kernel density smoothing function (in MATLAB). For the Kernel density estimation, we determined the bandwidth using the following equation[46,74–76]

$$H = 1.06n^{-1/5}\sigma$$

H: bandwidth, n: number of measurements and $\sigma = \min\{\sigma_x, \mathrm{IQR}/1.34\}$ where $\sigma_x$: standard deviation and IQR is the interquartile range.

Further, LR were estimated directly from the multiplication of spring constant and pulling velocity of the cantilever.

Kinetic parameters such as intrinsic unfolding transition-rate ($k_u^0$) and distance to transition state ($x_\beta$) for unfolding were obtained from the fitting of $F_{mp}$ vs. loading rate plots with Bell–Evans equation[55,56].

$$F(LR) = \left(\frac{k_B T}{x_\beta}\right)\ln\frac{(LR)x_\beta}{k_u^0 k_B T} \quad (2)$$

Activation barrier height ($\triangle G^*$) was estimated from Arrhenius equation:

$$\triangle G^* = -k_B \mathrm{T}.\ln\left(k_u^0/A\right) \quad (3)$$

Here, $k_u^0$ is the unfolding transition rate, and A is the Arrhenius frequency factor. For protein dynamics, the value of A is $10^9\ \mathrm{s}^{-1}$ [38,77].

**Molecular dynamics simulation**. Systems for the MD simulations were prepared using QwikMD[58] plugin of VMD[78]. Protein was aligned to the *Z*-axis and solvated using TIP3P water system in a box maintaining a distance of 15 Å from the edges of the box. $Na^+$ and $Cl^-$ ions were placed at a final concentration of 150 mM randomly in the box. Simulations were performed using NAMD[57] version 2.14 and CHARMM36 force field[79]. After fixing the atom-positions of the protein molecule, the system was minimized for 5000 steps and then 5000 steps of system minimization without any restraints, followed by increasing the system's temperature to 300 K at a rate of 1 K for 600 steps. Equilibration of the system was performed for 5 ns. Then GAMD simulation was performed for 20 ns[80,81]. Noose–Hover method[82,83] was followed to maintain 1 atm pressure, and the Particle mesh Ewald (PME) method[83] was followed to treat the long-range interactions.

For steered molecular dynamics, we used the structure of Cdh23 EC1-5, refined from GAMD. To mimic HAP, the C-terminus of Cdh23 EC1-5 was anchored, and pulling was carried out from N-terminus. In PAP, a complex of Cdh23 EC1-5 and Pcdh15 EC1-2 was used where the C-terminus of Cdh23 EC1-5 was anchored, and pulling was performed from the C-terminus of Pcdh15 EC1-2. In the multipoint pulling scenario, pulling was performed in three independent simulations by anchoring the C-terminus of Cdh23 EC1-5 and pulling using Arg71, Ser142, and Gln137 residues of Cdh23 EC1-5. All the SMD simulations were carried out at three different pulling velocities of 1 Å/ns, 2.5 Å/ns, and 5 Å/ns.

**Dynamic network analysis**. Dynamic network analysis has been carried out using NetworkView, plugin of VMD[59] and other associated tools. For the network construction, all the α-C's were considered as nodes. Edges were created between two nodes if they lie in the vicinity of 4.5 Å of a heavy atom for 75% of the simulation time. Neighboring alpha carbon atoms were not considered for the analysis procedure as it will lead to trivial paths. Edges were weighted using correlation coefficient calculated from correlation matrix using carma[84]. Suboptimal paths were determined using subopt script of VMD, which uses the Floyd–Warshal algorithm[85]. For HAP, we estimated the suboptimal paths between the N-terminus and C-terminus of Cdh23 EC1-5. For PAP, the estimation of suboptimal paths started from the C-terminus of Pcdh15 EC1-2 and extended till the C-terminus of Cdh23 EC1-5.

**Statistics and reproducibility**. We have performed all the experiments in triplicates with fresh batch of proteins by using new set of coverslip and cantilevers. Erros are estimated as standard error from experiment replicates and standard error of fitting as applicable.

**Associated content**. Supplementary figures and tables are attached separately in supplementary document.

**Reporting summary**. Further information on research design is available in the Nature Research Reporting Summary linked to this article.

## Data availability

The source data underlying the graphs are available as Supplementary Data 1. Any remaining information along with original force curves are available from corresponding author upon reasonable request.

## Code availability

All home-written MATLAB codes were used for the analysis and codes are available at a Github repository https://github.com/Singlemoleculelab-IISERM/Arora-et-al-Communicaton-Biology[86].

Received: 10 February 2021; Accepted: 7 July 2021;
Published online: 29 July 2021

## References

1. Tajik, A. et al. Transcription upregulation via force-induced direct stretching of chromatin. *Nat. Mater.* **15**, 1287–1296 (2016).
2. Therizols, P. et al. Chromatin decondensation is sufficient to alter nuclear organization in embryonic stem cells. *Science* **346**, 1238–1242 (2014).
3. Miroshnikova, Y. A., Nava, M. M. & Wickström, S. A. Emerging roles of mechanical forces in chromatin regulation. *J. Cell Sci.* **130**, 2243–2250 (2017).
4. Strzyz, P. Mechanotransduction: may the force be with you. *Nat. Rev. Mol. Cell Biol.* **17**, 533 (2016).
5. Qiu, Y., Myers, D. R. & Lam, W. A. The biophysics and mechanics of blood from a materials perspective. *Nat. Rev. Mater.* **4**, 294–311 (2019).
6. Parsons, J. T., Horwitz, A. R. & Schwartz, M. A. Cell adhesion: integrating cytoskeletal dynamics and cellular tension. *Nat. Rev. Mol. Cell Biol.* **11**, 633–643 (2010).
7. Leckband, D. & Prakasam, A. Mechanism and Dynamics of Cadherin Adhesion. *Annu. Rev. Biomed. Eng.* **8**, 259–287 (2006).
8. Lemke, S. B. & Schnorrer, F. Mechanical forces during muscle development. *Mech. Dev.* **144**, 92–101 (2017).
9. Felsenthal, N. & Zelzer, E. Mechanical regulation of musculoskeletal system development. *Development* **144**, 4271–4283 (2017).
10. LeMasurier, M. & Gillespie, P. G. Hair-cell mechanotransduction and cochlear amplification. *Neuron* **48**, 403–415 (2005).
11. Muller, U. & Gillespie, P. G. Mechanotransduction by Hair Cells: models, Molecules, and Mechanisms. *Cell* **139**, 33–44 (2010).
12. Hudspeth, A. J. How hearing happens. *Neuron* **19**, 947–950 (1997).
13. Thomas, W. E., Trintchina, E., Forero, M., Vogel, V. & Sokurenko, E. V. Bacterial adhesion to target cells enhanced by shear force. *Cell* **109**, 913–923 (2002).
14. Aprikian, P. et al. The bacterial fimbrial tip acts as a mechanical force sensor. *PLoS Biol.* **9**, 1–16 (2011).
15. Gordon, V. D. & Wang, L. Bacterial mechanosensing:the force will be with you, always. *J. Cell Sci.* **132**, 1–9 (2019).
16. Herzog, W. The role of titin in eccentric muscle contraction. *J. Exp. Biol.* **217**, 2825–2833 (2014).
17. Rief, M., Gautel, M., Oesterhelt, F., Fernandez, J. M. & Gaub, H. E. Reversible unfolding of individual titin immunoglobulin domains by AFM. *Science* **276**, 1109–1112 (1997).
18. Urry, D. W. et al. Elastin: a representative ideal protein elastomer. *Philos. Trans. R. Soc. B Biol. Sci.* **357**, 169–184 (2002).
19. Black, L. D., Allen, P. G., Morris, S. M., Stone, P. J. & Suki, B. Mechanical and failure properties of extracellular matrix sheets as a function of structural protein composition. *Biophys. J.* **94**, 1916–1929 (2008).
20. Reininger, A. J. Function of von Willebrand factor in haemostasis and thrombosis. *Haemophilia* **14**, 11–26 (2008).
21. Fu, H. et al. Flow-induced elongation of von Willebrand factor precedes tension-dependent activation. *Nat. Commun.* **8**, 1–12 (2017).
22. Kazmierczak, P. et al. Cadherin 23 and protocadherin 15 interact to form tip-link filaments in sensory hair cells. *Nature* **449**, 87–91 (2007).
23. Takeichi, M. Cadherin cell adhesion receptors as a morphogenetic regulator. *Science* **251**, 1451–1455 (1991).
24. Keeling, M. C., Flores, L. R., Dodhy, A. H., Murray, E. R. & Gavara, N. Actomyosin and vimentin cytoskeletal networks regulate nuclear shape, mechanics and chromatin organization. *Sci. Rep.* **7**, 1–14 (2017).
25. Wolf, K. et al. Physical limits of cell migration: control by ECM space and nuclear deformation and tuning by proteolysis and traction force. *J. Cell Biol.* **201**, 1069–1084 (2013).
26. Heisenberg, C. P. & Bellaïche, Y. Forces in tissue morphogenesis and patterning. *Cell* **153**, 948–962 (2013).
27. Wiita, A. P., Ainavarapu, S. R. K., Huang, H. H. & Fernandez, J. M. Force-dependent chemical kinetics of disulfide bond reduction observed with single-molecule techniques. *Proc. Natl Acad. Sci. U. S. A.* **103**, 7222–7227 (2006).
28. Guinn, E. J., Jagannathan, B. & Marqusee, S. Single-molecule chemo-mechanical unfolding reveals multiple transition state barriers in a small single-domain protein. *Nat. Commun.* **6**, 1–8 (2015).
29. Marszalek, P. E. et al. Mechanical unfolding intermediates in titin modules. *Nature* **402**, 100–103 (1999).

30. Li, L., Huang, H. H. L., Badilla, C. L. & Fernandez, J. M. Mechanical unfolding intermediates observed by single-molecule force spectroscopy in a fibronectin type III module. *J. Mol. Biol.* **345**, 817–826 (2005).
31. Grandbois, M., Beyer, M., Rief, M., Clausen-Schaumann, H. & Gaub, H. E. How strong is a covalent bond. *Science* **283**, 1727–1730 (1999).
32. Zimmermann, J. L., Nicolaus, T., Neuert, G. & Blank, K. Thiol-based, site-specific and covalent immobilization of biomolecules for single-molecule experiments. *Nat. Protoc.* **5**, 975–985 (2010).
33. Cecconi, G., Shank, E. A., Bustamante, C. & Marqusee, S. Biochemistry: direct observation of the three-state folding of a single protein molecule. *Science* **309**, 2057–2060 (2005).
34. Sedlak, S. M. et al. Monodisperse measurement of the biotin-streptavidin interaction strength in a well-defined pulling geometry. *PLoS ONE* **12**, 1–16 (2017).
35. Vera, A. M. & Carrión-Vázquez, M. Direct Identification of Protein–Protein Interactions by Single-Molecule Force Spectroscopy. *Angew. Chem. - Int. Ed.* **55**, 13970–13973 (2016).
36. Montana, V., Liu, W., Mohideen, U. & Parpura, V. Single molecule probing of exocytotic protein interactions using force spectroscopy. *Croat. Chem. Acta* **81**, 31–40 (2008).
37. Brockwell, D. J. et al. Pulling geometry defines the mechanical resistance of a β-sheet protein. *Nat. Struct. Biol.* **10**, 731–737 (2003).
38. Dietz, H., Berkemeier, F., Bertz, M. & Rief, M. Anisotropic deformation response of single protein molecules. *Proc. Natl Acad. Sci. U. S. A.* **103**, 12724–12728 (2006).
39. Paul, S. & Venkatramani, R. Estimating the Directional Flexibility of Proteins from Equilibrium Thermal Fluctuations. *J. Chem. Theory Comput.* **17**, 3103–3118 (2021).
40. Lee, W. et al. Mechanical anisotropy of ankyrin repeats. *Biophys. J.* **102**, 1118–1126 (2012).
41. Li, Y. D., Lamour, G., Gsponer, J., Zheng, P. & Li, H. The molecular mechanism underlying mechanical anisotropy of the protein GB1. *Biophys. J.* **103**, 2361–2368 (2012).
42. Jagannathan, B., Elms, P. J., Bustamante, C. & Marqusee, S. Direct observation of a force-induced switch in the anisotropic mechanical unfolding pathway of a protein. *Proc. Natl Acad. Sci. U. S. A.* **109**, 17820–17825 (2012).
43. Assad, J. A., Shepherd, G. M. G. & Corey, D. P. Tip-link Integrity and Mechanical Transduction in Vertebrate Hair Cells. *Neuron* **7**, 985–994 (1991).
44. Qiu, X. & Müller, U. Mechanically gated ion channels in mammalian hair cells. *Front. Cell. Neurosci.* **12**, 1–10 (2018).
45. Sotomayor, M., Weihofen, W., Gaudet, R. & Corey, D. P. Structure of a Force-Conveying Cadherin Bond Essential for Inner-Ear Mechanotransduction. *Nature* **492**, 128–132 (2012).
46. Mulhall, E. M. et al. Single-molecule force spectroscopy reveals the dynamic strength of the hair-cell tip-link connection. *Nat. Commun.* **12**, 1–15 (2021).
47. Bartsch, T. F., Hengel, F. E., Oswald, A., Dionne, G. & Chipendo, I. V. The elasticity of individual protocadherin 15 molecules implicates cadherins as the gating springs for hearing. *Proc. Natl Acad. Sci.* **116**, 11048–11056 (2018).
48. Oroz, J. et al. Nanomechanics of tip-link cadherins. *Sci. Rep.* **9**, 1–9 (2019).
49. Hazra, J. P. et al. Broken force dispersal network in tip-links by the mutations induces hearing-loss. *Biochem. J.* **476**, 2411–2425 (2019).
50. Srinivasan, S., Hazra, J. P., Singaraju, G. S., Deb, D. & Rakshit, S. ESCORTing proteins directly from whole cell-lysate for single-molecule studies. *Anal. Biochem.* **535**, 35–42 (2017).
51. Jaiganesh, A. et al. Zooming in on Cadherin-23: structural Diversity and Potential Mechanisms of Inherited Deafness. *Structure* **26**, 1–16 (2018).
52. Sotomayor, M., Weihofen, W. A., Gaudet, R. & Corey, D. P. Structural Determinants of Cadherin-23 Function in Hearing and Deafness. *Neuron* **66**, 85–100 (2010).
53. Bustamante, C., Marko, J., Siggia, E. & Smith, S. Entropic elasticity of lambda-phage DNA. *Science* **265**, 1599–1599 (1994).
54. Garg, S. et al. Weakening of interaction networks with aging in tip-link protein induces hearing loss. *Biochem. J.* **478**, 121–134 (2021).
55. Bell, G. I. Models for the Specific Adhesion of Cells to Cells. *Science* **200**, 618–627 (1978).
56. Evans, E. & Ritchie, K. Dynamic Strength of Molecular Adhesion Bonds. *Biophys. J.* **72**, 1541–1555 (1997).
57. Nelson, M. T. et al. NAMD: a parallel, object-oriented molecular dynamics program. *Int. J. High. Perform. Comput. Appl.* **10**, 251–268 (1996).
58. Rudack, T. et al. QwikMD — Integrative Molecular Dynamics Toolkit for Novices and Experts. *Sci. Rep.* **6**, 1–14 (2016).
59. Eargle, J. & Luthey-Schulten, Z. NetworkView: 3D display and analysis of protein.RNA interaction networks. *Bioinformatics* **28**, 3000–3001 (2012).
60. Roy, A., Kucukural, A. & Zhang, Y. I-TASSER: a unified platform for automated protein structure and function prediction. *Nat. Protoc.* **5**, 725–738 (2010).
61. Yang, J. et al. The I-TASSER suite: protein structure and function prediction. *Nat. Methods* **12**, 7–8 (2015).
62. DeLano, W. L. Pymol: An open-source molecular graphics tool. *Newsl. Protein Crystallogr.* **40**, 82–92 (2002).
63. Arnold, K., Bordoli, L., Kopp, J. & Schwede, T. The SWISS-MODEL workspace: a web-based environment for protein structure homology modelling. *Bioinformatics* **22**, 195–201 (2005).
64. Sethi, A., Eargle, J., Black, A. A. & Luthey-Schulten, Z. Dynamical networks in tRNA:protein complexes. *Proc. Natl Acad. Sci.* **106**, 6620–6625 (2009).
65. Böde, C. et al. Network analysis of protein dynamics. *FEBS Lett.* **581**, 2776–2782 (2007).
66. Ott, W. et al. Mapping Mechanical Force Propagation through Biomolecular Complexes. *Nano Lett.* **15**, 7370–7376 (2015).
67. Valbuena, A., Vera, A. M., Oroz, J., Menéndez, M. & Carrión-Vázquez, M. Mechanical properties of β-catenin revealed by single-molecule experiments. *Biophys. J.* **103**, 1744–1752 (2012).
68. Bajpai, S. et al. α-Catenin mediates initial E-cadherin-dependent cell- cell recognition and subsequent bond strengthening. *Proc. Natl Acad. Sci. U. S. A.* **105**, 18331–18336 (2008).
69. Wu, F. et al. Homophilic interaction and deformation of E-cadherin and cadherin 7 probed by single molecule force spectroscopy. *Arch. Biochem. Biophys.* **587**, 38–47 (2015).
70. Ie, S. C. Use of Peptide Libraries to Map the Substrate Specificity of a Peptide-Modifying Enzyme: a 13 Residue Consensus Peptide Specifies Biotinylation in Escherichia coli. *Nat. Biotechnol.* **6**, 12–17 (1993).
71. Gautier, A. & Hinner, M. J. Site-Specific Protein Labeling: Methods and Protocols. 1–267 (2015).
72. Cull, M. G. & Schatz, P. J. Biotinylation of proteins in vivo and in vitro using small peptide tags. *Methods Enzymol.* **326**, 430–440 (2000).
73. Hutter, J. L. & Bechhoefer, J. Calibration of atomic-force microscope tips. *Rev. Sci. Instrum.* **64**, 1868–1873 (1993).
74. Bura, E., Zhmurov, A. & Barsegov, V. Nonparametric density estimation and optimal bandwidth selection for protein unfolding and unbinding data. *J. Chem. Phys.* **130**, 1–15 (2009).
75. Cheng, W., Arunajadai, S. G., Moffitt, J. R., Tinoco, I. & Bustamante, C. Single-base pair unwinding and asynchronous RNA release by the hepatitis C virus NS3 helicase. *Science* **333**, 1746–1749 (2011).
76. Moffitt, J. R. et al. Intersubunit coordination in a homomeric ring ATPase. *Nature* **457**, 446–450 (2009).
77. Bieri, O. et al. The speed limit for protein folding measured by triplet-triplet energy transfer. *Proc. Natl Acad. Sci. U. S. A.* **96**, 9597–9601 (1999).
78. Humphrey, W., Dalke, A. & Schulten, K. VMD: visual molecular dynamics. *J. Mol. Graph.* **14**, 33–38 (1996).
79. Best, R. B. et al. Optimization of the additive CHARMM all-atom protein force field targeting improved sampling of the backbone φ, ψ and side-chain χ 1 and χ 2 Dihedral Angles. *J. Chem. Theory Comput.* **8**, 3257–3273 (2012).
80. Miao, Y., Feher, V. A. & McCammon, J. A. Gaussian Accelerated Molecular Dynamics: unconstrained Enhanced Sampling and Free Energy Calculation. *J. Chem. Theory Comput.* **11**, 3584–3595 (2015).
81. Pang, Y. T., Miao, Y., Wang, Y. & McCammon, J. A. Gaussian accelerated molecular dynamics in NAMD. *J. Chem. Theory Comput.* **13**, 9–19 (2017).
82. Martyna, G. J., Tobias, D. J. & Klein, M. L. Constant pressure molecular dynamics algorithms. *J. Chem. Phys.* **101**, 4177–4189 (1994).
83. Feller, S. E., Zhang, Y., Pastor, R. W. & Brooks, B. R. Constant pressure molecular dynamics simulation: the Langevin piston method. *J. Chem. Phys.* **103**, 4613–4621 (1995).
84. Koukos, P. I. & Glykos, N. M. Grcarma: a fully automated task-oriented interface for the analysis of molecular dynamics trajectories. *J. Comput. Chem.* **34**, 2310–2312 (2013).
85. Floyd, R. W. Algorithms 97. *Shortest Path Commun.* **5**, 345 (1962).
86. Arora et al. (2021) https://github.com/Singlemoleculelab-IISERM/Arora-et-al-Communicaton-Biology


## Acknowledgements

This work was supported by the Wellcome Trust/ DBT Indian Alliance fellowship [grant number: IA/I/15/1/501817] awarded to SR. SR acknowledges the financial support provided by The Wellcome Trust/DBT Intermediate fellowship by Indian Alliance and Indian Institute of Science Education and Research Mohali, India (IISERM). We thank Professor Raj Ladher, National Centre for Biological Science, India for providing Cdh23 and Pcdh15 mammalian constructs. NA is thankful to CSIR-India for providing fellowship. JPH is thankful to IISERM for the financial support.

## Author contributions

S.R. conceived the idea. J.P.H., N.A., and S.R. designed all the experiments and analyzed the data. N.A. and J.P.H. expressed and purified the proteins. J.P.H. and N.A. made the figures. J.P.H. and S.R. wrote the paper. N.A., S.R. and J.P.H. edited the paper.

## Competing interests

The authors declare no competing interests.

## Additional information

**Supplementary information** The online version contains supplementary material available at https://doi.org/10.1038/s42003-021-02445-y.

**Correspondence** and requests for materials should be addressed to J.P.H. or S.R.

**Peer review information** *Communications Biology* thanks the anonymous reviewers for their contribution to the peer review of this work. Primary Handling Editors: Nicholas Kurniawan and Anam Akhtar. Peer reviewer reports are available.

**Reprints and permission information** is available at http://www.nature.com/reprints

**Publisher's note** Springer Nature remains neutral with regard to jurisdictional claims in published maps and institutional affiliations.

# Appendix-II

## Force-activated catalytic pathway accelerates bacterial adhesion against flow

Mechanical cues often influence the factors affecting the transition-states of catalytic reactions and alter the activation-pathway. However, tracking the real-time dynamics of such activation-pathways is limited. Using single-molecule trapping of reaction-intermediate, we developed a method that enabled us to perform one reaction at one site and simultaneously study the real-time dynamics of the catalytic pathway. Using this, we showed single-molecule calligraphy at nanometer resolution and deciphered the mechanism of sortase A enzymatic reaction that counterintuitively accelerates bacterial-adhesion under shear-tension. Our method captured a force-induced dissociation of the enzyme-substrate bond that accelerates the forward reaction 100x, proposing for a new mechano-activated catalytic pathway. In corroboration, our molecular dynamics simulations in the presence of force identified a force-induced conformational switch in the enzyme that accelerates proton-transfer between CYS184 (acceptor) and HIS120 (donor) catalytic-dyads by reducing the inter-residue distances. Overall, this study opens up the possibility of studying the influence of factors affecting transition states in real-time and paves the way for the rational design of enzymes with enhanced efficiency.

**Biochemical Journal:** Available at http://dx.doi.org/10.1042/BCJ20180358

# Force-activated catalytic pathway accelerates bacterial-adhesion against flow

Jagadish P. Hazra[1], Nisha Arora[1+], Amin Sagar[1+], Shwetha Srinivasan[1], Abhishek Chaudhuri[2], and Sabyasachi Rakshit[1, 3*]

[1] Department of Chemical Sciences, Indian Institute of Science Education and Research Mohali, Punjab – 140306, India. [2] Department of Physical Sciences, Indian Institute of Science Education and Research Mohali, Punjab – 140306, India. [3] Centre for Protein Science Design and Engineering, Indian Institute of Science Education and Research Mohali, Punjab – 140306, India

Corresponding author : *srakshit@iisermohali.ac.in

Keywords: Intermediate trapping, Sortase, bacterial adhesion, Real-time reaction dynamics, single molecule force spectroscopy, single molecule localization.

**ABSTRACT:** Mechanical cues often influence the factors affecting the transition-states of catalytic reactions and alter the activation-pathway. However, tracking the real-time dynamics of such activation-pathways is limited. Using single-molecule trapping of reaction-intermediate, we developed a method that enabled us to perform one reaction at one site and simultaneously study the real-time dynamics of the catalytic pathway. Using this, we showed single-molecule calligraphy at nanometer resolution and deciphered the mechanism of sortase A enzymatic reaction that counterintuitively accelerates bacterial-adhesion under shear-tension. Our method captured a force-induced dissociation of the enzyme-substrate bond that accelerates the forward reaction 100x, proposing for a new mechano-activated catalytic pathway. In corroboration, our molecular dynamics simulations in the presence of force identified a force-induced conformational switch in the enzyme that accelerates proton-transfer between CYS184 (acceptor) and HIS120 (donor) catalytic-dyads by reducing the inter-residue distances. Overall, this study opens up the possibility of studying the influence of factors affecting transition states in real-time and paves the way for the rational design of enzymes with enhanced efficiency.

## INTRODUCTION

Force as a determinant of specific enzyme conformations leading to specific biochemical reactions is well established, from both theoretical perspectives and single molecule force measurements[1–5]. However, exploring the role of force in driving specific enzymatic-pathways has been challenging[6,7]. Using a combination of single molecule force-ramp measurements with Atomic Force Microscopy (AFM), and single-molecule fluorescence measurements, we developed a method of trapping the enzymatic reaction intermediate (TERI) to track the force activated reaction pathways in real-time. We implemented this method on sortase A enzymatic reaction that not only mediates the contact-adhesion of gram-positive bacteria to hosts against shear-flow[8–10] but also, counterintuitively, accelerates the rate of adhesion with increasing shear tension[11].

Sortase family of enzymes catalyze the bacterial cell-adhesion in a multistep process[10,12,13] for all gram-positive bacteria (including *Listeria monocytogenes Streptococcus pyogenes, Streptococcus pneumoniae*)[14]. It first recognizes the membrane-bound cell-adhesion molecules (e.g., staphylococcus protein A, Fibronectin binding proteins, FnBPA and FnBPB; clumping factors, ClfA and ClfB, etc.) from their conserved amino acid sequence (LPXTG) and forms a thioacyl-linked protein-sortase complex. This complex is formed by the nucleophilic attack of sulfhydryl($S^{2-}$) group of Cysteine184 (CYS184) of sortase to the peptide-carbonyl linking threonine(T) and glycine(G) in LPXTG polypeptide.

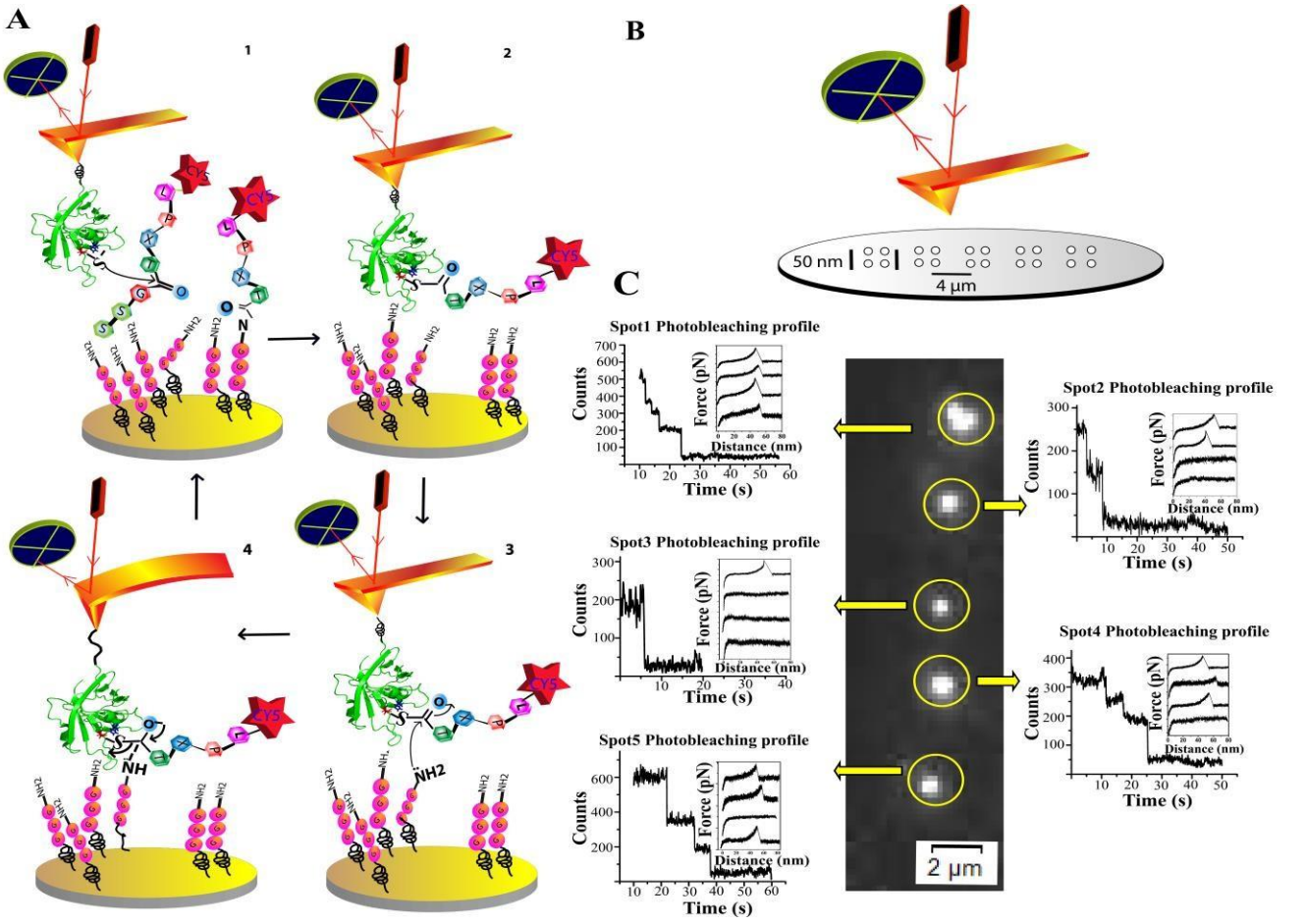


**Figure 1.** Single-Molecule Calligraphy using TERI. (A) Schematics of the TERI in steps. (1) Sortase A at the cantilever initiates the thioesterification by reacting with free cy5-LPETGSS in solution. (2) Thioester complex is formed at the cantilever. (3) Now the cantilever is brought in contact with the surface where the terminal–amine group from polyglycine initiates an attack to the thioacyl complex to form intermediate-II. 4) Upon retracting the cantilever, the formation of intermediate-II is featured as bending in the cantilever. In completion of the dissociation of the enzyme-substrate bond, a Cy5-labelled LPET remains covalently attached to the surface whereas the cantilever-sortase A complex is free to participate in another reaction. (B) Schematics of the experimental design for single-molecule calligraphy. Five major spots, 4 µm apart from each other, were constructed using force-spectroscopy. Each major spot comprised four spots within diffraction-limit, 50 nm apart from each other. (C, center) Fluorescence image of 'the single-molecule calligraphy' was obtained as designed in the scheme (B) by exciting the surface-attached Cy5-dye at 640 nm in TIRFM. The intensity-time profiles of the spots were shown sidewise guiding with arrows. Insets showed the force-spectroscopy measurements done at each major spot. Number of PEG-stretching observed corresponding to the intermediate trapping and thus, the successful completion of the reaction.

Subsequently, the nucleophilic amine from polyglycine attached to the cell-wall precursor molecules, lipid II, reacts with the thioester-acyl complex and forms a tetrahedral-intermediate (intermediate-II, Figure S1). Cleavage of the enzyme-substrate bond of the intermediate-II finally anchors the cell-adhesion molecules to the bacterial cell wall and establishes the foundation for host-pathogen interactions. This overall reaction is commonly known as sortagging. Sortagging is a continuous reaction process where the product regains the substrate binding and cleaving motif, i.e., LPXTG on it and thus, serves as a substrate for sortase (Figure S2). This reversible nature of sortagging sets the dynamics between the anchorage and obliteration of cell-adhesion molecules to/from peptidoglycans forming cell wall and subsequently, modulates the bacterial adhesion to hosts. While the sortagging

mechanism is well established, the mechanism by which the sortagging is catalyzed by shear flow, contributing towards faster cell-adhesion is poorly understood. Since the shear flow on the bacteria generates tensile force on the complexes linking bacteria to host-surfaces [15], we intend to study the reaction-kinetics of sortagging under tensile force at the single molecule resolution using TERI. We used sortase A from *Staphylococcus aureus* as a representative of sortase enzyme-family of proteins where three conserved amino-acid residues, HIS120, CYS184, and ARG197 (numbering as per sortase A), serve as triads in the catalytic activity of the entire family of the protein [16].

**RESULTS AND DISCUSSION.**

**Trapping the Enzymatic Reaction Intermediate (TERI) at the single molecule level:** We trap the sortase A–substrate intermediate-II with AFM cantilever and measure the real-time dissociation of the enzyme-substrate bond from the deflection of the cantilever (Movie S1). Each dissociation leads to covalent attachment of ligands to the glass-coverslip substrate. We employed this feature and performed the 'single-molecule calligraphy' (Figure 1A) using AFM as the proof-of-principle experiment of intermediate-trapping and subsequent dissociation. We covalently attached the C- terminal of sortase A to the AFM cantilever covalently prior to the experiment [17], and used that as a pen for the calligraphy. The sortase recognition peptide (sortag), LPETGSS, labeled with Cy5-NHS at Leucine (L) site (Cy5-LPETGSS), was used as red fluorescent ink. The glass coverslip modified with polyglycine (GGGC) was used as paper (Figure 1A). The amine ($–NH_2$) group of polyglycine was set away from the surface, available to execute the nucleophilic attack necessary for the intermediate-II formation (Figure S1). We used total internal reflection fluorescence microscopy (TIRFM) to monitor the extent of reaction from the fluorescence signal.

For the experiment, we added sortag (Cy5-LPETGSS) in the reaction buffer of pH 7.5 which readily forms the thioester-acyl complex with the sortase A attached to the cantilever (Figure 1A (1-2)). This complex is stable for hours in the buffer (Figure S3 and S4). Next, we brought the cantilever with thioester-complex down in contact to the polyglycine-coated surface and waited for 0.5 s (contact time) for the nucleophilic attack from amine (–NH2) group to happen (Figure 1A (3)). This contact facilitates the formation of intermediate-II. The contact time was optimized to 0.5s from the measure of the frequency of trapping reaction-intermediate in single molecule force spectroscopy (SMFS) for different contact times, and subsequently from the fluorescence intensity of the surface (Figure S5). Upon pulling the cantilever away in the next step, wherever the intermediate-II is formed, we observed the typical stretching of polyethylene glycol (PEG) molecules in force-spectroscopy (Figure 1A (4), Figure S6). PEG here is used as a spacer to differentiate the non-specific surface interactions [18,19]. PEG stretching manifested the trapping of the reaction intermediate-II, and the detachment of the cantilever from the surface (peak-maxima of PEG-stretch) as the dissociation of the enzyme-substrate bond, leading to the attachment of dye-labeled peptides onto the surface. Further, the stretching of PEG was confirmed from the Worm-like Chain (WLC) model fitting (Figure S6) [18,20].

We programmed to tether four molecules in 4 reaction-spots, 50 nm away from each other and repeated the pattern at five sites after unidirectionally translocating 4 μm for each step (Scheme in Figure 1B). This experimental scheme should result in five bright fluorescent spots beyond the diffraction-limit where each spot should contain four fluorophores within diffraction. We monitored the extent of TERI from the single-molecule fluorescence measurement of the grafted dyes using TIRFM as circled in Figure 1C (center panel). Direct correlations between the trapping of intermediates to the successful grafting of molecules are shown in Figure 1C (side panels). The number of PEG-stretching events (inset of Figure 1C side panels) at each spot corresponded to the successful trapping of the intermediate-II leading to tethering, and the number of steps in the intensity-time photobleaching profile of fluorophores corresponded to the number of tethered molecules (Figure 1C side panels). In spot one, all four attempts were successful as reflected from the four PEG-stretching events and four-step photobleaching profile. However, in consecutive spots only two, one, three, and three molecules were attached respectively. The position of each tethered molecule on the spot one was determined beyond diffraction-limit, using two-dimensional Gaussian fitting of the intensity-image (Figure S7) [21,22]. This experiment overall validates the concept and the successful execution of TERI which would now be used as a potential tool to measure the kinetics of sortase A enzymatic reaction and the influence of tensile force on its reaction pathway.

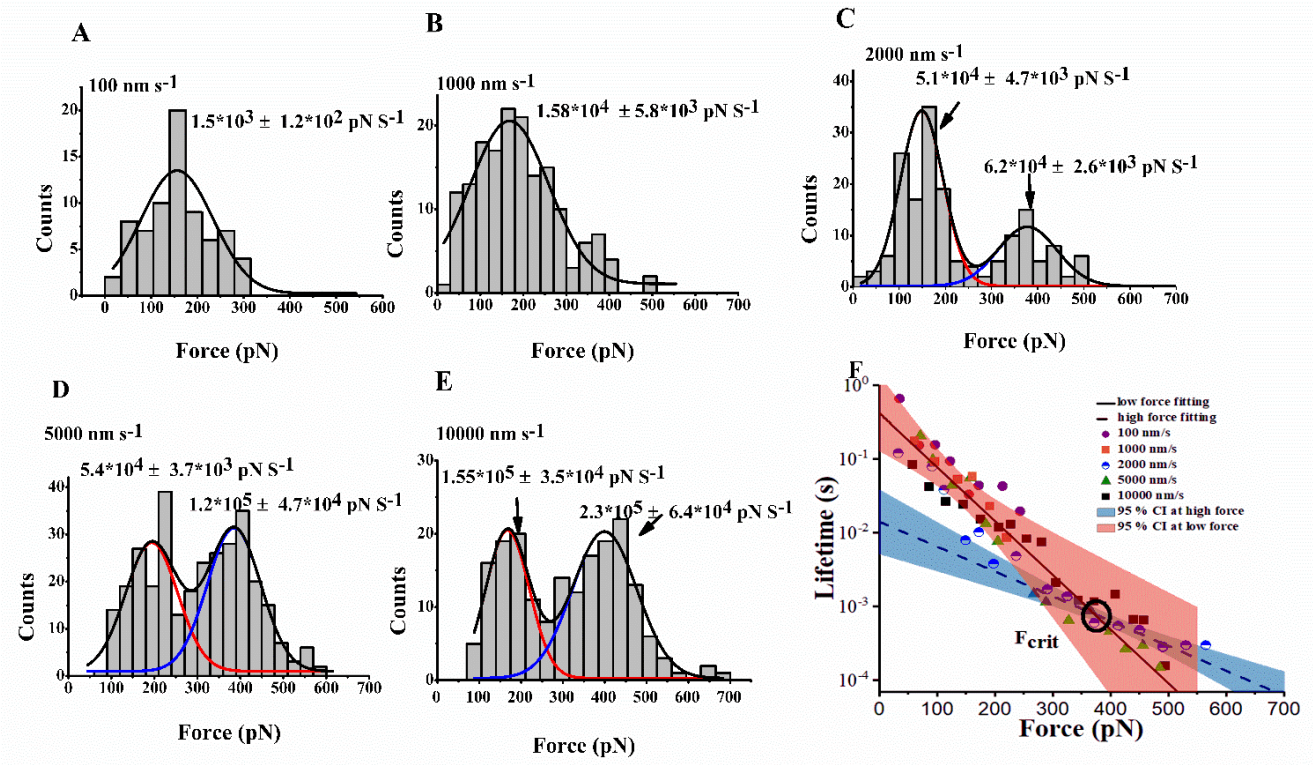


**Figure 2. Role of mechanical-tension in the dissociation of the tetrahedral intermediate-II in sortagging.** (A)Force-histograms of the enzyme-substrate bond cleavage was recorded at five different pulling-rates (A) 100 nm.s$^{-1}$ (B) 1000 nm.s$^{-1}$ (C) 2000 nm.s$^{-1}$ (D) 5000 nm.s$^{-1}$, and (E)10000 nm.s$^{-1}$. Distributions were individually fitted to Gaussian (Red and blue line) and cumulatively (black) for the guidance to the eye. (F) Lifetime for each bin of the force-distributions shown in Figure A-E was estimated using Dudko-Hummer-Szabo (DHS) model and plotted with the mean-force (center of each bin). Lifetime profiles obtained from different pulling-rates(100 nm.s$^{-1}$ (violet-circles), 1000 nm.s$^{-1}$ (orange-rectangles), 2000 nm.s$^{-1}$ (blue circles), 5000 nm.s$^{-1}$ (green triangles), 10000 nm.s$^{-1}$ (black rectangles)) were overlaid to each other. Black lines (solid and dotted) showed the fitting of low and high force regimes respectively. Colored shaded regions denote 95% CI bands. The intersection between the fitted lines of both the regions was marked with a circle, denoting the critical force ($F_{crit}$).

**TERI to decipher the counterintuitive adhesion of *S. aureus* against tensile force:** To decipher the counterintuitive adhesion mechanism of *S. aureus* against a tensile force we performed TERI as before, except the density of molecules on both surfaces was reduced to 10%, so that separation between each molecule is 600±10 nm, ensuring capture of proper single molecule events (Materials and Methods) [17]. We observed 7.6% of PEG-stretching events on average (Figure S8), and in accord with Poisson predictions, 96.8% of the PEG-stretching featured single unbinding events fitting to WLC-model (Figure S6 and S9). While repeating the experiments in the absence of any LPETGSS peptide in the buffer, or without polyglycine on the surface, we obtained 0.4% PEG-stretching events (Figure S8). This accounts for the non-specificity of the surfaces. In addition to non-specific PEG-stretching, we also anticipated PEG-stretching events for unsuccessful reactions due to the incomplete interaction between intermediate–I and nucleophile on the surface. To avoid such false attempts of the reactions, we repeated the measurements consecutively five times on each spot and analyzed those spots which featured only once PEG-stretching at either first or second attempt out of five (Figure S10).

Figure 2 (A-E) shows the force-distributions of the dissociation of the thioester-complex of intermediate-II, at five different pulling rates (nm.s$^{-1}$) of the cantilever. At low pulling rates, 100 nm.s$^{-1}$ and 1000 nm.s$^{-1}$, we observed predominantly unimodal force-distributions. At higher loading-rates, a second distribution appeared at higher force-regime (Figure 2C-E). Dissociation-force (pN) of a single-bond, the S-C$^{+}$ bond of the intermediate-II in this case, and the survival of the bond (lifetime, s) are related to the rate

at which the bond is loaded to pulling force, defined as loading-rate ($pN.s^{-1}$) [23,24]. We estimated loading-rate from the most probable unbinding forces, obtained from the peak maxima of each distribution [25]. In case of higher loading-rate we have two peak maxima and thus two loading-rates at each velocity (Fig 2A-E). Using the analytical expression relating lifetime, force, and loading-rate, as given by Dudko-Hummer-Szabo (DHS) [25], we converted the mean-force of each bin in the histogram in figure2(A-E) to survival-time of the bond at that force and depicted in Figure 2F. The limitation in DHS model is that it is applicable only to unimodal force distribution. We segregated the bimodal distribution to individual contributions using Gaussian fit as shown in Figure 2(C-E) and implemented DHS. Force-lifetime data obtained from different loading-rates showed excellent overlap amongst each other. This collapse of the data from widely distributed loading-rates is one of the major criteria to check the validity of the model. We observed a non-linear behavior in the force-lifetime plot as shown in Figure 2F. The non-linearity in the model is expected with increasing loading-rate and accounted for the spatial shift in the peak of the potential-barrier towards the bound state. In other words, the model considers the decrease in the distance between the bound state to transition-state ($x_\beta$), thus stiffening of the loaded bond with increasing loading-rate, along with the tilting of the barrier towards the load. However, the DHS model doesn't predict the appearance of a new force distribution at higher loading-rate. The new force distribution can be justified if the contribution is from a new conformation in the intermediate-II complex. This is a force-induced transient conformation.

A similar observation was reported previously in case of von Willebrand factor (VWF) binding to platelets during Haemostasis under the influence of hydrodynamic drag [26,27]. A switch from one bound state to another bound state of VWF-platelet complex was observed with loading-rates in SMFS. At lower loading-rate, only one bound state existed, and dissociation from that bound state was featured in a unimodal force-distribution. Above a critical loading-rate, the second pathway of bond-dissociation appeared and became increasingly dominating with loading-rates. The differences in the potential-barrier crossing of the bound-state were reflected as bimodal distributions in the unbinding-force histogram at higher loading-rates. We also observed similar bimodal force-distributions appearing at higher loading-rates, confirming the force-induced conformational switch, and the same has been reflected as two slopes in the force-lifetime plot. The plot can be divided into two Bell's regimes and can be fit to Bell equation (dissociation-rate, $k_{off} = k^0_{off} . \exp(\frac{F.x_\beta}{K_BT})$). At lower force regime (<300pN), the dissociation occurred from state I with an off-rate and $x_\beta$ of 1.78 $s^{-1}$ and 0.6 Å respectively. The dissociation from the switched conformation is represented by the slope in high force-regime, with off-rate and $x_\beta$ of 100 $s^{-1}$ and 0.2 Å respectively.

The faster off-rate and smaller $x_\beta$ of the intermediate-II obtained at higher force-regime indicate that the force-induced conformational-switch (state-II) accelerates the dissociation kinetics. At lower loading-rates, where the intermediate-II dissociates at forces below $F_{crit}$, it does not experience the force-induced conformational-switch and thus, follows a slower dissociation-kinetics from state I. However, with increasing loading rates, the bonds are loaded to a force above the $F_{crit}$, faster than the survival-time of the intermediate-II at state I and thus, the switch occurs. We estimated the $F_{crit}$ as 370 pN from the intersection of the decays (Figure 2F). This switch to state II possibly contributes in the flow-induced faster adhesion.

**Steered Molecular Dynamics (SMD) simulations depict the conformational-switch by mechanical tension:** For the structural elucidation of the phenomenon observed in the AFM experiments, we performed multiple constant velocity SMD simulations. To maintain the pulling geometry similar to AFM, we kept the S-group of CYS184 anchored, and pulled from the C-terminal of sortase A at a velocity of 2.5 Å/ns (and 7.5 Å/ns) and calculated distances between the residues contribute in catalysis i.e. CYS184, HIS120 and ARG197 (materials and methods). We noticed a flip of HIS120 residue towards CYS184 above a critical force that gradually decreases the distance between the $S^-$ of CYS184 and the ND1 atom of HIS120 to 5.0 Å from 8.2 Å (from crystal structure) (Figure 3A,3B, left of the vertical blue line, Movie S2). The same was reflected from the bimodal distributions of HIS120-CYS184 distances obtained from SMD (Figure 3C). The peak at 8.0 Å corresponded to the unaffected crystal structure dominated at low force regime, whereas the peak at 4.9 Å corresponded the switched conformation observed at high force regime. No change was measured in the distance between CYS184 and the third member in the catalytic-triad, ARG197 (Figure S11). This conformation-switch favors the proton

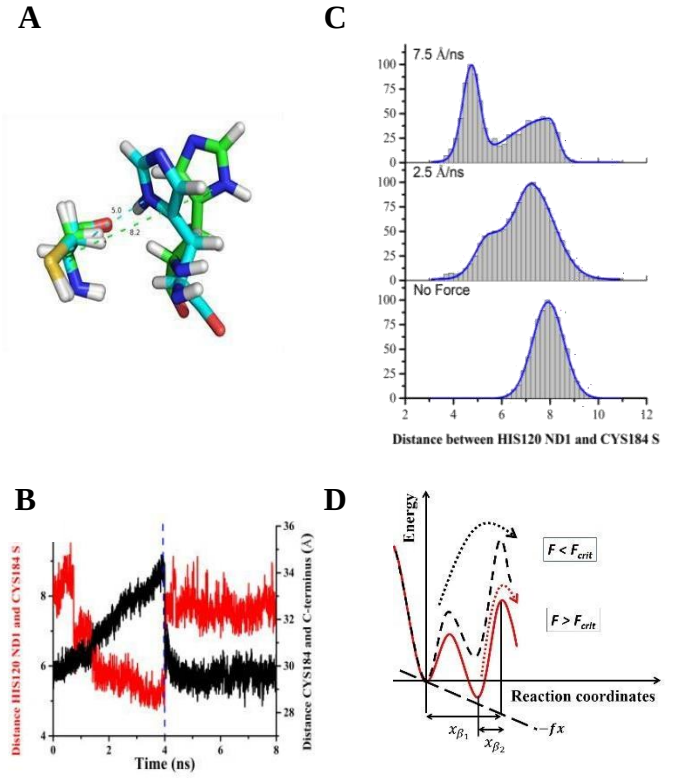


**Figure 3. Effect of force on the conformation of sortase A.** (A) An overlay of the zoomed structures of sortase A highlighting the distance between catalytic dyads, HIS120 and CYS184, at the beginning of the SMD (HIS120 and CYS184 far apart) and at the end of SMD (HIS120 and CYS184 in closer conformation). (B) The distances between HIS120 and CYS184 and between CYS184 and C-ter of sortase A were plotted in red and black lines respectively with simulation time. The force was applied by pulling the C-ter away from CYS184 for the first 4 ns (indicated by the vertical blue dashed line) after which the force was switched off and the simulation was continued for additional 4 ns. Blue dotted line marks the time where force was released. (C) Plots showing the distance-distributions between HIS120 and CYS184 at pulling velocities of 2.5 and 7.5 Å/ns and in absence of any pulling forces. (D) Schematic representation of the dissociation-pathways through an intermediate. The black dotted arrow directs the dissociation from the primary bound state where the applied force is lower than the Fcrit. Red solid line represents the energy landscape after conformational switch above Fcrit where the force-induced conformation is lower in energy than the initial conformation, and the dissociation happens through the path indicated using red arrow from the force-induced conformation state.

transfer from ND1 atom of HIS120 to the thiolate of CYS184 that eventually makes the substrate-enzyme dissociation faster. This flip is highly resilient, and upon switching off the force, HIS120 reverted to original position as shown in the crystal structure (Figure 3B, right of the vertical blue line). Reassuringly, thermal fluctuations alone could not induce the flip as observed from multiple MD simulations of 10 ns each (Figure 3B, Figure S12). Based on the experimental fit and the SMD, we proposed a dissociation-pathway model via an intermediate as a function of mechanical tension (Figure 3D)[28,29]. At a force regime lower than $F_{crit}$, the rate-limiting step is the escape from the thermodynamically stable conformation as in crystal structure (primary bound state) to the dissociated state (Black dotted line in Figure 3D). In the presence of force, the barrier heights decrease and at a force higher than $F_{crit}$, the state corresponding to the conformational switch becomes the deepest bound state (red line in Figure 3D). The escape from this state to the dissociation state is the rate determining now (red dots in Figure 3D) which is featured as the second peak in the force-distribution.

Our results present how sortase A switches its conformation to adapt to a tensile force and accelerate the sortagging of cell-adhesion molecules to the cell wall. Acceleration in the kinetics overall helps the limited number of enzymes at the host-pathogen contact to anchor number of cell-adhesion molecules to cell wall within the given contact-time and thus, strengthen adhesion (Figure S13). Existing theory to force-induced strong adhesion is catch-bonding between cell-adhesion molecules as observed for multicellular organisms [30] and gram-negative bacteria [31]. Catch-bonds extend bond-lifetime with increasing force [32]. We cannot overrule the possibility of an additional catch-bonding mechanism between cell-adhesion molecules from bacterial cell wall to host to explain the counterintuitive cell-adhesion against force [33]. However, single-molecule force spectroscopy with FnBPs that dimerize for intercellular adhesion in *S. aureus* has shown slip-bonds [34]. Slip-bonds reduce the bond-lifetime with increasing force [32].

The molecular details presented here have raised an important question, i.e. if the reaction-rate is higher with HIS120 and CYS184 closer to each other then why did the enzyme not evolve with the force-induced twisted conformation in the natural state. One possible explanation comes from the NMR structure of sortase A bound to LPAT* substrate[35], and the MD simulations performed earlier. It appears that the

force-induced conformation observed in our SMD simulations would promote the "THR-out" conformation of the peptide, i.e. THR pointing away from the active site by forming H-bond with HIS120[36]. This conformation is catalytically non-productive as it hinders the formation of thioester from the cleavage of the THR-GLY peptide bond and consecutively, the nucleophilic attack from a polyglycine-amine. Therefore, our force-induced conformation, if existed intrinsically, the covalent attachment of the peptide to CYS184, would have slowed down the reaction drastically.

The "Conformational-switching" makes sortase A a viable target for allosteric drugs[37]. The discovery of molecules that can mimic the effect of force and make Sortase A adopt the conformation seen on applying force would push the peptide into the "THR-out" non-productive conformation, effectively inhibiting the sortase catalyzed reaction. Also, if the orthosteric inhibitors are biased towards one of the available conformers of sortase, either with HIS120 and CYS184 close together or far apart, then allosterically acting compounds that enrich the needed conformation can be used along with the orthosteric inhibitors to enhance their efficacy.

## Methods

### Cloning, expression, and purification of wild-type and LPETG tagged sortase A

Sortase A (Δ59) in pET28a plasmid (Addgene plasmid # 51138) with N-terminal 6x-His tag was used as wildtype (WT). For LPETG-tagged sortase A, the peptide was genetically incorporated at the C-terminus of WT construct using PCR and cloned into NdeI and BamHI sites of the pET28a vector. Both proteins were expressed in *E.coli* BL21 (DE3) (Stratagene) cultured in LB (Luria-Bertani) media and induced at the OD600 of 0.6 with 500 μM IPTG at 16˚C for 16hr. These pellets were freeze-thawed thrice and suspended in resuspension buffer (50mM HEPES buffer with 100mM NaCl, 50mM KCl, 2mM $CaCl_2$). The cells were lysed by sonication followed by centrifugation to remove the cell debris. Both proteins were obtained in the soluble fractions that were immediately loaded on to a Ni-NTA (Qiagen) column, eluted in same buffer containing 200 mM imidazole (Hi-media). Finally, the proteins were purified using Size-exclusion chromatography with Superdex 75 16/30 column (Wipro-GE Healthcare) in 25 mM HEPES, 25 mM KCl, 100 mM NaCl, and 2mM $CaCl_2$ (pH 7.5) (Figure S14).

### Surface-functionalization for TIRF microscopy and AFM force spectroscopy experiments

The glass coverslips and $Si_3N_4$ cantilevers (Olympus, OMCL-TR400PSA-1) were cleaned with plasma for 1 min and piranha ($H_2SO_4$ : $H_2O_2$ in a ratio of 3:1) (Merck) for 3 h prior to any modifications. Subsequently, the surfaces were silanized using 2% APTES (Sigma-Aldrich) in Acetone and cured at 110 °C for 1 h. The amine exposed surfaces were reacted with a mixture of 10% NHS-PEG-maleimide in NHS-PEGm (LaysanBio) in a basic buffer (100mM $NaHCO_3$, 600mM $K_2SO_4$, pH 8.0) for 4 hours. The PEG-modified surfaces were then incubated in 100 μM polyglycine (GGGC) for 7 h at 25 ºC to anchor the peptide to surfaces via cysteine-maleimide reaction. This polyglycine serves as a nucleophile for sortagging chemistry. To covalently attach the LPETG-tagged sortase A enzyme onto the surfaces, the surfaces were incubated in a mixture of sortase A (WT) and LPETG tagged sortase A in 4:5 volume ratio at 200 nM concentration of each.

### Single-molecule fluorescence using TIRFM

LPETG-tagged sortase A was conjugated with Cy7 NHS ester nonspecifically to locate the reaction-sites on the surface. To track the thioacyl complex formation, the LPETGSS peptide; leucine (L) labeled with Cy5-NHS, was added to the surface at a concentration of 10 nM and monitored the extent of the reaction by exciting the molecules with 640 nm laser, 200 ms exposure. Next, we washed off the unreacted LPETGSS peptide from the solution and added the GGGC peptide labeled with Cy3 maleimide at cysteine (C), onto the surface. The formation of the intermediate-II was imaged by exciting the surface attached dyes simultaneously using 532 nm and 640 nm lasers at 10% intensity and in total internal reflection mode. All the image processing, image subtraction, centroid fitting, and overlapping of images from different channels were performed using home-written MATLAB programs.

An objective-based TIRFM (Olympus) equipped with 3-lasers (488-nm, 532-nm, and 640-nm diode laser system, 100 mW power) excitations and EMCCD camera (Q-Imaging Roller Thunder) with QUADVIEW options was used for fluorescence experiments. The filters used are for Quad-band LF405/488/532/635-A-000 Bright Line Full Multi-Band Laser Filter set.

### Single-molecule force ramp-spectroscopy using Atomic Force Microscopy (AFM)

Force-ramp measurements were performed at 5625 spots with a 400 nm gap between two consecutive points, thus covering 30 µm x 30 µm area. We performed such measurements at five different pulling velocities (100, 1000, 2000, 5000, and 10000 $nm.s^{-1}$) and a constant contact time of 0.5 s. The contact time is the time cantilever waits in contact to surface or ligands. To standardize the contact time, we first performed experiments at contact time varying from 0.05 s to 1 s and observed maximum events at 0.5 s.

The spring constant of the chemically modified cantilever was measured using thermal fluctuation method before each experiment. Each approach and retract distance was set to be 200 nm with data acquisition at 6 kHz.

**MD simulation methods**

The coordinates for Sortase A were obtained from Protein Data Bank entry 1T2P. The hydrogen atoms were added using AutoPSF plugin from VMD[38]. The protein was placed in a TIP3P[39] water box using the VMD plugin SOLVATE. This was followed by addition of ions using the plugin AUTOIONIZE to have a total concentration of 250 mM after neutralization of the system. All the Molecular Dynamics simulations were performed using the program NAMD version 2.12 [40][41] and CHARMM36 force field[42]. The system was first minimized for 5000 steps using conjugate gradient algorithm with the backbone atoms of the proteins constrained followed by 5000 steps of minimization with all the atoms free to move. This was followed by slowly heating up the system in steps of 20 K every 2 picoseconds (ps) with the backbone atoms constrained using harmonic restraints. The system was then equilibrated in NPT ensemble for 5 ns. The effect of force on the conformation of Sortase was studied using steered molecular dynamics (SMD) simulations. The C-terminus was restrained with a spring to a point moving with a constant velocity of 2.5 Å/ns away from the catalytic residue i.e. CYS184. The value of spring constant was chosen to be 97.3 pN/Å. All the simulations were performed using periodic boundary conditions, with the temperature kept constant at 300 K using Langevin temperature control [43] and pressure maintained at 1 atm with Nose-Hoover piston[44]. The long-range electrostatic interactions were calculated using the Particle Mesh Ewald (PME) method. A time step of 1 femtosecond (fs) was used for annealing, and it was increased to 2 fs with the bonds to the hydrogen atoms constrained used SHAKE algorithm[45] for the equilibration and SMD phase. The simulations trajectories were visualized using VMD and the distances were calculated using the program Carma [46].

ASSOCIATED CONTENT

The details of the methods used for expression and purification of sortase A, TIRF microscopy, force spectroscopy and MD simulations. The movies are showing the procedure following for single molecule intermediate trapping, and the change in the distance between CYS184 and HIS120 during the course of one SMD simulation.

AUTHOR INFORMATION

S.R. has supervised the project. J.P.H., and N.A. did the expression and purification. J.P.H., N.A., S.S. and S.R. recorded and analyzed AFM. J.P.H. and S.R. recorded and analyzed TIRF. A.S. and S.R. performed and analyzed MD and SMD. J.P.H., A.C., and S.R. performed the data-fitting and proposed model. J.P.H., N.A. and A.S. made the figures. S.R., A.S. and A.C. wrote the manuscript. J.P.H., A.S., N.A., A.C., and S.R. edited the manuscript.

N.A. and A.S. are co-second authors.

The Authors declare no competing financial interests.

Correspondence and requests for materials should be addressed to S.R. (srakshit@iisermohali.ac.in).

ACKNOWLEDGMENT

We thank Professor N. Sathyamurthy, Indian Institute of Science Education and Research Mohali, India for editing this manuscript, Professor Sri Rama Koti Ainavarapu, Tata Institute of Fundamental Research, Mumbai and Professor S. Ramakrishnan, Indian Institute of Science, Bangalore for providing critical comments that improved the scientific content of the manuscript.

S.R. acknowledges the financial support by the Indian Institute of Science Education and Research Mohali (IISERM) and the Centre of Excellence (COE) in Frontier Areas of Science and Technology (FAST) program of the Ministry of Human Resource Development, Government of India. J.P.H sincerely thank IISERM for financial support. N.A. is grateful to Council for Scientific and Industrial Research, India (CSIR) for funding. A.S. is thankful to the

Centre of Excellence (COE) in Frontier Areas of Science and Technology (FAST) program of the Ministry of Human Resource Development, Government of India for financial support. A.C. acknowledges the financial support by the Indian Institute of Science Education and Research Mohali (IISERM).
Authors also thank Satavisa Jana (MS project student, IISERM) for helping N.A. in the cloning.

## REFERENCES

1 Puchner, E. M. and Gaub, H. E. (2012) Single-Molecule Mechanoenzymatics. Annu. Rev. Biophys. **41**, 497–518.

2 Alegre-Cebollada, J., Perez-Jimenez, R., Kosuri, P. and Fernandez, J. M. (2010) Single-molecule force spectroscopy approach to enzyme catalysis. J. Biol. Chem. **285**, 18961–18966.

3 Benkovic, S. J. (2003) A Perspective on Enzyme Catalysis. Science **301**, 1196–1202.

4 Billeter, S. R., Webb, S. P., Agarwal, P. K., Iordanov, T. and Hammes-Schiffer, S. (2001) Hydride transfer in liver alcohol dehydrogenase: Quantum dynamics, kinetic isotope effects, and role of enzyme motion. J. Am. Chem. Soc. **123**, 11262–11272.

5 Piermattei, A., Karthikeyan, S. and Sijbesma, R. P. (2009) Activating catalysts with mechanical force. Nat. Chem. **1**, 133–137.

6 Pal, N., Wu, M. and Lu, H. P. (2016) Probing conformational dynamics of an enzymatic active site by an in situ single fluorogenic probe under piconewton force manipulation. Proc. Natl. Acad. Sci. **113**, 15006–15011.

7 Pelz, B., Žoldák, G., Zeller, F., Zacharias, M. and Rief, M. (2016) Subnanometre enzyme mechanics probed by single-molecule force spectroscopy. Nat. Commun. **7**.

8 Liesenborghs, L., Peetermans, M., Claes, J., Veloso, T. R., Vandenbriele, C., Criel, M., Lox, M., Peetermans, W. E., Heilbronner, S., De Groot, P. G., et al. (2016) Shear-resistant binding to von Willebrand factor allows staphylococcus lugdunensis to adhere to the cardiac valves and initiate endocarditis. J. Infect. Dis. **213**, 1148–1156.

9 Beachey, E. H. (1981) Bacterial Adherence: Adhesin-Receptor Interactions Mediating the Attachment of Bacteria to Mucosal Surfaces. J. Infect. Dis. **143**, 325–345.

10 Mazmanian, S. K., Liu, G. and Schneewind, O. (1999) Staphylococcus aureus Sortase, an Enzyme that Anchors Surface Proteins to the Cell Wall. Science **285**, 760–763.

11 Li, Z. J., Mohamed, N. and Ross, J. M. (2000) Shear Stress Affects the Kinetics of Staphylococcus aureus Adhesion to Collagen. Biotechnol. Prog. **16**, 1086–1090.

12 Navarre, W. W. and Schneewind, O. (1994) Proteolytic cleavage and cell wall anchoring at the LPXTG motif of surface proteins in Gram-positive bacteria. Mol. Microbiol. **14**, 115–121.

13 Hung Ton-That, Sarkis K. Mazmanian, K. F. F. and O. S. (2000) Anchoring of Surface Proteins to the Cell Wall of Staphylococcus aureus. J. Biol. Chem **275**, 9876–9881.

14 Mazmanian, S. K., Ton-That, H. and Schneewind, O. (2001) Sortase-catalysed anchoring of surface proteins to the cell wall of Staphylococcus aureus. Mol. Microbiol. **40**, 1049–1057.

15 McEver, R. P. and Zhu, C. (2010) Rolling cell adhesion. Annu Rev Cell Dev Biol **26**, 363–396.

16 Zong, Y., Bice, T. W., Ton-That, H., Schneewind, O. and Narayana, S. V. L. (2004) Crystal structures of Staphylococcus aureus Sortase A and its substrate complex. J. Biol. Chem. **279**, 31383–31389.

17 Srinivasan, S., Hazra, J. P., Singaraju, G. S., Deb, D. and Rakshit, S. (2017) ESCORTing proteins directly from whole cell-lysate for single-molecule studies. Anal. Biochem., Elsevier Inc **535**, 35–42.

18 Oesterhelt, F., Rief, M. and Gaub, H. E. (1999) Single molecule force spectroscopy by AFM indicates helical structure of poly ( ethylene-glycol ) in water. New J. Phys. **1**, 1–11.

19 Hinterdorfer, P., Kienberger, F., Raab, A., Gruber, H. J., Baumgartner, W., Kada, G., Riener, C., Wielert-Badt, S., Borken, C. and Schindler, H. (2000) Poly(Ethylene Glycol): An Ideal Spacer for Molecular Recognition Force Microscopy/Spectroscopy. Single Mol. **1**, 99–103.

20 Portillo, A. M., Krasnoslobodtsev, A. V and Lyubchenko, Y. L. (2012) Effect of electrostatics on aggregation of prion protein Sup35 peptide. J. Phys. Condens. Matter **24**, 164205.

21 Thompson, R. E., Larson, D. R. and Webb, W. W. (2002) Precise Nanometer Localization Analysis for Individual Fluorescent Probes. Biophys. J. **82**, 2775–2783.

22 Kufer, S. K., Strackharn, M., Stahl, S. W., Gumpp, H., Puchner, E. M. and Gaub, H. E. (2009) Optically monitoring the mechanical assembly of single molecules. Nat. Nanotechnol. **4**, 45–49.

23 Bell, G. I. (1978) Models for the specific adhesion of cells to cells. Science **200**, 618–627.

24 Evans, E. and Ritchie, K. (1997) Dynamic strength of molecular adhesion bonds. Biophys. J. **72**, 1541–1555.

25 Dudko, O. K., Hummer, G. and Szabo, A. (2008) Theory, analysis, and interpretation of single-molecule force spectroscopy experiments. Proc. Natl. Acad. Sci. U. S. A. **105**, 15755–15760.

26 Kim, J., Zhang, C. Z., Zhang, X. and Springer, T. A. (2010) A mechanically stabilized receptor-ligand flex-bond important in the vasculature. Nature **466**, 992–995.

27 Kim, J., Hudson, N. E. and Springer, T. A. (2015) Force-induced on-rate switching and modulation by mutations in gain-of-function von Willebrand diseases. Proc. Natl. Acad. Sci. **112**, 4648–4653.

28 Strunz, T., Oroszlan, K., Schumakovitch, I., Güntherodt, H. J. and Hegner, M. (2000) Model energy landscapes and the force-induced dissociation of ligand-receptor bonds. Biophys. J. **79**, 1206–1212.

29 Derényi, I., Bartolo, D. and Ajdari, A. (2004) Effects of Intermediate Bound States in Dynamic Force Spectroscopy. Biophys. J. **86**, 1263–1269.

30 Marshall, B. T., Long, M., Piper, J. W., Yago, T., McEver, R. P. and Zhu, C. (2003) Direct observation of catch bonds involving cell-adhesion molecules. Nature **423**, 190–193.

31 Aprikian, P., Tchesnokova, V., Kidd, B., Yakovenko, O., Yarov-Yarovoy, V., Trinchina, E., Vogel, V., Thomas, W. and Sokurenko, E. (2007) Interdomain interaction in the FimH adhesin of Escherichia coli regulates the affinity to mannose. J. Biol. Chem. **282**, 23437–23446.

32 Dembo, M., Torney, D. C., Saxman, K. and Hammer, D. (1988) The Reaction-Limited Kinetics of Membrane-to-Surface Adhesion and Detachment. Proc. R. Soc. Lond. Ser. B, Biol. Sci. **234**, 55–83

33 Vitry, P., Valotteau, C., Feuillie, C., Bernard, S., Alsteens, D., Geoghegan, J. A. and Dufrêne, F. (2017) Force-Induced Strengthening of the Interaction between Staphylococcus aureus Clumping Factor B and Loricrin. mBio. **8**, 1–14.

34 Herman-Bausier, P., El-Kirat-Chatel, S., Foster, T. J., Geoghegan, J. A. and Dufrêne, Y. F. (2015) Staphylococcus aureus fibronectin-binding protein A mediates cell- cell adhesion through low-affinity homophilic bonds. mBio. **6**, 1–10.

35 Suree, N., Liew, C. K., Villareal, V. A., Thieu, W., Fadeev, E. A., Clemens, J. J., Jung, M. E. and Clubb, R. T. (2009) The structure of the Staphylococcus aureus sortase-substrate complex reveals how the universally conserved LPXTG sorting signal is recognized. J. Biol. Chem. **284**, 24465–24477.

36 Jacobitz, A. W., Wereszczynski, J., Yi, S. W., Amer, B. R., Huang, G. L., Nguyen, A. V, Sawaya, M. R., Jung, M. E., McCammon, J. A. and Clubb, R. T. (2014) Structural and computational studies of the Staphylococcus aureus sortase B-substrate complex reveal a substrate-stabilized oxyanion hole. J Biol Chem **289**, 8891–8902.

37 Nussinov, R. and Tsai, C.-J. (2013) Allostery in Disease and in Drug Discovery. Cell **153**, 293–305.

38 Humphrey, W., Dalke, A. and Schulten, K. (1996) Visual molecular dynamics. J. Mol. Graph. **14**, 33–38.

39 Jorgensen, W. L., Chandrasekhar, J., Madura, J. D., Impey, R. W. and Klein, M. L. (1983) Comparison of simple potential functions for simulating liquid water. J. Chem. Phys. **79**, 926–935.

40 Nelson, M. T., Humphrey, W., Gursoy, a., Dalke, a., Kale, L. V., Skeel, R. D. and Schulten, K. (1996) NAMD: a Parallel, Object-Oriented Molecular Dynamics Program. Int. J. High Perform. Comput. Appl. **10**, 251–268.

41 Phillips, J. C., Braun, R., Wang, W., Gumbart, J., Tajkhorshid, E., Villa, E., Chipot, C., Skeel, R. D., Kalé, L. and Schulten, K. (2005) Scalable molecular dynamics with NAMD. J. Comput. Chem. **26**, 1781–1802.

42 Best, R. B., Zhu, X., Shim, J., Lopes, P. E. M., Mittal, J., Feig, M. and MacKerell, A. D. (2012) Optimization of the additive CHARMM all-atom protein force field targeting improved sampling of the backbone φ, ψ and side-chain χ 1 and χ 2 Dihedral Angles. J. Chem. Theory Comput. **8**, 3257–3273.

43 Martyna, G. J., Tobias, D. J. and Klein, M. L. (1994) Constant pressure molecular dynamics algorithm. J. Chem. Phys. **101**, 4177–4189.

44 Feller, S. E., Zhang, Y., Pastor, R. W. and Brooks, B. R. (1995) Constant pressure molecular dynamics simulation: The Langevin piston method. J. Chem. Phys. **103**, 4613–4621.

45 Ryckaert, J. P., Ciccotti, G. and Berendsen, H. J. C. (1977) Numerical integration of the cartesian equations of motion of a system with constraints: molecular dynamics of n-alkanes. J. Comput. Phys. **23**, 327–341.

46 GLYKOS, N. M. (2006) Carma: A Molecular Dynamics Analysis Program. J. Comput. Chem. **27**, 1765–1768.